PONTIFICIA UNIVERSIDAD CATOLICA DE CHILE

SCHOOL OF ENGINEERING

MULTIFACTORIAL STUDY OF EROSION-CORROSION MECHANISMS IN THE WEAR OF A LOW CARBON STEEL BY SLURRY OF COPPER TAILING

JAVIERA AGUIRRE SEPÚLVEDA

Thesis submitted to the Office of Graduate Studies in partial fulfillment of the requirements for the Degree of Doctor in Engineering Sciences

Advisor:

MAGDALENA WALCZAK

Santiago de Chile, March 2019

PONTIFICIA UNIVERSIDAD CATOLICA DE CHILE
SCHOOL OF ENGINEERING

MULTIFACTORIAL STUDY OF EROSION-CORROSION MECHANISMS IN THE WEAR OF A LOW CARBON STEEL BY SLURRY OF COPPER TAILING

JAVIERA AGUIRRE SEPÚLVEDA

Members of the Committee:

MAGDALENA WALCZAK

MAMIÉ SANCY

ALVARO VIDELA

MARGARET STACK

ANNA IGUAL

JORGE VASQUEZ

Thesis submitted to the Office of Research and Graduate Studies in partial fulfillment of the requirements for the Degree of Doctor in Engineering Sciences

Santiago de Chile, March, 2019.

ACKNOWLEDGEMENTS

I would like to express my deep gratitude to my advisor, professor Magdalena Walczak, for guiding me during this process, sharing with me her passion for research and academic life. This thesis is not only my effort but also his. I would also like to thank Dr. Michael Rohwerder, my advisor during my stay as a visiting researcher at the Department Interface Chemistry and Surface Engineering of the Max-Planck-Institut für Eisenforschung, for giving me the exceptional opportunity of performing research at one of the leading materials research centers.

My gratitude also goes to all people who collaborated in the development of this thesis. Members of the Mechanical and Metallurgical Engineering Department, especially people from the mechanical workshop and maintenance. Research assistants and undergraduate students from Laboratorio de Corrosión y Desgaste de Materiales. Moreover, to my colleagues from MPIE Cauê Corrêa da Silva and Dr. Waldemar Krieger for their indispensable help during my research internship.

I am grateful to the members of the Doctoral Thesis Committee, professors Álvaro Videla, Mamié Sancy, Margaret Stack and Anna Igual, for the significant feedback they provided to the development of this thesis, collectively and individually in several instances along these years.

I acknowledge the scholarship for Doctorate studies (No 21150171) awarded to me by the Comisión Nacional de Ciencia y Tecnología, CONICYT, de Chile, between August 2014 and January 2019. Besides, to the project CONICYT through FONDECYT grant No. 1141107.

I would like to thank my boyfriend, friend, and colleague Francisco, for supporting me emotionally, academically and technically during this process, for being with me in good times, but above all in the bad ones.

Finally, I would like to express my profound gratitude to my family especially to my mom Marta for her unconditional support throughout these years.

TABLE OF CONTENTS

LIST OF TABLES

LIST OF FIGURES

PONTIFICIA UNIVERSIDAD CATOLICA DE CHILE
ESCUELA DE INGENIERIA

MULTIFACTORIAL STUDY OF EROSION-CORROSION MECHANISMS IN THE WEAR OF A LOW CARBON STEEL BY SLURRY OF COPPER TAILING

Thesis submitted to the Office of Research and Graduate Studies in partial fulfillment of the requirements for the Degree of Doctor in Engineering Sciences by

JAVIERA AGUIRRE SEPÚLVEDA

ABSTRACT

The hydraulic transport of solids (hydro-transport) in the form of slurry is an essential technology for transporting large volumes of raw, process and waste materials in several industries such as oil and gas, metallurgy and mining. However, although this type of transport system is considered safe compared to other alternatives, corrosion and erosion have constituted an essential threat to the integrity of the slurry transport system. Erosion-corrosion (E-C) of metallic materials describe the material degradation process where mechanical wear by solid particles interact with the electrochemical corrosion process. A major issue in approaching the understanding of E-C material loss processes is the large number of variables involved since multiple factors can act simultaneously or interact between them, affecting considerably the type of material removal mechanisms involves in the wear process. Thereby, a comprehensive understanding of the erosion-corrosion mechanisms is of practical importance to establish the mitigation strategy.

This research focuses on quantifying and characterizing the effects of selected factors and their interactions on the E-C wear in conventional pipe steel, API 5L X65, by a synthetic copper tailing slurry. The studied parameters are velocity, particle

concentration, temperature, pH, dissolved oxygen and copper ions. The study by experimental design was conducted using a rotating cylinder electrode to induce the E-C damage. The contribution and statistical significance of each studied parameter in the wear process were determined using statistical tools while the wear mechanism affected by the main factors and interactions was analyzed using surface characterization techniques and electrochemical analysis.

The statistical analysis revealed that three main effects and two interactions explain the increment in wear rate. These are slurry velocity, dissolved oxygen, and temperature, and interactions between velocity/dissolved oxygen and particle/copper ions content. In addition, it is concluded that increment in particle energy and frequency of impact are the main contributors in removing the material at higher particle velocity. Whereas, the availability of dissolved oxygen prevents the formation of a work-hardened layer in the sub-surface of the steel and promotes localized-type corrosion by a mechanism dominated by erosion-enhanced corrosion. The remaining main effects and interactions can be described regarding the same mechanism.

Members of the Doctoral Thesis Committee:

Magdalena Walczak
Mamié Sancy
Álvaro Videla
Margaret Stack
Anna Igual
Jorge Vásquez

Santiago, March 2019.

PONTIFICIA UNIVERSIDAD CATOLICA DE CHILE
ESCUELA DE INGENIERIA

ESTUDIO MULTIPARÁMETROS DE LOS MECANISMOS DE EROSION-CORROSION DE UN ACERO CON BAJO CONTENIDO DE CARBONO POR PULPA DE RELAVE DE COBRE

Tesis enviada a la Dirección de Investigación y Postgrado en cumplimiento parcial de los requisitos para el grado de Doctor en Ciencias de la Ingeniería.

JAVIERA AGUIRRE SEPÚLVEDA

RESUMEN

El transporte hidráulico de sólidos (hidro-transporte) en forma de pulpa es un proceso esencial para el transporte de grandes volúmenes de materias primas y residuos en diferentes industrias como la industria del gas y petróleo, metalúrgica y minera. Sin embargo, aunque este tipo de sistema de transporte se considera seguro en comparación con otras alternativas, la corrosión y la erosión han constituido una amenaza esencial para la integridad del sistema de transporte de pulpas. La erosión–corrosión (E−C) de los materiales metálicos describe el proceso de degradación del material en el que el desgaste mecánico de las partículas sólidas interactúa con el proceso de corrosión electroquímica. Un problema importante en la comprensión de los procesos de degradación debido al daño por E−C es el gran número de variables involucradas, ya que, múltiples factores pueden actuar simultáneamente o interactuar entre ellos, afectando considerablemente el tipo de mecanismos de remoción de material que implica el proceso de desgaste. Por lo tanto, una comprensión integral de los mecanismos de erosión–corrosión es importante para establecer una estrategia de mitigación apropiada.

Esta investigación se enfoca en cuantificar y caracterizar los efectos de determinados factores y sus interacciones en el desgaste E−C en un acero de tubería convencional, API 5L X65, por una pulpa de relave de cobre sintético. Los parámetros estudiados fueron: la velocidad, concentración de partículas, temperatura, pH, oxígeno disuelto y contenido de iones de cobre de la pulpa. El estudio fue realizado mediante un diseño experimental utilizando un electrodo de cilindro rotante para simular el daño por E−C. La contribución y significancia estadística de cada factor en el proceso de desgaste se determinó utilizando herramientas estadísticas, mientras que el mecanismo de desgaste influenciado por los factores principales e interacciones fue analizado mediante técnicas de caracterización de superficie y análisis electroquímico.

El análisis estadístico reveló que el incremento en la tasa de desgaste se explica por tres efectos principales y dos interacciones. Estos son: la velocidad de la pulpa, cantidad de oxígeno disuelto y la temperatura, además de las interacciones entre velocidad/oxígeno disuelto, y la concentración de partículas/contenido de iones cobre. Por otro lado, se concluye que el incremento en la energía de las partículas y la frecuencia del impacto son los principales contribuyentes en la remoción del material a alta velocidad de pulpa. Mientras que, la disponibilidad de oxígeno disuelto evita la formación de una capa endurecida en la sub-superficie del acero y promueve la corrosión de tipo localizada por un mecanismo de corrosión mejorado por erosión. Los demás efectos e interacciones principales se pueden describir en términos de los mismos mecanismos.

Miembros de la Comisión de Tesis Doctoral

Magdalena Walczak
Mamié Sancy
Álvaro Videla
Margaret Stack
Anna Igual
Jorge Vásquez

Santiago, Marzo 2019.

LIST OF PAPERS

J. Aguirre, M. Walczak. Effect of dissolved copper ions on erosion-corrosion synergy of X65 steel in simulated copper tailing slurry. *Tribology International*, Volume 114, October 2017, Pages 329-336.

J. Aguirre, M. Walczak. Multifactorial study of erosion-corrosion wear of a X65 steel by slurry of simulated copper tailing. *Tribology International*, Volume 126, October 2018, Pages 177-185

J. Aguirre, M. Walczak, M. Rohwerder. The mechanism of erosion-corrosion of API X65 steel under turbulent slurry flow: Effect of nominal flow velocity and oxygen content. Sent to *Wear*, May 2019.

1 INTRODUCTION

The hydraulic transport of solids (hydro-transport) in form of slurry is, at this time the most reliable, available and economical solution for long distance and high mass transport in a large number of industries such as oil and gas, metallurgy and, especially in mining where the ore, concentrate or tailings are usually transferred by this type of systems. Chile has important mineral deposits located in the high mountain range, most of them from 2500 meters above sea level, and most of the time in areas where the accesses are limited by many different factors like weather or lack of roads. This geographical context present intrinsic difficulties to high mining for the inspection, design, and operation of its transport systems. Therefore, ensure the correct operating conditions and integrity of the hydraulic transport of solid is a fundamental stage for the development and sustainability of the copper mining process in Chile.

During the process of copper mineral, three types of slurries are generated: ore pulp (slurry of crushed and ground mineral), copper concentrate (slurry of copper floccules after flotation process) and copper tailings (slurry of mineral waste once the copper has been extracted and processed). Among these slurries, the concentrate and tailings are the most commonly transported using low-carbon steel pipelines. Although this type of transport system is considered safe compared to other alternatives, erosion-corrosion (E−C) phenomenon has constituted an essential threat to the integrity of the slurry transport system.

The damage caused by E-C generates significant losses in productivity, owing to the costs associated with the replacement of critical components, such as pump cases, impellers, valves, and of course long distances of pipes. Then, obtaining a better understanding of E-C is necessary for improving the predictability of associated failures, planning feasible mitigation strategies, developing and implementation of inspections plans and improve the security and integrity from the early stage in the design process in hydraulic transport systems.

Erosion-corrosion of metallic materials describes the material degradation process where mechanical wear by solid particles, liquid or the combination of both interact with the electrochemical corrosion process over the material surface. Extensive experimental works had demonstrated that erosion and corrosion in flowing slurry would enhance mutually, increasing the wear rate of the material, which is commonly referred to as *positive synergism*. A major issue in the understanding of material loss by erosion-corrosion processes is the large number of variables involved such as characteristics of the target, the dispersed phase and of the flow environment. Even more, multiple factors can act simultaneously or interact between them, affecting the type of material removal mechanisms involves in the wear process considerably. However, in a multivariable system, not all factors contribute with the same intensity to the material degradation. Therefore, the extent of E−C rate in a determined system of metal-electrolyte/slurry can be attributed to some key variables which need to be determined.

In the case of the Chilean hydraulic transport systems of copper tailing slurry, the presence of water and oxygen, combined with concentrations of some heavy metals ions, causes corrosion to the carbon steel pipe. This electrochemical process is accelerated by the flowing slurry and the high content of solid sand particles. As of date, there is no systematic study of the variables or mechanisms that could affect the degradation of this type of systems. Consequently, the proposed research aims to improve the understanding of complex E-C phenomena for the particular case of steel used in pipelines in hydraulic transport systems of copper tailings in Chile.

This work focuses on quantifying and characterizing the effects of selected factors and their interactions on the E-C wear in conventional pipe steel, API 5L X65, by a synthetic copper tailing slurry. The studied parameters are chosen by significance observed in the operation of slurry pipelines which are: velocity, the concentration of particles, temperature, pH, and content of dissolved oxygen and copper ions. The study by experimental design is conducted using a rotating cylinder electrode (RCE) to induce the E-C damage. The contribution and statistical significance of each study parameter in the wear process are determined, and the significant interactions are characterized by contour

maps. On the other hand, the wear mechanism affected by the main factors and interactions is analyzed using advanced surface characterization techniques and electrochemical analysis.

2 LITERATURE REVIEW

This literature review is divided into four sections encompassing an overview and introduction to the field of slurry erosion, metallic corrosion, erosion-corrosion and the context of copper mining in Chile.

2.1 Slurry erosion

2.1.1 Fundamentals of erosion mechanisms

The wear process known as solid particle erosion is defined as the progressive loss, fracture or displacement of material under the repeated impingement of solid particles, carried by gas streaming or fluid, on a target material. In particular, if the erodent particles are carried by a liquid, the wear may be termed *slurry erosion* (Hutchings, 1992; Javaheri, Porter, & Kuokkala, 2018). Slurry erosion usually occurs under turbulent flow conditions when the moving slurry strikes a surface, scars it and removes material. According to Hutchings (1992) during erosion, several forces of different origins may act on a particle in contact with the solid surface as shown in Figure 2.1. Thus, solid particles entrained in a liquid media would be subjected to drag forces by the flowing fluid as well as gravitational and contact forces due to surrounding particles interacting with each other. However, the most dominant force is the contact force exerted by the surface.

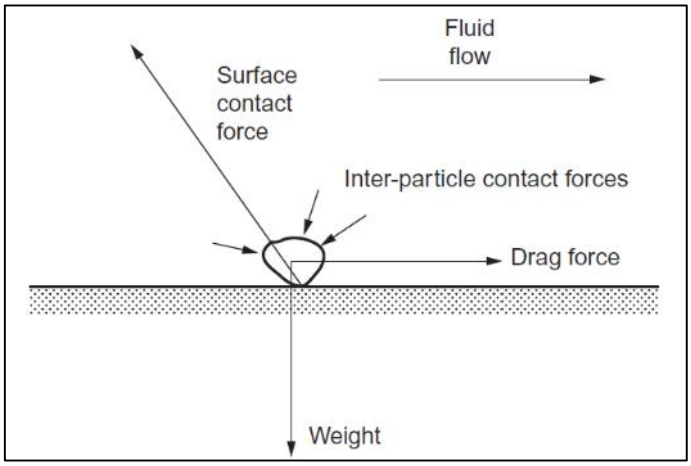

Figure 2.1 Diagram of forces acting on a particle in contact with a solid surface (Hutchings, 1992).

Surface deformation as result of solid particle erosion has been extensively studied (Bitter, 1963a, 1963b; Finnie, 1960; Hutchings, 1992) for metallic surfaces in order to understand the material remove mechanisms involved in the process. Thus, it is well accepted that there are two basics mechanism in erosion damage referred to as *cutting* and *deformation* as were originally introduced by Finnie (1960). The cutting mechanism is associated with particles impacting the eroding surface at an oblique angle with enough energy to plow or cut the surface. Whereas the deformation mechanism is associated with particles impacting perpendicular to the eroding surface, in this case, the kinetic energy is transfer from solid particles to the surface of the target material inducing the material deformation, crack initiation and propagation (Javaheri et al., 2018; Wang & Yang, 2008). These two mechanisms can occur simultaneously in ductile materials as metals whereas only progressive crack growth is the case for brittle materials as ceramics. Figure 2.2 illustrates the erosion mechanism for both types of materials.

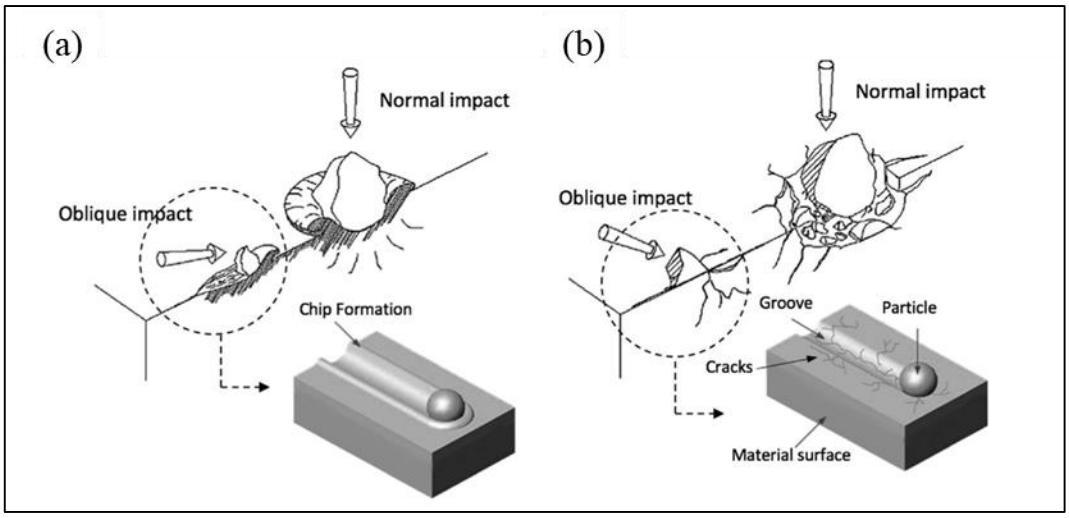

Figure 2.2 Schematic representation of erosion caused by deformation mechanism at normal impact and cutting mechanism at oblique impact in a) ductile and b) brittle materials (Javaheri et al., 2018).

In the erosion damage, the interaction between all these mechanisms is very complex since it is a time-dependent phenomenon where the erosion damage results from the cumulative effect of large numbers of particle impact a surface. Experimentally it has

been observed (Hadavi, Arani, & Papini, 2019; Söderberg, Hogmark, Engman, & Swahn, 1981; Wood, Walker, Harvey, Wang, & Rajahram, 2013) that for ductile materials the mass loss rate can be characterized as a function of time in three stages according to the representation of Figure 2.3. The first stage corresponds to the incubation period where particles and fragments can embed into an uneroded surface, resulting in a preliminary mass gain of the sample. The second stage is the accumulation period where the surface begins to be work hardening by particles impact leads to the reduction of embedded particles and the increase of material loss through the removal of extruded material from previous impacts. Finally, the steady-state period occurs when the surface material has reached equilibrium between particle embedment and surface work hardening as a result of the impact conditions.

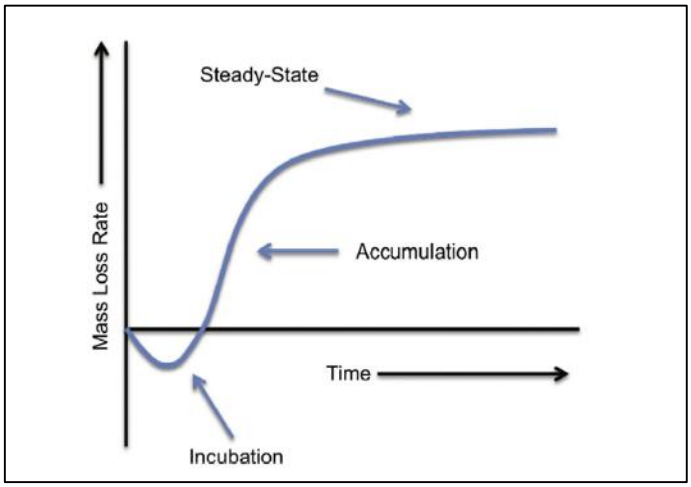

Figure 2.3 Scheme of material removal rates as a function of time for the erosion process (Wood et al., 2013).

2.1.2 Factors influencing erosion

In practice, the total erosion rate is dependent of a large number of parameters, which can be classified into three groups as material characteristics, erodent properties, and slurry characteristic and flow conditions listed in Table 2.1. This section will review some of the key factors influencing erosion.

Table 2.1 Summary of factors influencing erosion process.

Material characteristics	Erodent properties	Slurry characteristics and flow conditions
Hardness	Hardness	Slurry velocity/turbulence
Modulus of elasticity	Size	Impact angle
Toughness	Shape	Erodent concentration
Chemical composition	Density	Temperature
Microstructure		pH
		Viscosity

2.1.2.1 Slurry velocity

The effect of slurry particle velocity has been extensively studied on last decades due to its dominant effect on the material removal rate (Alam, Aminul Islam, & Farhat, 2015; Clark, 2002; Clark, 1991; Gandhi, Singh, & Seshadri, 1999; Islam & Farhat, 2014; Yang & Cheng, 2012). Several studies proposed that erosion rate (E) follow an empirical power-law relationship with particle velocity (V) according to the following equation (Kosel, 1992; Mbabazi, Sheer, & Shandu, 2004; Molinari & Ortiz, 2002; Stevenson & Hutchings, 1995):

$$E = KV^n \qquad \text{(Equation 2.1)}$$

where K is an experimental constant and n is the velocity exponent commonly reported to take values between 0.34 and 4.83 depending on the relative properties of the particles and material, as well as specific conditions of the test (Akbarzadeh, Elsaadawy, Sherik, Spelt, & Papini, 2012; Clark, 1992; Desale, Gandhi, & Jain, 2008; Javaheri et al., 2018). The increase in wear rate with velocity is associated mainly with the increase in the kinetic energy of the particles that causes greater effective damage on the surface. It is believed that there is a threshold over which the particles have enough energy to deform the material plastically, while those particles with low energy only result in elastic deformation of the target and do not contribute to measurable erosion rate (Islam & Farhat,

2014). Thus, a greater slurry velocity more particles will have the critical energy necessary to deform and remove the material.

On the other hand, regardless the impact angle of the particle, the contribution of particle velocity to the erosion mechanism has two fundamental components according to Finnie (1960) and Bitter (1963a, 1963b) description. A vertical component that is responsible for penetrating the metal matrix, and a horizontal component which is responsible for plowing the surface as the particle moves through it. Both of them give depth and shape to wear scars, respectively.

2.1.2.2 Impact angle

Impact angle (θ) in erosion is defined as the angle between the velocity vector of particles and the target surface (Hutchings, 1992), as shown the Figure 2.4. For normal impact, $\theta = 90°$, while flush to the surface θ tends to 0°. Particle impact angle is considered crucial in the extension of the wear damage since it is closely related to the nature of the erosion mechanism in a given system. Experimentally (Desale, Gandhi, & Jain, 2011; Kosa & Göksenli, 2015; Nandre & Desale, 2018; Shipway & Hutchings, 1996), it has been observed that wear rate dependence on the impact angle for ductile and brittle materials is different as shown in Figure 2.4. For ductile materials, maximum erosion occurs typically between 20° to 30° falling to one-third of the peak wear rate at normal incidence, the main erosion mechanism at this condition is plastic deformation in which material is removed by displacing or cutting action of the hard particle. In brittle materials, the maximum erosion rate occurs at normal incidence where the material is removed by formation and intersection of cracks that radiate out from the point of impact of the erodent particle (Ben-Ami, Uzi, & Levy, 2016; Hutchings, 1992; Kleis & Kulu, 2008).

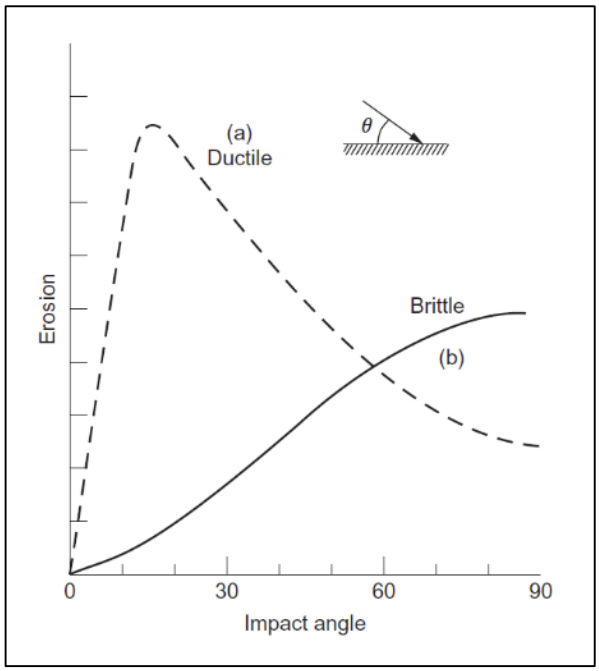

Figure 2.4 Typical dependence of erosion on impact angle θ for (a) ductile and (b) brittle metals (Hutchings, 1992).

Studies of single particles on to metals at different impact angles have shown some basic types of impact damage as shows Figure 2.5. Söderberg, Hogmark, & Swahn (1983) classified examples of different type of single-impact craters according to geometry, preferential impact angle, and mechanism as:

a. Micromachining-type craters (Figure 2.5a): commonly observed to low impact angles (15°) are generated by the removal of a chip of material by the impact of the particle.
b. Plowing-type craters (Figure 2.5b): are generated by the impact of the particles at low impact angles (15°). Particle plows the material parallel and transverse to its path without detaching the material.
c. Lip formation-type craters (Figure 2.5c): observed at middle impact angles (45°). Particle cuts or plows the material in the direction of its path without detaching the material.
d. Indentation-type craters (Figure 2.5d): the particle extrudes the material to the side. Typical for high impact angles (θ>45°).

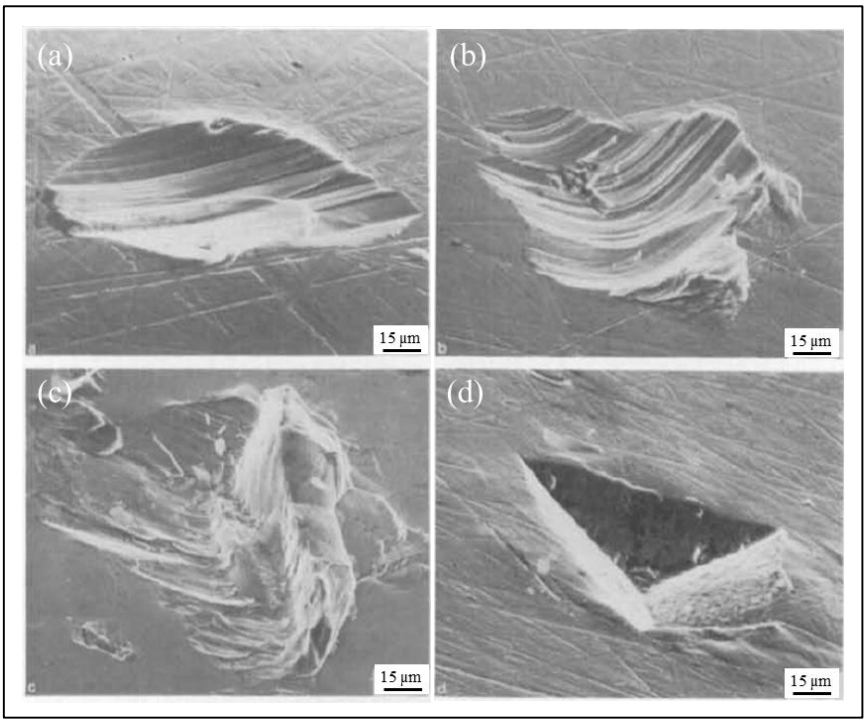

Figure 2.5 Examples of simple-impact craters at different angles of impingement. (a) Micromachining-type craters; (b) Plowing-type craters; (c) Lip formation-type craters; (d) Indentation-type craters. Adapted from Söderberg et al. (1983).

In a multiple impacts system as expected in practice, erosive wear is associated with the detachment raised craters rim and lips, after several impacts, in case of oblique angles whereas the detachment of material for indentation craters is expected by fracture of vulnerable ends after several cycles of plastic deformation (Hutchings, 1992; Shipway & Hutchings, 1996).

2.1.2.3 Erodent shape

The shape of erosive particles also is an important factor affecting the erosion mechanism. Angularity is difficult to define in a three-dimensional particle. Therefore, particles are often describing as spherical, rounded and angular. Several works (Al-Bukhaiti, Abouel-Kasem, Emara, & Ahmed, 2016; Desale, Gandhi, & Jain, 2006; Alan Levy & Chik, 1983; Stachowiak, Salasi, Rickard, & Stachowiak, 2016) have concluded that angular particles lead higher erosion rate than spherical or rounded particles. The

latter can be mainly explained by the different type of erosion mechanism dominant in each case. Hutchings (Hutchings, 1992; 1981; Winter & Hutchings, 1974) suggested two different mechanisms of material removal for rounded and angular particles. He proposed that the impact of rounded particles removes the target material by plowing and deformation displacing the material around the craters, producing more rounded and shallow craters. Whereas in angular particles the material is mainly removed by cutting action producing sharp and deep craters in the target material that form extruded lips more easily. Thus, more rounded particles lead to less localized deformation, and more impacts are required to remove each fragment of debris.

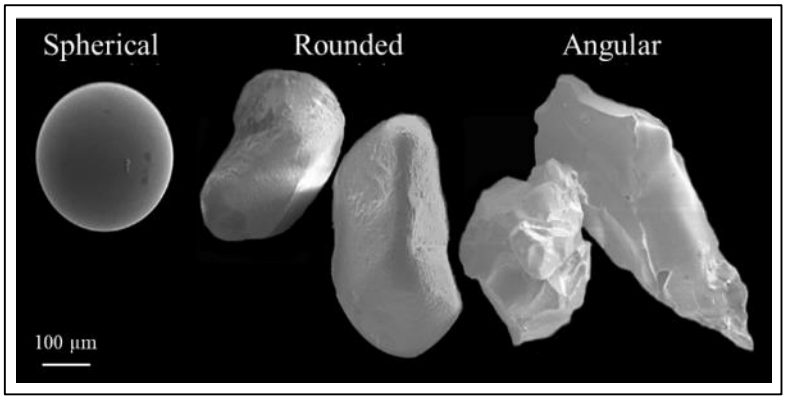

Figure 2.6 Example of spherical, rounded and angular particles. Adapted from Stachowiak et al. (2016).

2.1.2.4 Erodent size

The size of particles hitting the target surface has a significant effect on erosion rate. It is generally observed for ductile materials that the wear increases with an increase in the particle size (Desale, Gandhi, & Jain, 2009; Gupta, Singh, & Seshadri, 1995; Misra & Finnie, 1981; V. B. Nguyen, Nguyen, Zhang, Lim, & Khoo, 2016; Sinha, Dewangan, & Sharma, 2017). Clark and co-workers (Clark, 2002; 1991; Lynn, Wong, & Clark, 1991) have studied the effect of particle size on erosion rate, in terms of striking efficiency, for a wide range of particle size. According to them, small size particles have lower striking efficiency and dissipate less kinetic energy during impact as compared to the bigger size particles, and therefore small size particles cause less wear. However, it has been shown

that particles with sizes smaller than 100 μm often failed to approach the specimen surface, while the particles with larger sizes in the order of 1 mm, had a little deviation from their original trajectories or produce lower energy transmitted to the target material by previous fragmentation (Benchaita, Griffith, & Rabinowicz, 1983; Clark & Burmeister, 1992; H. McI Clark & Hartwich, 2001; Misra & Finnie, 1981). Therefore, it has been observed that exists a range of erodent size for which a maximum wear rate occurs which depends on the conditions in a determined system. Iwai & Nambu (1997) reported for 403 stainless steel in a slurry containing different silica sand size (42-415 μm) an erosion peak at 300 μm. Stack & Pungwiwat (1999) studied this phenomenon for several materials that as iron, aluminum, stainless steel, alumina, and Teflon using slurry containing alumina for size between 250-1000 μm. They reported that a peak in the erosion rate occurred at intermediate particle sizes between 500-710 μm for all but ceramic materials. Whereas, Rajahram, Harvey, & Wood (2009) observed a peak of wear damage between 150-300 μm for AISI 1020 steel and UNS S31603 stainless steel exposed to a slurry of silica particles (between 100-600 μm). According to Stack & Pungwiwat (1999), the erosion peak varied as a function of the particle velocity and shape, target material properties and characteristics of the flowing environment.

2.1.2.5 Erodent concentration

The term “erodent concentration” is very often interpreted as the percentage content by weight or by volume of the particles in a fluid medium (Kleis & Kulu, 2008). Some research (Dasgupta, Prasad, & Jha, 1998; Turenne, Fiset, & Masounave, 1989) has shown that an increase in the erodent concentration leads an increment in the erosion rate since more particles are impinging the target material. However, this is only valid for slurries with a low solids content where a linear dependence between the erosion rate and the particle concentration is observed; after a certain threshold this behavior changes and the effective erosion rate decrease (Kleis & Kulu, 2008; Turenne et al., 1989). Turenne et al. (1989) found that increasing the particle concentration the erosion efficiency decreases according to the power law of the erodent concentration in the slurry. They proposed that

at a high erodent concentration leads to greater particle-particle interaction reducing the number of particles impacting the surface due to rebounding (“blanketing") or screening effect between particles. However, other effects such as particle size reduction (attrition effect) by particle-particle interaction are also valid.

2.1.2.6 Hardness of target material and erodent

The hardness of particles involved in the erosion process influences the erosion rate since particles with a lower hardness than the surface causes less damage than hardener particles (Hutchings, 1992). In this context, the ratio between particle hardness (H_a) and target material hardness (H_s) is widely used to describe this effect. Generally, with an increase in the H_a/H_s ratio, the total erosion increases until a certain value after which a further rise in the hardness ratio has no apparent effect (Arabnejad, Shirazi, McLaury, Subramani, & Rhyne, 2015; Desale et al., 2006; Javaheri et al., 2018; Alan V. Levy & Chik, 1983). According to Hutchings (1992), particle impacting a plane surface under normal load should exceed three times the uniaxial yield stress of the surface for that the surface of the material flows plastically. If the particle fractures or deforms during the impact the kinetic energy will not be effectively transferred to the target material, then, insignificant plastic deformation will occur in the surface (Arabnejad et al., 2015). Experimentally, it is expected that a particle of any shape scratch a surface if the H_a/H_s >1.2 as illustrated in Figure 2.7 (Finnie, 1995; Hutchings, 1992).

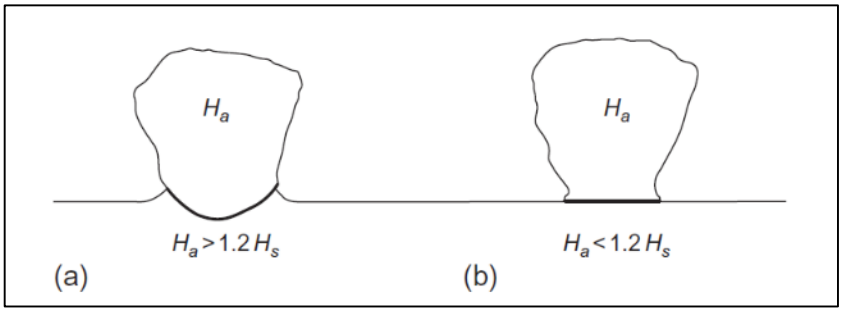

Figure 2.7 Particle impact under normal load and a plane surface. (a) If $H_a > 1.2\ H_s$, the particle will indent the surface. (b) If $H_a < 1.2\ H_s$, the plastic flow will occur in the particle (Hutchings, 1992).

On the other hand, it is generally believed that materials with higher hardness have higher erosion resistance (Finnie, 1995). However, this is not always a good approximation since the hardness of the bulk is different from the surface during the erosion process due to the work-hardening that the particles carry out on the surface (Finnie, 1995; Hutchings, 1992).

2.1.2.7 Slurry temperature

The effect of temperature can affect both the behavior of the material and the physical characteristic of the slurry. On the one hand, metals at higher temperatures tend to be less brittle than at lower temperatures. On the other hand, as temperature increase viscosity of the slurry decrease which leads to higher mobility of the solid particles. Levy & Hickey (1987) tested six different steel alloys in a slurry pot tester in the range 25-175°C. Between 25-95°C, the wear rates of all alloys either decreased or remained almost constant, then it increased rapidly up to 175°C. This behavior was associated with changes in the nature of the slurry liquid rather than changes in the alloy properties. Whereas, Young & Ruff (1977) studied the behavior of an AISI 304 stainless steel increasing the target material temperature from 25 °C to 500 °C. They observed a decrease in erosion rate due to changes in the surface chemistry which led to the growth a protective oxide on the steel surface.

2.2 Metallic corrosion

2.2.1 Fundamentals of corrosion mechanism

Damage of metallic material by corrosion can be defined as the chemical degradation of a metal due to the exposure to the environment. However, this corresponds to a complex spontaneous electrochemical process that involves an irreversible interfacial reaction of the metal and its environment, which result in a loss of material or the dissolving of one of the constituents of the environment into the material (Heusler, Landolt, & Trasatti, 1989; Landolt, 2007). From an engineering point of view, corrosion

is damaging because it can degrade some functional properties of a material, being able to generate catastrophic failures. Even though there are different forms and types of corrosion, this review will concentrate on electrochemical corrosion phenomena in wet environments specifically in *flow accelerated corrosion*.

As all electrochemical process, corrosion involves the transfer of electrons across the interface between an electronic conductor (electrode, in this case, the metal) and an ionic conductor (electrolyte) (Landolt, 2007). The global reaction is composed of two coupled partial reactions: oxidation and reduction (redox). Oxidation involves the loss of electrons from the metal whereas reduction leads the gain of electrons by an oxidizing agent (commonly protons, oxygen, metallic ions among others) present in the environment. Both reactions take place in different places, the oxidation in the anode and the reduction in the cathode; this is why they are usually called anodic and cathodic reaction, respectively. On a corroding metal surface, anodic and cathodic reactions, take places in different regions of the metal surface as is shown in Figure 2.8.

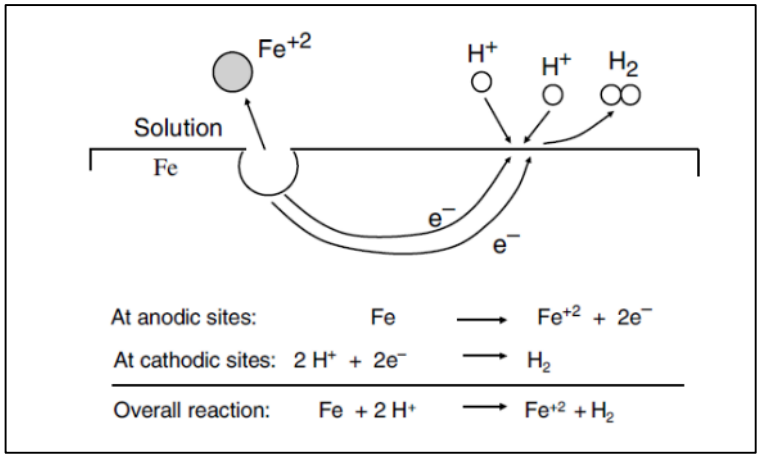

Figure 2.8 Coupled electrochemical reaction occurring at different sites on the same metal surface for iron in an acid solution (Mccafferty, 2010).

The reason that two partial reactions can occur on the same metal surface is due to the intrinsic heterogeneities present on the metal surface. Polycrystalline metals surfaces contain an array of site energies due to different phases, grain boundaries, deformations,

stresses or imperfections in the material, so some areas in the same metal are more susceptible than others to corroding (Mccafferty, 2010).

2.2.2 Electrochemical behavior of metals

From the surface chemistry point of view, metals can exhibit different behavior in aqueous electrolytes; Concentration of protons, i.e., pH, and the presence of dissolved oxygen in the electrolyte can modify the corrosion behavior of a material (Landolt, 2007; Mccafferty, 2010). Marcel Pourbaix (1974) developed a unique method to summarized the thermodynamic behavior of different metals in equilibrium with their aqueous environment in a useful potential-pH diagram. The Pourbaix Diagram indicates for a metal three stable domains at certain regions of potential and pH that are known as immunity, corrosion, and passivity. Figure 2.9 present the Pourbaix diagram for iron at 25 °C.

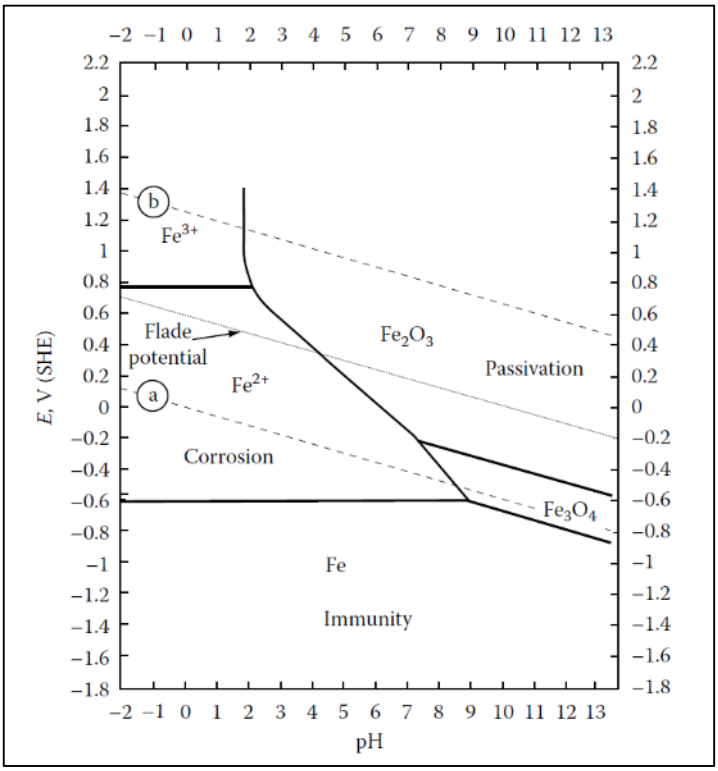

Figure 2.9 Pourbaix diagram for Fe at 25 °C. Dashed lines a and b represent the reaction of reduction for protons and oxygen, respectively (Marcus, 2017).

In the immunity region, the reaction proceeds in the direction of reduction of metallic ions; therefore, the metal is protected. In the corrosion region, the metal is oxidized to a soluble ionic product. Whereas in passivity zone the metal is oxidized, but its ionic species generate a protective oxide layer on metal surfaces that impede the corrosion reaction. In Figure 2.9, it can see that iron can react with protons in acidic and neutral environments, with the evolution of hydrogen. In basic solutions, iron is resistant to corrosion because the formation of iron oxides on the surface, such as Fe_2O_3 and Fe_3O_4, which are not easily dissolved by reaction with hydroxyl ions. This corresponds to what is observed in practice.

Most metals and alloys that resist well against corrosion, *passive metals*, such as stainless steels, nickel-based alloys, titanium, etc. are in a passive state, i.e., they have a small layer of oxide on their surface that separates the metal from its environment. This passivity can be broken electrochemically, chemically or mechanically depending on conditions of exposures; therefore, corrosion can take place (Landolt, 2007). On the other hand, metals that are film free, *active metals*, such as low-alloy steels, are more likely to oxidize and may be actively corroded or generate a oxide layer as a result of their interaction with the environment, as mentioned above.

In this context, electrochemical techniques are useful to evaluate the active o passive behavior of a metallic material as well as the kinetics of corrosion reactions. Since electrochemical reactions involve electron transfer, a valid way to quantify the rate of the reaction is by measuring the intensity of current on an electrode/electrolyte interface. Faraday's law establishes this relationship:

$$\mathrm{C} = \frac{i_{\mathrm{corr}}\mathrm{WA}t}{\mathrm{zF}} \qquad \text{(Equation 2.2)}$$

where C, i_{corr}, W, A, t, F and z are the weight loss due to pure corrosion (g), corrosion current density ($A \cdot cm^{-2}$), atomic weight ($g \cdot mol^{-1}$), surface area of the sample (cm^2), time (s), Faraday constant, and charge number, respectively. However, in an electrochemical

reaction, the anodic and cathodic reactions occur with the same magnitude, but oppositely, thus, the current measured in an electrode under normal conditions is equal to 0.

One of the most used techniques for quantifying the current density in an electrode/electrolyte interface is by means potentiodynamic polarization where the current is measured as a function of potential (polarization curve) (Landolt, 2007). To measure a potentiodynamic polarization curve, a DC source is used (potentiostat) with a three-electrode arrangement comprising the working electrode, the counter electrode, and a reference electrode as shown in Figure 2.10. The potentiostat changes the potential of the working electrode related to the reference electrode and registers the current intensity transferred between the working electrode and the counter electrode. Depending on the applied potential, the working electrode can behave as an anode or as a cathode and favor the oxidation or reduction reactions on its surface, respectively. Figure 2.11a shows a potentiodynamic polarization over a wide range of potential. Current density is determined by extrapolation of the linear part of the curve in the active region, near zero-current potential, as shown in Figure 2.11b.

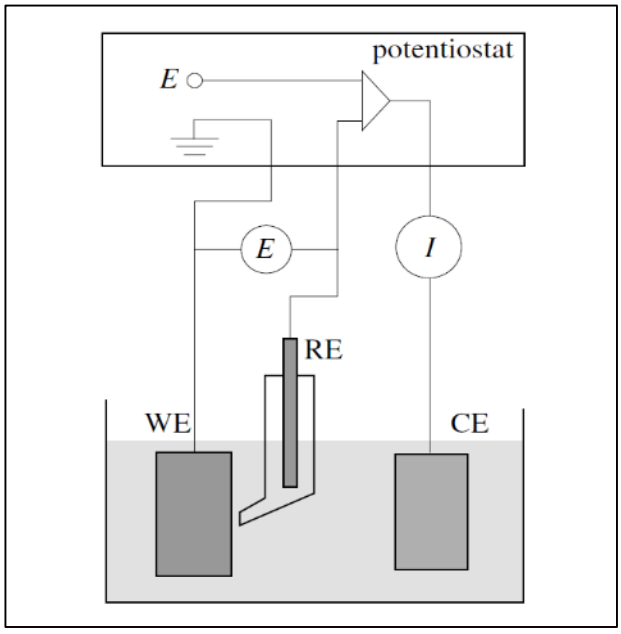

Figure 2.10 Experimental set up for potentiostatic polarization. WE: working electrode, RE: reference electrode, CE: counter electrode (Landolt, 2007).

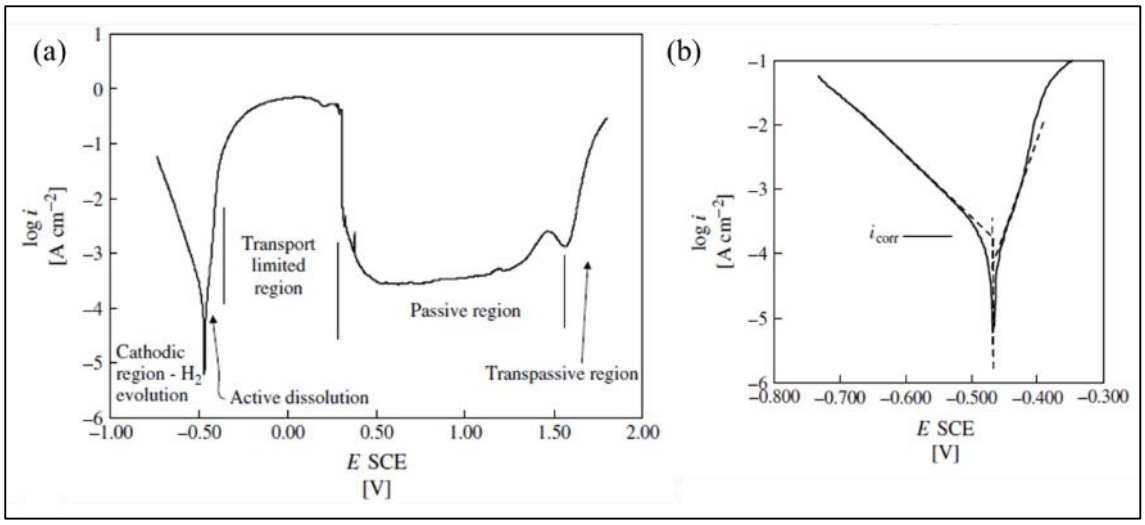

Figure 2.11 Potentiodynamic polarization curve for Fe in 0.5 M H_2SO_4: (a) full polarization curve and (b) portion of the curve near zero-current potential (Frankel & Rohwerder, 2007).

However, the polarization curve provides more information about the system than just the corrosion density current. Cathodic and anodic branch in the curve gives information about cathodic and anodic reactions. Therefore, the anodic branch gives information about the behavior of a metal in a determined system. Figure 2.11a indicate different regions; at potentials near zero-current, an active dissolution of the metal is present. As the applied potential increased further, a region of limiting current is observed where the reaction is limited by mass-transport of the dissolution product away from the surface. As potential increases, current density decrease as a result of the formation of a thin protective passive film. Finally, at very high potentials, in the *transpassive* region, the current increase again with the evolution of oxygen on the electrode surface (Frankel & Rohwerder, 2007).

2.2.3 Flow-accelerated corrosion

The corrosion rate of metals in a fluid environment is significantly higher than that in a stagnant environment; this behavior is commonly denominated as *flow-accelerated corrosion* (FAC). This phenomenon has been studied for many years in pipeline systems (Ahmed, 2010; El-gammal et al., 2010; Kain, Roychowdhury, Ahmedabadi, & Barua,

2011; Landolt, 2007). According to Heitz (1990, 1996), the corrosion rate should increase with increasing flow velocity by the action of shear stress on corrosion product film covering the pipe walls and by mass-transport consideration, especially increase in oxygen diffusion. However, Li and co-workers (Li, Pots, Brown, Kee, & Nesic, 2016) reported the wall shear stress alone, produced in multiphase flow patterns covered, is insufficient to damage the protective rust layers mechanically. Whereas, Zhang & Cheng (2009) and Tian & Cheng, (2008) investigated the corrosion behavior of X65 pipeline steel under different hydrodynamic conditions using rotating cylinder electrode apparatus in simulated oil/water emulsion. They proposed that mass-transfer of oxygen play an important effect in the cathodic reaction of X65 steel at the study conditions indicating that electrode rotation accelerates the oxygen diffusion and the cathodic reduction. Similar conclusions were obtained by Jiang et al. (Jiang, Chai, Su, & Yang, 2017) in the study of a low alloy steel under at different velocities using a flow loop and rotating cylinder electrode systems.

Therefore, the mass transfer coefficient is the main parameter used to describe flow-accelerated corrosion for iron according to the following equation (Prasad, Gopika, Sridharan, Parida, & Gaikwad, 2018):

$$M = \frac{(C_{eq} - C_b)\theta}{\frac{1}{k} + (1-f)\left[\frac{\delta_0}{D} + \frac{1}{K_m}\right]} \qquad \text{(Equation 2.3)}$$

Where M is the FAC rate (kg m^{-2} -s), C_{eq} (kg m^{-3}) and C_b (kg m^{-3}) are the equilibrium concentration (solubility) of ferrous ion and the bulk concentration of ferrous ion respectively, θ (dimensionless) is the porosity of oxide layer, δ_0 is the thickness of oxide layer (m), D is the diffusion coefficient ($m^2 \cdot s^{-1}$) of ferrous ions, κ is the reaction rate constant (m s^{-1}) for ferrous ion production in the base metal, ' 1-f ' is the fraction of ferrous ion available for transport to fluid (a fraction 'f'of the ferrous ions produced in the base metal get deposited and remaining fraction ' 1-f ' is what is transported to fluid) and K_m ($m \cdot s^{-1}$) is the mass transfer coefficient for ferrous ion transport to fluid.

On the other hand, FAC usually causes an increase in surface roughness. Indeed, carbon steel exposed to turbulent conditions often exhibits characteristics of surface features, such as orange peel appearance elongated in the flow direction (Kain et al., 2011). According to Landlot (2007) the corrosion rate increase as the surface roughness increment because a flow disturbance causes a locally higher mass-transport this premise is supported by Chilton-Colburn analogy that relates mass transport coefficient and friction coefficient of the surface.

Other factors such as temperature (Madasamy, Mohan, Sylvanus, Natarajan, & Rani, 2018), water chemistry (e.g. dissolved oxygen, pH value) (Mcgrady et al., 2017), and some alloys of the material (e.g.% chromium in steel) (Jiang et al., 2017) can modify considerable de FAC rate.

2.3 Erosion-corrosion

Erosion-corrosion (E-C) is a complex mode of material deterioration observed with exposure to erosive wear in corrosive media. Slurry-induced E-C of metallic materials is customarily described as material degradation in which mechanical wear by impinging and sliding solid particles suspended in an electrolyte interferes with the electrochemical reactions at the metal/electrolyte interface (Huth, 2011), and vice versa; the electrochemical processes alter the mechanical wear. This wear process is of common occurrence in several industries such as oil and gas, mining and metallurgy generating significant losses in productivity, owing to the costs associated with the replacement of critical components, such as pump cases, impellers, valves, and turbines (Wood, 2006, 2010).

2.3.1 Erosion and corrosion interaction

Extensive experimental works (Guo, Lu, & Luo, 2005; Islam & Farhat, 2013; Lu, Lu, & Luo, 2011; Lu & Luo, 2006; Meng, Hu, & Neville, 2007; Neville, Reyes, & Xu, 2002; Stack & Abdulrahman, 2010; Wood & Hutton, 1990) had demonstrated clearly that erosion and corrosion in flowing slurry would enhance each other resulting in a mass loss

of material greater than expected for the summation of mass loss due to pure erosion and pure corrosion. This additional mass loss is commonly referred to as *positive synergism* and presents a major issue in understanding the degradation metal process. The total mass loss during erosion-corrosion can be expressed by Equation 2.4 (ASTM International, 1994):

$$T = E_o + C_o + S \qquad \text{(Equation 2.4)}$$

where T, is the total mass loss rate of the material, Eo is the erosion rate in the absence of corrosion, Co is the corrosion rate in the absence of erosion and S is the synergistic component which has been defined as follow (ASTM International, 1994):

$$S = \Delta Ce + \Delta Ec \qquad \text{(Equation 2.5)}$$

where ΔCe is the change in corrosion rate due to erosion (*erosion-enhanced corrosion*), and ΔEc is the change in erosion rate due to corrosion (*corrosion-enhanced erosion*). In some cases depending on the study system the synergic effect can reach up to 35 to 50 % of the total weight loss in a metal (Aminul Islam, Farhat, Ahmed, & Alfantazi, 2013; A. Neville, Hodgkiess, & Xu, 1999; Yang & Cheng, 2012; Yin & Li, 2008). Sometimes erosion-corrosion mass loss can be lower than the sum of pure erosion and pure corrosion. In that case, the effect is called *antagonist effect* or *negative synergy*.

The synergistic/antagonist between erosion and corrosion has received significant attention in the last years because its mechanism is not thoroughly understood due to the influence of multiples factors in the system, some of them were reviewed in the previous sections. In the context of this thesis, only positive synergism will be reviewed.

2.3.1.1 Corrosion−enhanced erosion (ΔEc)

Different observations have been done (Guo et al., 2005; Gutman, 2002; Heitz, 1990; Islam & Farhat, 2013; Lu & Luo, 2015) related the fact that corrosion may enhance erosion rate. Postlethwaite (1981) proposed that corrosion increase the erosion rate by roughness metal surface because the erosion is very sensitive to the impact angle of the

solid particles. Whereas Matsumara (1994) suggested that corrosion enhanced corrosion through the elimination of the work-hardened layer. Thus, particles can penetrate deeper into the surface and remove material. On the other hand, it has been proposed that corrosion can reduce the wear resistance of the materials by the degradation of mechanical properties of the surface. This has been demonstrated experimentally by Lu and co-workers (Guo, Lu, & Luo, 2006; Lu & Luo, 2006, 2015). They studied *in-situ* surface hardness of a carbon steel in different corrosion environments (acidic, neutral and alkaline). They found that surface hardness degradation depends heavily on the electrolyte chemistry in acidic environments and indicate that corrosion-induced surface hardness degradation would be the dominant mechanism of corrosion-enhance erosion. Other mechanisms include selective corrosion attack at grain boundaries resulting in increased susceptibility of grain removal by erosion (Neville et al., 1999) and, localized attack of flakes formed by repeated impacts of solid particles (Li, Burstein, & Hutchings, 1995).

2.3.1.2 Erosion−enhanced corrosion (ΔC_e)

The increase of corrosion rate in presence of solid particles has been frequently reported (Aminul Islam & Farhat, 2015; Aminul Islam et al., 2013; Xie, Alpas, & Northwood, 2003a; Yang & Cheng, 2012). In this context, it generally accepted that successive particles impacting the surface lead to continuing removal of material and corrosion products which increase surface effective area and expose fresh material for the electrochemical reactions take place. On another hand, as discussed in Section 2.2.3, the corrosion rate is very sensitive to the transport-mass coefficient. According to some authors (Hu & Neville, 2005; Malka, Ne , & Gulino, 2007; Neville et al., 2002; Zhou, Stack, & Newman, 1996) erosion can accelerate corrosion reactions significantly due to increase in mass transfer coefficient mainly by increasing local turbulence when particles interact with the boundary layer and by the increase in surface roughness on the surface. In addition, Xie, Alpas, & Northwood (2003a, 2003b) have studied the electrochemical properties of an AISI 1020 steel at different erosion conditions. They reported that

deformed surfaces by erosion are electrochemically activated; thus, the corrosion rate is exponentially related to the increase of stored strain energy on the surface.

2.3.2 Factors influencing erosion-corrosion

A major issue in approaching the understanding of erosion-corrosion material loss processes is the large number of variables involved since multiple factors can act simultaneously or interact between them, affecting considerably the type of material removal mechanisms involves in the wear process. Thereby, a comprehensive understanding of the erosion-corrosion mechanisms is practically important to establish mitigation strategies.

In this context, numerous studies have been focused on the influence of different variables on E−C wear, most of them described in the previous sections, as for example the properties of the erodent (Arabnejad et al., 2015; Clark & Hartwich, 2001; Desale et al., 2006; Lindgren & Perolainen, 2014), particle impact angle (Andrews, Giourntas, Galloway, & Pearson, 2014; Burstein & Sasaki, 2000; Islam & Farhat, 2014; Jana & Stack, 2005), concentration and velocity of particles (Dasgupta et al., 1998; Islam & Farhat, 2017; Stack, Zhou, & Newman, 1996; Telfer, Stack, & Jana, 2012; Tian & Cheng, 2008; Turenne et al., 1989; Yang & Cheng, 2012), properties of the target material (Alam et al., 2015) and slurry chemistry (Guo et al., 2006; Lu & Luo, 2015), which have focused mainly on assessing the materials' durability (Andrews et al., 2014; Giourntas, Hodgkiess, & Galloway, 2015; Islam & Farhat, 2017; Rajahram et al., 2009). It has been well established that not all the parameters of a system contribute to the response in equal degree (Montgomery, 2017). Therefore, the extent of E−C rate in a determined system metal-electrolyte/slurry can be attributed mainly to some key variables. Some authors have suggested that the particle velocity, the impact angle and the chemistry of the slurry are the most determinant in the field and laboratory trials (Meng & Ludema, 1995; Meng et al., 2007; Rajahram, Harvey, & Wood, 2010). Figure 2.12 summarizes the principal factors contributing to the mechanical and electrochemical aspects of erosion and corrosion, respectively.

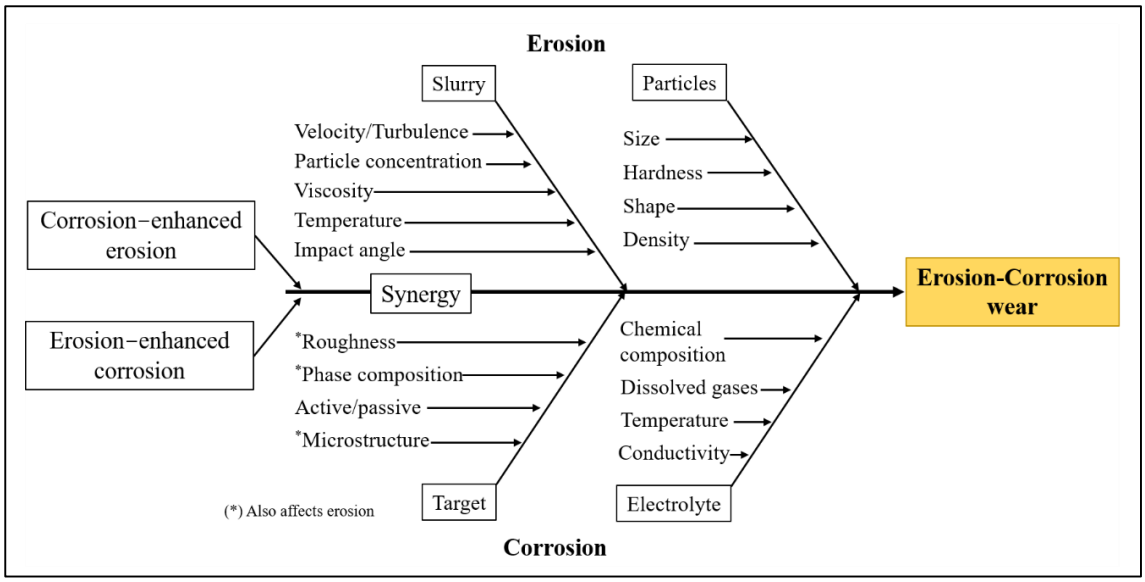

Figure 2.12 Fishbone diagram of the erosion−corrosion wear summarizing the principal parameter affecting the erosive (top) and corrosive (bottom) damage.

From the statistical point of view, the study of interactions between all the parameters is necessary for characterizing the full effect that a particular factor has on the processes, as is the case of E-C. However, only a few studies have been aiming at quantifying the effects of interactions between the relevant parameters in E-C (Jana & Stack, 2005; Meng et al., 2007; Rajahram et al., 2010). A possible tool for representing how the interaction between two parameters affects the total E-C rate is E-C mapping. In this field Stack and co-workers (Jana & Stack, 2005; M. . Stack, Corlett, & Turgoose, 2003; M. M. Stack, Abdelrahman, & Jana, 2010; Stack et al., 1996; Telfer et al., 2012) have done a great contribution employing this approach where the effects of combining applied potential, pH, particle concentration, and fluid velocity has been visualized for a range of target materials as shown in Figure 2.13. However, in order to generate a map, the significant parameters have to be known a priori.

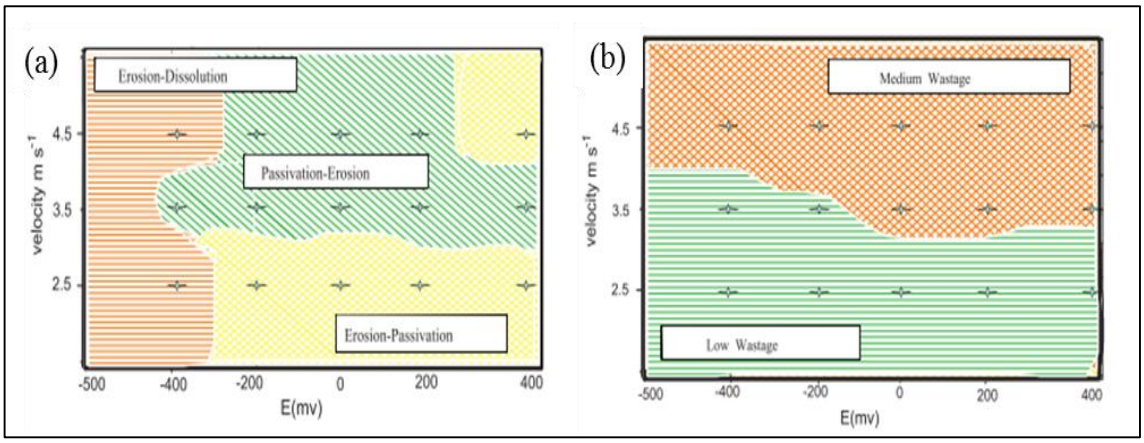

Figure 2.13 Erosion-corrosion (a) mechanism maps (b) wastage maps for carbon steel in aqueous environment at impact angle 15° (Stack & Abdulrahman, 2012).

Another tool for the study of multivariate systems is the design of experiments (DOE). This method provides a systematic approach for the collection, analysis, and interpretation of a large amount of data, where the effect and statistical significance of each factor can be determined, and where the interaction between individual parameters can also be considered. However, up to now, only Meng et al. (2007) and Rajahram et al. (2010) have explored this approach for the study of E-C of super-duplex and austenitic stainless steels by chloride-containing silica sand slurry.

2.3.3 Erosion-corrosion evaluation

Erosion-corrosion damage can be evaluated using different devices, which are coupled usually to an electrochemical system in order to evaluate the corrosion resistance of the material as well as the contribution of synergy through its components (ASTM International, 1994). The lack of agreement on which method is the most reliable is reflected in the relative popularity of different set-ups which differ in how the flow of slurry is generated such as slurry pot tester (circular flow), jet impingement (projected flow), Coriolis tester (flow by centrifugation), or flow loop (flow by pipes). The slurry pot tester and slurry jet tester have become the two most popular test arrangements, being used in almost 50% of recently published research (Javaheri et al., 2018).

2.3.3.1 Slurry pot tester

In slurry pot tester, different configurations can be implemented for the assembly of samples, which generally consists of specimens supported on a frame or shaft that are rotated at a pre-set speed in a pot full of a slurry of known composition. Within these the rotating cylinder electrode (RCE) has been widely used (Silverman, 1999, 2004, 2005; Walsh, Kear, Nahlé, Wharton, & Arenas, 2017), both in the study of single-phase fluids as well as multi-phase fluids. It consists in a metallic shaft (inner cylinder) that is covered by a resistant non-conductor material (outer cylinder), where a cylindrical specimen of the same thickness that the outer cylinder is placed in the middle or bottom of the inner shaft. The shaft immersed in a pot full of a slurry is rotated at a controlled speed and shake the slurry. In-situ electrochemical measurements can be made with the incorporation of an arrangement of electrodes (counter and reference electrode) to the system that with the specimen (working electrode) are directly connected to a potentiostat to perform electrochemical studies. A schematic representation of an example of RCE used in E−C evaluation is presented in Figure 2.14. The advantages of RCE according to Silverman studies (1999, 2004, 2005) are its defined hydrodynamics (turbulent flow condition even at low rotation frequency), reasonably well-defined empirical correlations, and uniform current and potential distribution on the sample surface. Compared with other devices, the RCE has the advantage of being compact and easy to assemble or modify; it does not require large electrolyte volumes or pumped flow loop. However, the use of cylindrical specimens does not allow to control a particular impact angle, so the information of the sample is collected throughout the particle impact range between 90° and 0°. In addition, the nature of the slurry flow and particle impact conditions in the pot are unknown and can only be described by reference to the nominal test conditions (Clark & Hartwich, 2001).

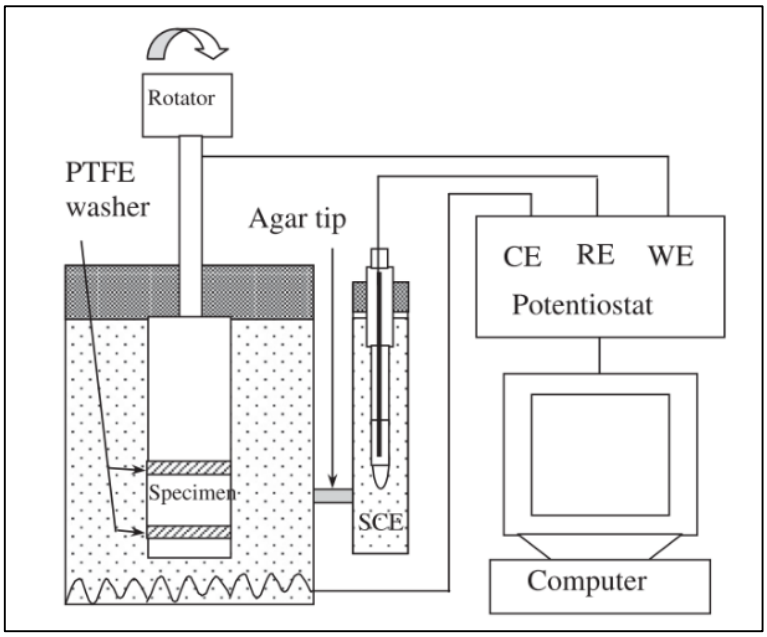

Figure 2.14 Schematic illustration of RCE for E−C measurements (Lu & Luo, 2015)

2.3.3.2 Slurry jet tester

The slurry jet apparatus consists of a large reservoir tank to store electrolyte which is pumped through an ejector to the specimen as shows Figure 2.15. The solid particles are introduced into the system by allowing the pressure drop across the nozzle, which create a region of low pressure to lift the sand to the ejector. A system of three-electrodes can be incorporated into the test rig to enable in−situ electrochemical tests, placing reference and counter electrode just before the nozzle, and connecting them with the metallic sample (working electrode). This experimental rig allows work at different velocities as well as modified the impact angle of particles by rotating the stationary specimen. However, unless the concentration of particles is very low, the particulate-particle interaction cannot be avoided, between particles from the nozzle and those that bounce off the specimen, so that non-homogeneous wear is generated in the sample which involves different types of mechanisms (Q. B. Nguyen et al., 2014; V. B. Nguyen et al., 2016). On the other hand, the direction of the jet at angles less than 90° removes the rotational symmetry of the flow pattern, making flow analysis, regarding particle impact angles, velocities, and

frequencies, much more complex (Clark & Hartwich, 2001). Besides, by practical issues, high concentrations of particles, i.e.,>40 wt%, cannot be used due to the get blocked up the nozzle.

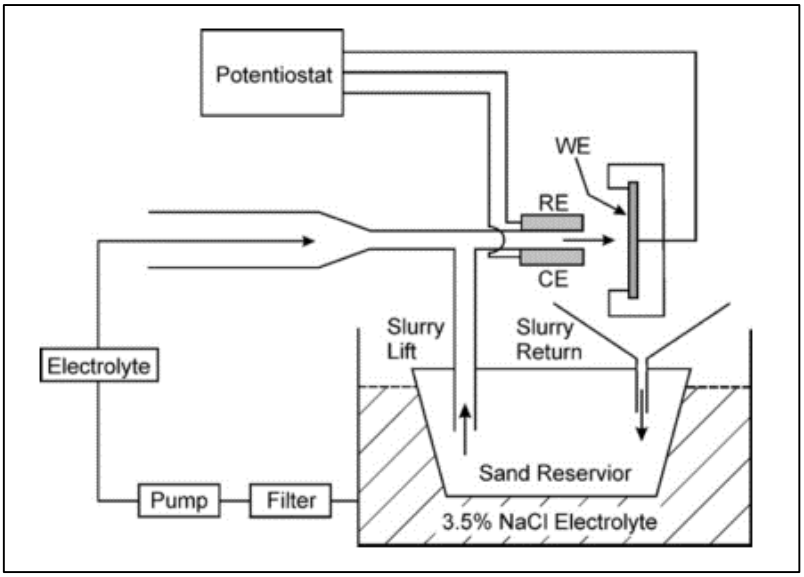

Figure 2.15 Schematic representation of a slurry jet device for E−C evaluation (Barik, Wharton, Wood, & Stokes, 2009).

2.4 The context of copper mining in Chile

2.4.1 Hydro-transport system

The hydraulic transport of solids (hydro-transport) in the form of slurry is an essential technology for transporting large volumes of raw, process and waste materials in several industries such as oil and gas, mining and metallurgy. It counts with some advantages that are translated into gross economic gains such as high efficiency in the transport of solids to a short and large distance, continuous operation and remote command, low impact on local communities and the environment, minimum maintenance among others (Chadwick, 2011). From a practical point of view, carbon and low-alloyed steels are the material of choice when building a slurry pipeline due to their good ductility-

strength relation, well-known construction procedures and availability of bulk material, especially where long transport distance is required.

Chile has important mineral deposits located in the high mountain range, most of them located above 2500 meters above sea level, which present intrinsic difficulties of high mining for its inspection, design, and operation. Therefore, the hydraulic transport of solid it is a fundamental stage for the development of the mining process in copper mining (Juan Rayo Capacitación, 2013). During the processing of copper mineral, three types of slurries are generated: ore pulp (slurry of crushed and ground mineral), copper concentrate and copper tailings (slurry of mineral waste once the copper has been extracted); among which, the concentrate and tailings slurries are most commonly transported using low-carbon steel pipelines. Due to the Chilean geography, most of the pipelines are classified as long, operating to date more than 25 pipelines to transport ore, concentrate or tailings, with over 5 km distance (Minería Chilena, 2014).

2.4.2 Copper tailing

A tailing is defined as the solid waste between sand and silt size resulting from a concentration process and which is produced, transported and deposited as sludge (COCHILCO, 2015). In copper mining, the tailings are produced in the step of sulfide copper concentration by flotation and correspond to waste materials once produced sulfide copper concentrate. The tailings fraction is poor in mineral elements of interest initially extracted. Their chemical and mineralogical composition, mainly dominated by clays and alumina, depends directly on the ore composition. On the other hand, their physical characteristics (size, percent solids, etc.) depend on the characteristics of the concentration processes; at present, the particle size is under 200 µm according to JRI study (JRI & INNOVA CORFO, 2010) the mean particle size is D_{50} 52 µm and D_{84} 174 µm.

In the process of hydro-transport, copper tailings are transported from concentration plant to tailings dam through pipelines of a low carbon steel, API 5L X65 frequently, in the form of slurry, typically in concentrations ranging from 40 to 65 wt%

solid. The transport distance in these systems can vary from 20 km to 100 km depending on the distance between the concentrator plant and tailings dam as well as the geography of the place.

3 THESIS PROPOSAL

The phenomenon of erosion-corrosion has been studied extensively, yet a complete understanding of the mechanisms involved in the degradation process has not been fully developed. This is mainly due to the influence of numerous environmental variables and dependence of material and microstructural properties on the erosion-corrosion process. For this reason, any attempt to study, evaluate or predict the wear rate by erosion-corrosion damage in a given system requires a specific study of the key parameters involved in a determined system. In the case of copper tailing slurry, the presence of water and oxygen, combined with the presence of heavy metals ions, causes corrosion to the carbon steel pipe, which is accelerated by the flowing slurry and the high content of solid sand particles. As of date, there is no systematic study of the variables or mechanisms that could affect the degradation of this type of systems. Consequently, the proposed research aims at extending the understanding of erosion−corrosion for the particular case of steel used in pipelines transporting copper tailings in Chile.

3.1 Hypothesis

Degradation of low carbon steel produced by the flow of simulated copper tailings is caused by erosion−corrosion in which some system parameters determine the wear rate by either direct effect or interaction. The relative contribution of each factor to the overall wear rate is associated with a particular mechanism of damage that can be suppressed or enhanced resulting in either negative or positive synergy between erosion and corrosion.

3.2 General objective

The main objective of this thesis is to broaden the knowledge about the erosion-corrosion process for the particular case of an API 5L X65 steel used in copper tailings pipelines in Chile, providing a fundamental understanding of the mechanism underlying most significant factors on the overall rate of material degradation.

3.3 Specifics Objectives

The following specific objectives are proposed:

I. Establish an experimental method, set-up, and procedure, for determining the wear rate of an API 5L X65 steel in simulated copper tailing in the conditions of erosion-corrosion.

II. Determine the contribution, and identify the significance, of each factor and their interactions in the erosion-corrosion rate of the X65 steel at conditions typical to copper tailing transportation.

III. Determine and characterize the main erosion-corrosion mechanisms associated with each significant factor and interaction identified previously, using electrochemical characterization and surface analysis.

4 EXPERIMENTAL

This chapter details the materials and methods used in this study and describes the two stages in which the experimental work was divided. The first stage consists of the preparation and execution of factorial design to identify the significant factors involved in the process of erosion-corrosion of low alloy steel by copper tailing. Further, with the identification of significant factors, the second stage analyzes the erosion-corrosion mechanisms associated with the effect of these factors, using for this purpose, electrochemical and surface characterization techniques

4.1 Steel samples

The material used in this study is a low alloyed carbon steel, API 5L X65, hereafter referred to as X65, extracted from a pipeline after eight years of its operation. The chemical composition of the material determined by glow discharge emission spectrometry bulk analysis (Spectruma, GDA 750 HR) is presented in Table 4.1.

Table 4.1 Chemical composition in weight percentage (wt%) of the X65 used.

Material	C	Si	Mn	P	V	S	Fe
API 5L X65	0.06	0.21	1.53	0.01	0.03	0.001	Bal.

The test specimens were hollow cylinders of 15-10 mm external-internal diameter and 10 mm in height made by lathe machining. Figure 4.1 presents the microstructure of the samples, consisting of 96.2 % of ferrite and 3.8 % of perlite determined by image analysis (National Institutes of Health, n.d.). The hardness, determined using a micro-hardness tester (LECO, M-400-H) was found to be about 2.32 GPa.

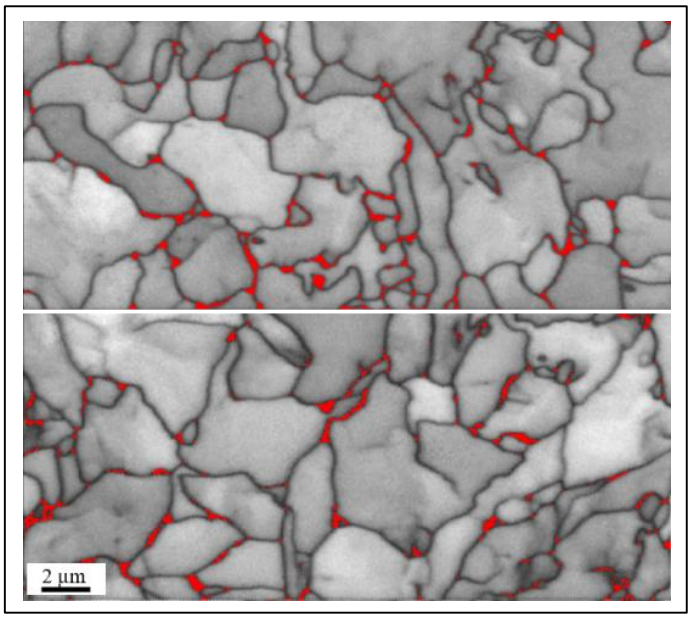

Figure 4.1 Representative images of X65 steel microstructure. Gray areas correspond to ferrite; Red areas correspond to perlite.

4.2 Specimen preparation

The surface of each sample was polished using SiC sandpaper, starting from 320 down to 1200 grit using a lathe tool to provide a uniform surface. After the final polishing, the samples were rinsed and sonicated first in distilled water and then in acetone for 180 s. The samples were dried by blowing hot air and stored in a desiccator for its preservation until the experiments. The final average surface roughness (Ra) was measured in the axial direction of some representative samples using a surface profilometer (PCE instruments, PCE-RT 1200) to be approximately R_a 0.073 ± 0.006 µm.

4.3 Erodent

The erodent used in this study was a synthetic copper tailing (SCT) prepared by mixing determined quantities of quartz and alumina of selected size distribution. For the preparation of the erodent, both abrasive materials were sieved separately by mesh N°80 (mesh opening 180 µm) and then mixed in a proportion of 4:1 in mass, for quartz and alumina. The particle size was chosen to best match the size distribution found typically

in Chilean copper tailings (JRI & INNOVA CORFO, 2010). The shape of the particles as seen under scanning electron microscope (SEM, Zeiss (Leo) 1550vp) is shown in Figure 4.2.

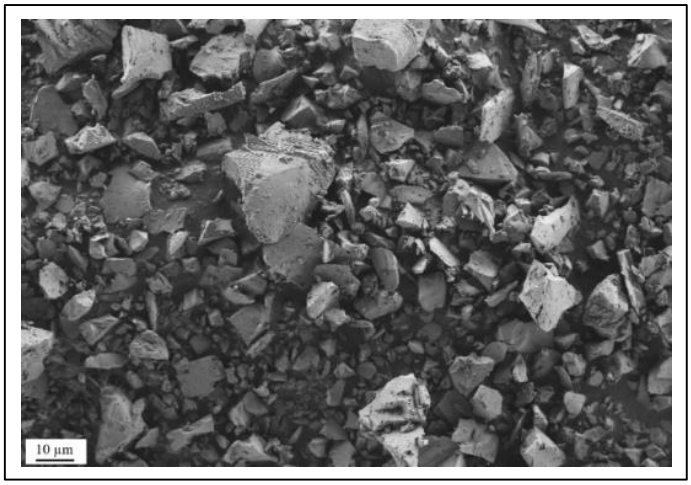

Figure 4.2 SEM image for SCT used as erodent. Magnification ×2,000.

Selected physical features of the prepared SCT are presented in Table 4.2. Density was determined by a gravimetric method using a Gay-Lussac pycnometer while the hardness of the mixed particles was measured using nanoindentation technique (Bruker, Hysitron TI 950). The circularity also referred to as form or roundness factor was obtained through analysis of SEM images employing open source image processing software, ImageJ (National Institutes of Health, n.d.), where circularity was calculated as:

$$\text{Circularity} = 4\pi \times \frac{[\text{Area}]}{[\text{Perimeter}]^2} \qquad \text{(Equation 4.1)}$$

The circularity indicator is 1 for a perfect circle (rounded particles) and 0 for an infinite elongated polygon (particles with sharp shapes). Finally, the particle size distribution and values of D_{50} and D_{90} were determined by laser scattering technique (Malvern, Mastersizer 2000).

Table 4.2 Selected physical characteristics of the SCT.

Density (g cm^{-3})	Circularity	Hardness (GPa)	D_{50} (µm)	D_{90} (µm)
2.77 ± 0.02	0.329 ± 0.04	16.84 ± 1.20	47.21 ± 0.10	142.64 ± 3.45

4.4 Experimental rig

The experiments were carried out using an in-house build system of rotating cylinder electrode (RCE). Figure 4.3a shows the configuration of the basic assembly of the system, consisting of a motor, the sample shaft, and the cell container. The motor was a 2.2 kW three-phase induction motor with a maximum speed of 24,000 rpm driven by a variable frequency drive to control the tangential velocity of the samples. The sample shaft is a steel core covered by a machined Teflon® cylinder, which allows the assembly of two samples in the lower part, separated by rubber washers, providing stiffness and electrical insulation. The slurry container is made of acrylic (maximum capacity of 300 mL) and contains four baffles mounted at 90° to each other for preventing sedimentation of the solid phase of the slurry. The concentricity of the shaft and sample are ensured by a cylindrical pivot bearing at the bottom of the slurry container. The rig does not allow for direct control of the angle by which the particles hit the surface.

Electrochemical measurements were carried out *in-situ* by the use of a three-electrode system in the RCE (Figure 4.3b) The system consists in a graphite rod as a counter electrode, Ag/AgCl (KCl saturated) as a reference and the X65 sample as working electrode. All electrodes were connected directly to a Gamry Reference 600 potentiostat for generation and collection of electrochemical data.

Further modifications were introduced in the RCE system (Figure 4.3c) with the objective of control, automatically, the temperature and oxygen concentration in the slurry. For the first objective, the pot was equipped with a heating and cooling systems consisting of a heater plate and a copper coil for pumped ice water circulation. Both systems (heat and cooling) are connected to two independent thermostats sets at the same desired temperature. The temperature of the slurry was *in-situ* measured with “NTC” type

probe. The control logic was defined so if the measured temperature is lower than the set one the heating system is activated, and the cooling system is shut down. Otherwise, the heat source is shut off, and the cooling unit starts. By this algorithm, the temperature (T) of the slurry can be established in the controlled range of 10−60 ± 1 °C.

In order to control the amount of dissolved oxygen (DO) in the slurry, two gas hoses were submerged in the slurry, one for nitrogen and one for oxygen. The actual amount of DO was monitored *in-situ* using a DO probe (Atlas Scientific, DO Kit accuracy ±0.05 ppm). The oxygen level was managed through a microcontroller integrating the gas supply valves and the oxygen probe. When the DO levels exceeded the set level, nitrogen (purity 99,999 vol.%) was added to the slurry; analogously, when the DO was below the set level, oxygen (purity 99,999 vol.%) was added. The achieved precision of control was ±1 ppm, and the nominal values of DO should be considered with this precision. It should be noted that the particular condition of nominal DO of 0 ppm is not provided, as in practice it corresponds to values between 0 and 0.3 ppm rather than absolute absence of DO.

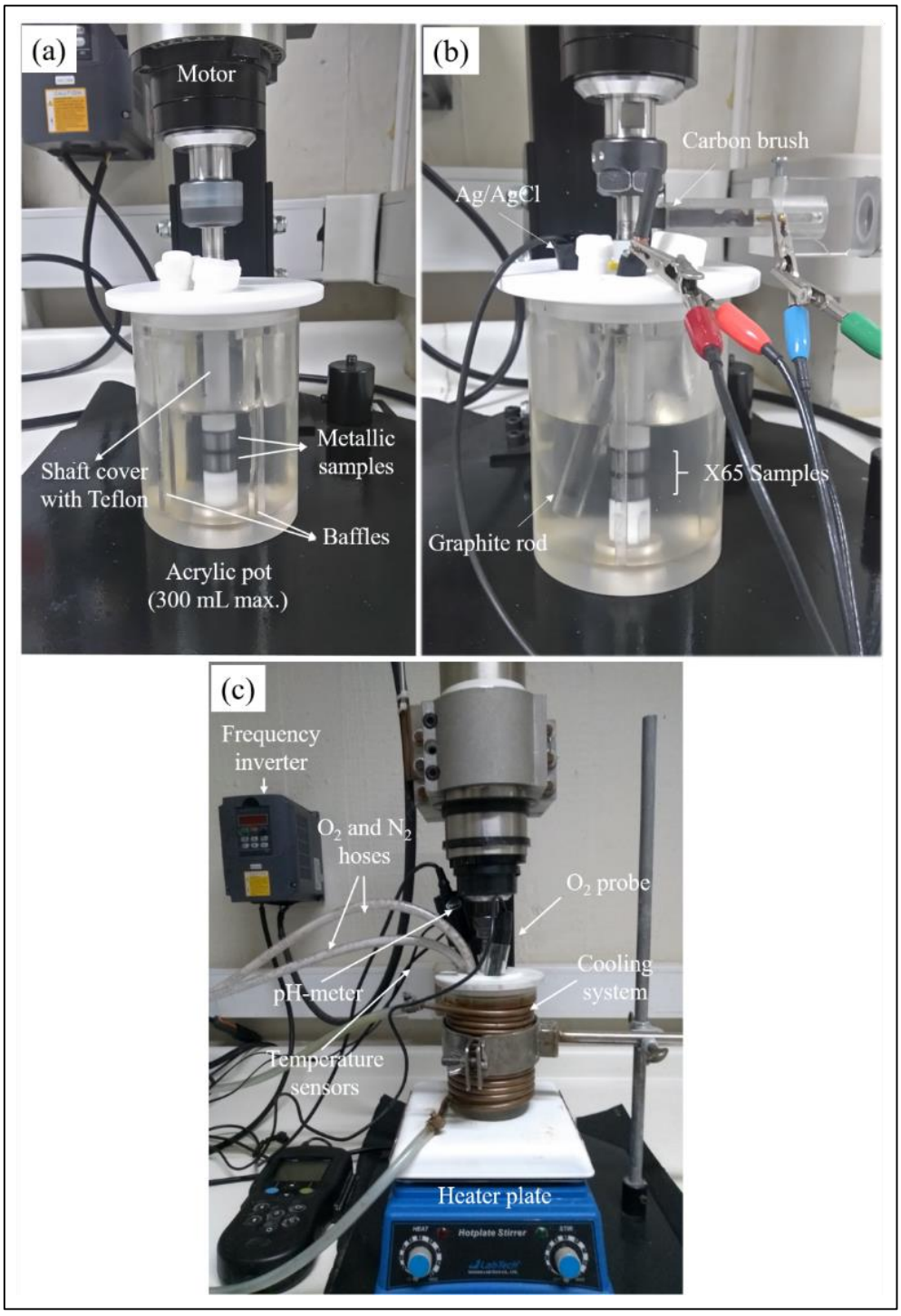

Figure 4.3 Experimental set-up (pot filled with transparent electrolyte for making the test samples visible: a) Overview of the RCE basic assembly; b) Three-electrode system; c) Complete configuration allowing the control of all the studied factors.

4.5 Stage I: Study of significant factors

4.5.1 Design of experiment

The parameters and their ranges used in this study were selected by significance in the E-C process according to literature and operational conditions in copper mining (COCHILCO, 2015; H. Meng et al., 2007; Rajahram et al., 2010). The selected parameters were velocity (V), particle concentration (P), temperature (T), pH, content of DO, and copper ion concentration (Cu^{2+}) on the slurry.

In order to study and quantify the contribution and significance of each factor and interaction, an experimental design analysis was carried out, employing a fractional factorial design, 2^{6-1} (middle fraction), with central points. This experimental configuration gives the same information as a full factorial experiment but with half of the runs. The levels and values selected for each factor are summarized in Table 4.3. In total, 35 experiments were conducted, considering all the combinations between the lowest and highest levels of each factor and a triplicate at the central level set. The direct answer, i.e., the E-C damage, was quantified by weight loss (in mg).

Table 4.3 Summary of test parameters used for the fractional factorial design of experiment, indicating the lowest, central, and highest values.

Factor	Symbol	Low level	Central level	High level	Answer
Velocity ($m \cdot s^{-1}$)	V	3	5	7	Weight loss (mg)
Particles concentration (wt%)	P	45	55	65	
Temperature (°C)	T	25	35	45	
pH	pH	5	8	11	
Dissolved oxygen (ppm)	DO	0*	5	10	
Copper ion concentration (ppm)	Cu^{2+}	0	250	500	

*effective value between 0 and 0.3 ppm

4.5.2 Erosion-corrosion test

The synthetic slurry was prepared mixing the erodent in the desired concentration with 0.1M sodium sulfate (Na_2SO_4) with the addition of copper sulfate ($CuSO_4$) to set the desired concentration of dissolved copper ions. The pH of the slurry was controlled with a pH-meter and adjusted manually by adding drops of 0.3 M H_2SO_4 or 0.3 M NaOH when pH levels deviated by more than ± 0.5 units. Temperature and DO of the slurry were controlled as described in Section 4.4. Each E-C exposure was conducted using a freshly prepared particle mixture.

The erosion-corrosion exposure was set to 75 minutes to generate measurable weight loss without significant distortion of the geometry of the test sample or attrition of the erodent.

4.5.3 Weight loss measurements

Before tests run, the weight of each sample was registered by triplicated using an analytical balance (Sartorius BP221S) with a precision of 0.1 mg. After exposure, corrosion products were removed for an accurate estimation of the total weight loss by weighing. The cleaning procedure consisted in an ultrasonic bath of the samples for 180 s, first in acetone and then in an inhibiting acid solution (Clark solution consisting of 1000 mL of hydrochloric acid, 20 g of antimony trioxide (Sb_2O_3) and 50 g of stannous chloride ($SnCl_2$)) according to the ASTM standard G1-03 (ASTM International, 1999).

Because the rig allows the exposure of two samples at the same time, for each set of factors, an average weight loss of the duplicates was calculated to determine the effective E-C rate in $mg \cdot cm^{-2} \cdot h^{-1}$. The variability of the E-C rate determined for the results of the central levels was 0.008 $mg \cdot cm^{-2} \cdot h^{-1}$, which approximates the statistical error of the experiment.

4.5.4 Factorial analysis

All the results obtained from the experimental work (shown in Table A 1, Appendix A) were processed and analyzed using Minitab 17® statistical software, where the factorial analysis was conducted to analyze the main effects and generate interaction graphs in order to determine the contribution of each factor in the weight loss.

The main effect is defined as the difference in the mean response, here the E-C rate, between two levels of a unique factor; thus, the greater the difference between the mean responses, the greater the magnitude of the factor effect. When an interaction between two factors is present, the effect of one factor depends on the level of the other factor. This is contrary to the main effect, which is the action of a single independent variable on the dependent variable.

The statistical significance was quantified with a confidence level of 95% through a normal graph of effects, whereas interaction contour plots were used to derive empirical relationships between test parameters and the resulting rate of E-C.

4.6 Stage II: Study of erosion-corrosion mechanisms

With the aim of study and characterize the effect of the significant factors in erosion-corrosion wear process, different experimental runs defined in the previous stage were repeated. The combination of parameters to be analyzed was selected from those runs that presented the highest E−C rate for the significant factor to be studied. The tests carried out considered only the variation of the significant factors separately, keeping all the other parameters constant according to Table 4.4.

Table 4.4 Experimental runs for studying of E-C mechanisms.

Analyzed Factor	Symbol	V ($m \cdot s^{-1}$)	P (wt%)	pH	T (°C)	DO (ppm)	Cu^{2+} (ppm)
Velocity	7 $m \cdot s^{-1}$	7	65	5	45	0	0
	3 $m \cdot s^{-1}$	3	65	5	45	0	0
Oxygen	0 ppm	7	65	5	45	0	0
	10 ppm	7	65	5	45	10	0
Temperature	25 °C	7	45	5	25	0	0
	45 °C	7	45	5	45	0	0
Particles	45 wt%	7	45	5	45	0	0
	65 wt%	7	65	5	45	0	0
Copper ions	0 ppm	7	45	5	45	10	0
	500 ppm	7	45	5	45	10	500

The experiments were performed in triplicate considering two tests for electrochemical measurements and one test to generate a set of samples for surface and sub-surface characterization. In the latter case, after the E−C test, the samples were extracted and sonicated for 180 s in acetone, to remove traces of particles from the surface, then dried with hot air and stored in a desiccator at vacuum conditions for further analysis.

4.6.1 Potentiodynamic polarization

Potentiodynamic polarization on samples for each treatment was conducted after one hour of exposure to the flowing slurry at the desired conditions. Anodic and cathodic curves were collected separately, polarizing the sample from open circuit potential at the scan rate of 1 $mV \cdot s^{-1}$ in either anodic or cathodic direction. The amount of corrosion current density (i_{corr}) was quantified via the Tafel extrapolation technique (Frankel & Rohwerder, 2007) and the weight loss due to corrosion was determined according to Faraday's law (Equation 2.2). The anodic reaction considered is represented in(Equation 4.2:

$$Fe \leftrightarrow Fe^{2+} + 2\bar{e} \qquad \text{(Equation 4.2)}$$

4.6.2 Surface characterization

The surface morphology of the samples was analyzed by SEM (Zeiss, Leo 1550 VP) at different magnifications inspecting the worn surface of the cylinders in the axial direction and selecting a representative image for further analysis. SEM images were complemented by elemental analysis by means of energy dispersive X-Ray spectroscopy (EDX, Oxford Instrument) coupled with the SEM equipment.

4.6.3 Sub-surface and microstructural characterization

For the study of sub-surface, the samples were prepared using standard metallographic techniques, where samples cross-sections were embedded in conductive epoxy resin., which were then cured and ground using SiC papers with grit sizes 240 (52 µm), 320 (35 µm), 400 (22 µm), 600 (15 µm), 800 (13 µm) and 1500 (8 µm). The first grinding step aimed to produce a flat surface, the duration of the subsequent steps was 5 minutes each. The final SiC grinding step was followed by two polishing steps using a polishing cloth and diamond suspensions of 3 µm and 1 µm for 5 minutes each. The final polishing step was conducted using 0.04 µm of colloidal silica suspension for 30 minutes. The samples were thoroughly rinsed in water between the different grinding/polishing steps and finally sonicated and cleaned in ethanol.

The sub-surface of the whole samples was analyzed at different magnifications first by SEM and then by EDX. Finally, the microstructural analysis of the cross-section of each sample was conducted using electron backscatter diffraction technique (EBSD). The EBSD maps of the sub-surface were obtained using the same SEM instrument described above, which is also equipped with a Hikari EBSD Camera provided by EDAX. The measurements were performed with the sample tilted at 70° towards the EBSD detector, using the acquisition parameters summarized in Table 4.5. For statistical reproducibility, at least four mappings were done for each sample in different locations.

The acquisition software was TSL OIM, version 6.2, where only the ferritic phase (BCC) was indexed according to the Miller indexes (*hkl*) for this type of steel.

Table 4.5 EBSD acquisition parameters.

Accelerating voltage	Working distance	Step size	Binning	Scan size
15 keV	22 mm	50 µm	5 × 5	12 µm × 28 µm

The data were processed using the software OIM Analysis™ version 7.0 in order to analyze local misorientations by Kernel Average Misorientation (KAM) method. KAM is a calculation of the average misorientation between each pixel in the map and its nearest neighbors, which allows the analysis of the degree of local deformation of the material. In this study, only first neighboring pixels with a misorientation angle lower than a threshold of 5° are considered in the calculation in order not to include misorientations due to grain boundaries.

5 RESULTS

5.1 Statistical analysis

5.1.1 Main factors and interactions

Figure 5.1 shows a graph of the main effects of the six factors. The main effects graph is used to observe how one or more factors influence a continuous response, here the E-C rate. For this study, the slurry velocity, particle concentration, temperature, oxygen concentration, and copper ion concentration generate an increase in the wear rate of the material when they change from their lowest to their highest level. However, the pH has a contrary effect, producing a higher wear rate when the pH changes from the higher to the lower level. The magnitude of the effect, i.e., the change in the E-C rate attributable to the change in the level of a factor, is observed to be the highest for the slurry velocity (e = 4.36 mg·cm^{-2}·h^{-1}), oxygen content (e = 2.41 mg·cm^{-2}·h^{-1}), and temperature (e = 1.32 mg·cm^{-2}·h^{-1}), producing a greater influence on the E-C rate as compared with the other factors.

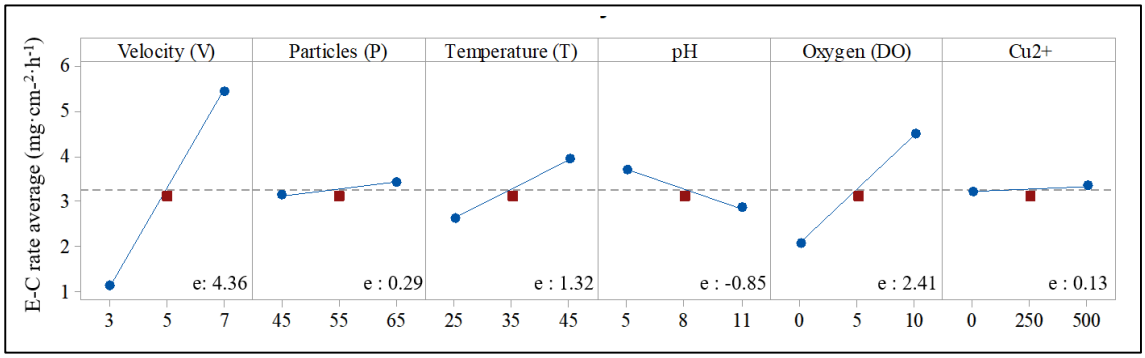

Figure 5.1 Main effects of experimental factors on the E-C rate. The magnitude of the effect (e) is shown in the lower part of each box. Color code: red– central point, blue– corner points.

Figure 5.2 summarizes the interaction effects between the minimum (blue line) and maximum (green line) values for each of the six factors, and each corresponding to a distinct interaction. The largest effect is observed for the interactions between velocity

and temperature (V×T), temperature and pH (T×pH), velocity and dissolved oxygen (V×DO), and particle concentration and content of copper ions (P×Cu^{2+}), as indicated by the slope of the curve and the distance between the maximum and minimum values.

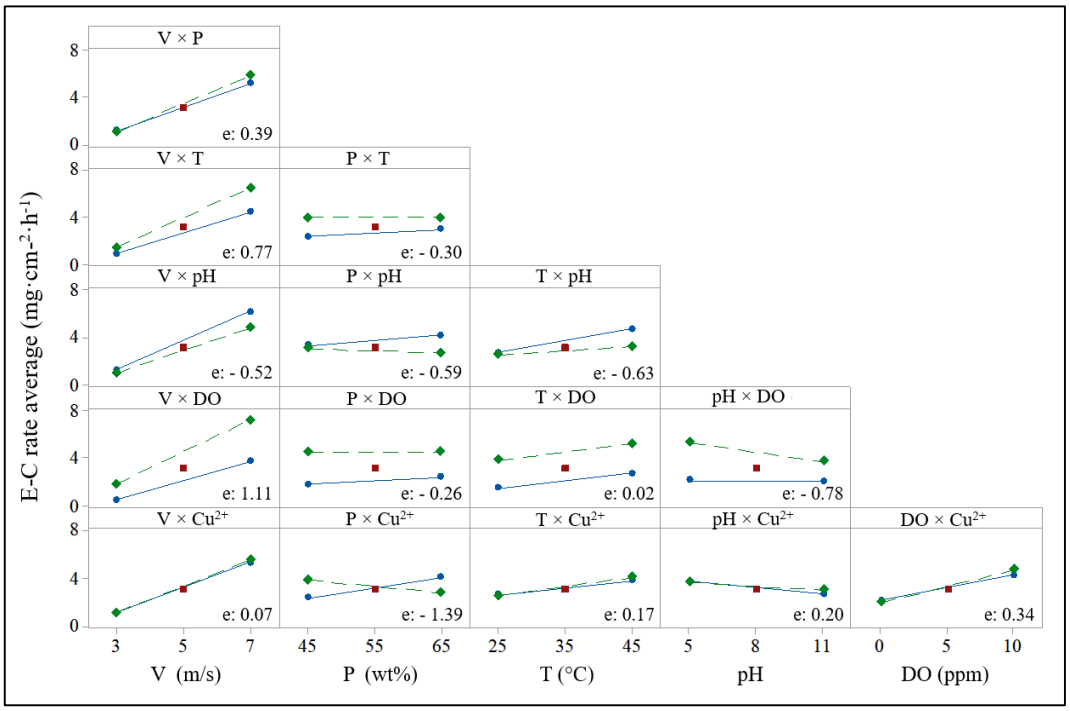

Figure 5.2 Interaction plot of factors on the overall E-C rate. The magnitude of the effect (e) is shown in the lower part of each box.

The statistical significance of the effect of each factor and the first-order interactions is shown in Figure 5.3, where the values of the effects are ordered in a normal probability graph. The red line indicates where all the points would be located if all the effects were null, and thus points located far from the line indicate a significant effect (red points). A factor or interaction is statistically significant when the observed association between the effect and the response is not random, i.e., the change in response can be attributed to the particular factor, be it an individual parameter or interaction. The factor that is found to have the strongest influence on the E-C rate is the slurry velocity, followed by oxygen concentration, the interaction between velocity and oxygen content, and temperature, with an increment in the wear rate of the material. The effect of the

interaction between particle concentration and copper content is also significant; however, it tends to decrease the rate of wear when both factors are at their highest level.

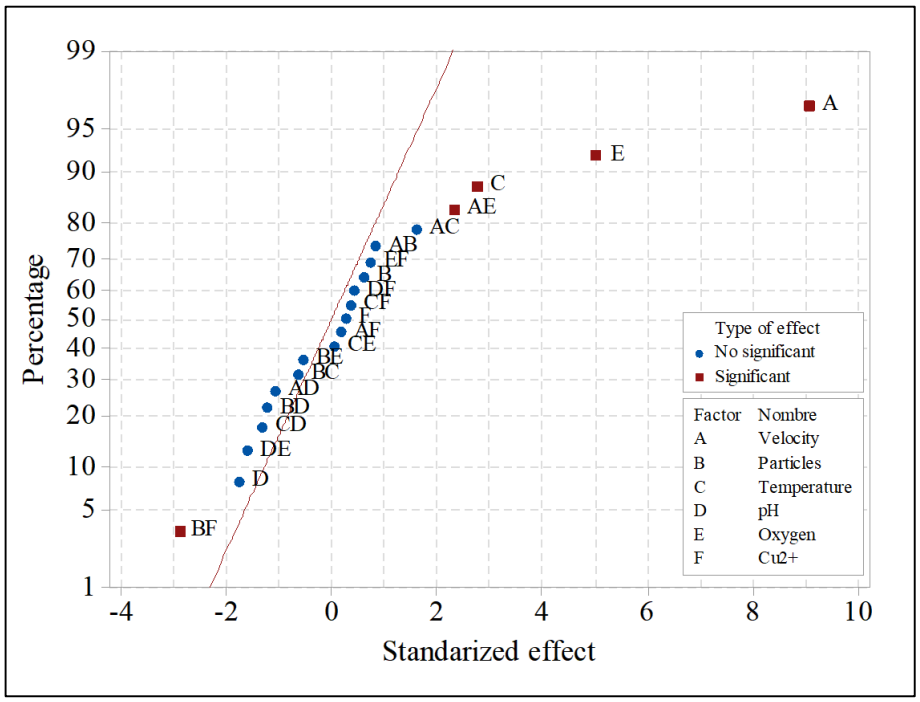

Figure 5.3 Graph of normal effects detailing the significance of each factor and first-order interactions.

5.1.2 Linear regression

A multiple linear regression equation was derived from the experimental results, representing the relationship between E-C rate measured in $mg \cdot cm^{-2} \cdot h^{-1}$ and the studied values of factors/interactions. In a general way, the regression equation is presented in the following form:

$$y = b_o + b_1X_1 + b_2X_2 + \ldots + b_kX_k + \varepsilon \qquad \text{(Equation 5.1)}$$

where y is the value of the answer (E−C rate), X_n is the value of n-th predictor (variable), b_o is an intersection constant, and b_n is the n-th regression coefficient associated with n-th variable, n taking values from 1 to k. The value of k depends on the maximum order of

interactions considered. Finally, ε represent the random error in the central points (central levels) of the experiment.

In the first approximation, the regression equation included 23 terms, considering six factors and their respective first-order interactions, neglecting possible interactions of second or higher orders (Equation 5.2):

$$\text{E–C rate} = -14.60 - 0.086\,V + 0.180\,P + 0.128\,T + 1.085\,pH + 0.272\,DO + 0.01225\,Cu^{2+} + 0.0099\,V{\times}P + 0.0192\,V{\times}T - 0.0428\,V{\times}pH + 0.0557\,V{\times}DO + 0.000076\,V{\times}Cu^{2+} - 0.00151\,P{\times}T - 0.00993\,P{\times}pH - 0.00261\,P{\times}DO - 0.000279\,P{\times}Cu^{2+} - 0.01056\,T{\times}pH + 0.00024\,T{\times}DO + 0.000035T{\times}Cu^{2+} - 0.0260\,pH{\times}DO + 0.000134\,pH{\times}Cu^{2+} + 0.000138\,DO{\times}Cu^{2+} - 0{,}170$$

(Equation 5.2)

Taking into account only the statistically significant factors and interaction, the (Equation 5.2 could be reduced to 8 terms considering only statistically significant factors/interactions:

$$\text{E–C rate} = -7.88 + 0.811\,V + 0.0716\,P + 0.0536\,T + 0.0318\,DO + 0.01287\,Cu^{2+} + 0.0370\,V{\times}DO - 0.000229\,P{\times}Cu^{2+}$$

(Equation 5.3)

The values of the standard error of the regression (S), the coefficient of determination (R^2), the adjusted and predicted R^2 determined for both equations and are summarized in Table 5.1. In should be kept in mind that (Equation 5.2 and (Equation 5.3 are reported in uncoded units (natural units).

Table 5.1 Statistical quality parameters of equation describing experimental E-C rates.

Equation	Terms	S ($mg \cdot cm^{-2} \cdot h^{-1}$)	R^2 (%)	R^2 adjusted (%)	Predicted R^2 (%)
(Equation **5.2**	23	1.35	92.33	78.28	21.50
(Equation **5.3**	8	0.93	88.28	85.25	79.32

In general, the term S represents the standard distance separating the data values from the regression line. The value R^2 indicates the percentage of deviation explained by its relationship with the variables. The value of R^2 adjusted is the percentage of response variable variation that is explained by its relationship with one or more predictor variables, adjusted for the number of predictors in the model. The predicted R^2 indicates how well the model predicts responses for new observations. Larger values of predicted R^2 indicate models of greater predictive capacity. In this context, (Equation 5.3 provided a better model and was selected for further analysis.

5.1.3 Contour plots

From (Equation 5.3 contour maps were generated using the statistically significant interactions and the resultant erosion-corrosion levels arising from the variation of these factors. Figure 5.4 shows a contour plot of the interaction between oxygen concentration and the velocity of the slurry. It is observed that the increase in velocity produces a higher wear rate compared with the increase in oxygen concentration. The highest wear rate is obtained in the region where the highest oxygen content is combined with the highest velocity.

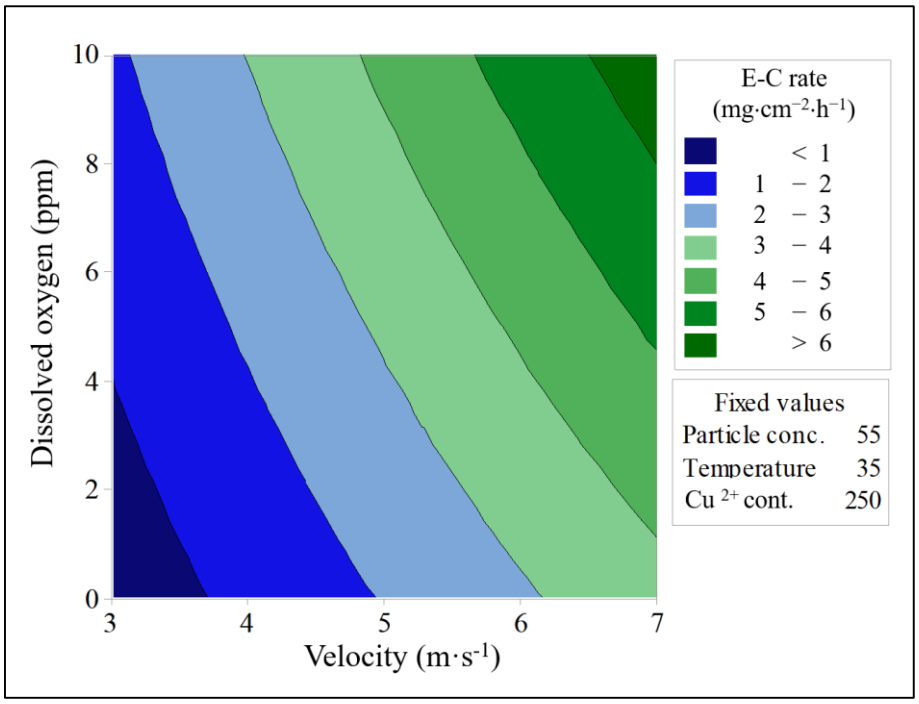

Figure 5.4 Contour plot of interaction between dissolved oxygen and the velocity of the slurry.

The interaction between particle concentration and copper ion content is depicted in the contour plot in Figure 5.5. In this case, the wear response of the material is more complex. The highest E-C rates are only observed when the factors are at opposite levels, whereas the lowest E-C rates are observed when both factors are at the same time at their lowest or their highest level. The interaction also tends to present a stable value of wear rate when both factors are close to their central level.

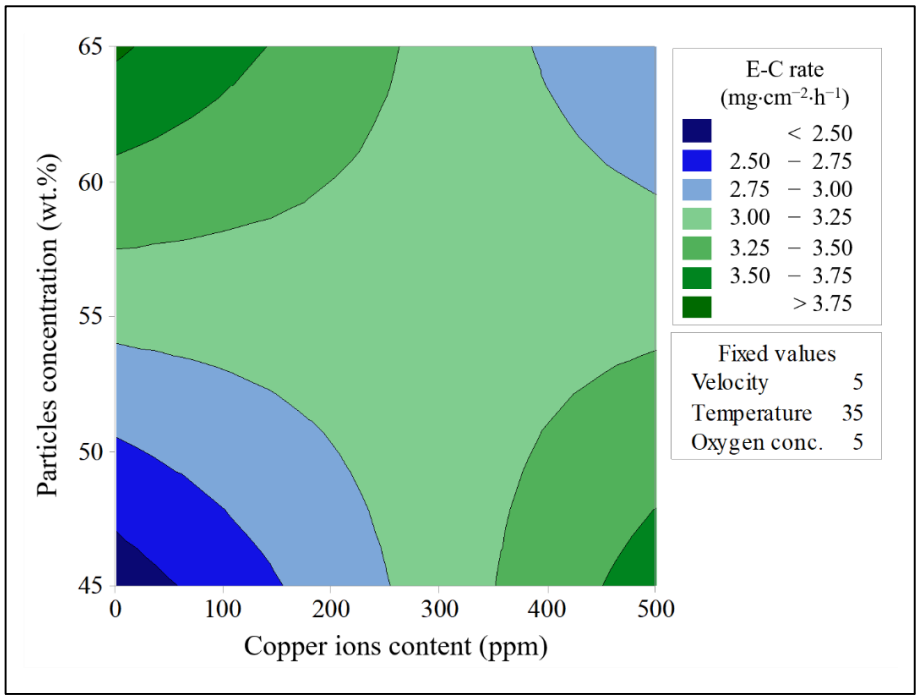

Figure 5.5 Contour plot of interaction between particle concentration and Cu^{2+} content.

5.2 Characterization of E-C mechanisms

5.2.1 SEM analysis

5.2.1.1 Effect of slurry velocity

Figure 5.6 summarizes representative SEM micrographs of the samples exposed at low (3 $m \cdot s^{-1}$) and high (7 $m \cdot s^{-1}$) velocity at 0 ppm of DO. Visible damage by plastic deformation is observed on the top surface due to the impact of slurry particles on the steel. At both velocities cutting–type-, plowing–type-, and indentation–type craters are observed on the surface, also the formation of lips and the presence of steel debris. As expected, the increment in velocity reveals an evident increase in the damage by plastic deformation, showing a higher density of craters and lips on the surface. These craters become deeper and more random at 7 $m \cdot s^{-1}$, with an increase in the presence of indentation–type craters on the surface.

The cross-sections of the samples reveal the relief profiles, the depth of craters is quantified to be on average 0.6 and 1.7 µm for the velocities of 3 and 7 $m \cdot s^{-1}$, respectively. SEM images of the sub-surface damaged at 3 $m \cdot s^{-1}$ present a profile with craters more rounded and homogeneous in depth, compared with samples exposed at 7 $m \cdot s^{-1}$ that reveal an irregular and sharp craters with areas larger than depths. At the edges of the indents, some extruded material and cracks towards the inner of the steel are observed.

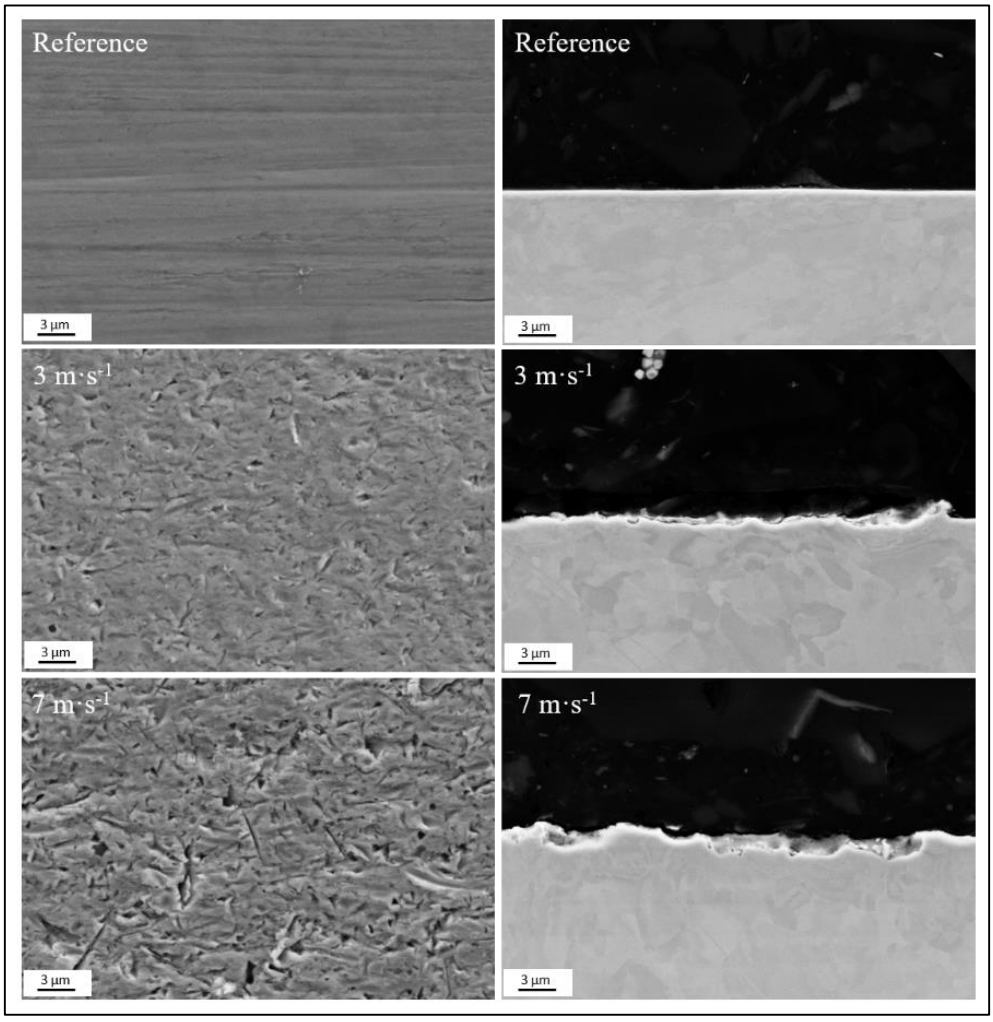

Figure 5.6 Representative SEM micrographs of the surface (left) and cross-sections (right) of samples exposed at 3 and 7 $m \cdot s^{-1}$ of the slurry keeping the other factors constant. Magnification 10,000×.

5.2.1.2 Effect of dissolved oxygen

Different surface morphology is formed after exposure to the slurry with a high content of DO (Figure 5.7). Whereas surface morphology at 0 ppm of DO shows a heavy plastic deformation, with a surface covered by craters and lips due to the impact of the particles, similar to what was seen above. The samples exposed to the slurry with 10 ppm of DO have a surface with irregular grooves of large extension and depth, where particles of erodent can be observed retained inside. The magnitude of the damage is not clear since some particles, apparently of the erodent, and deposits are found covering the surface of the steel.

This contrasting difference can also be observed in the cross-section of the samples presented in the same Figure 5.7. The SEM images of the samples exposed in a slurry at 0 ppm DO, shows a profile with irregular and sharp craters, mainly by plowing and extrusion of the steel, with an average crater depth of 1.6 μm. However, in samples exposed at 10 ppm of DO shows some deep and wide dimples through the sub-surface, with an average depth of 5.4 μm, where it is possible to observe these dimples filled with deposits and particles.

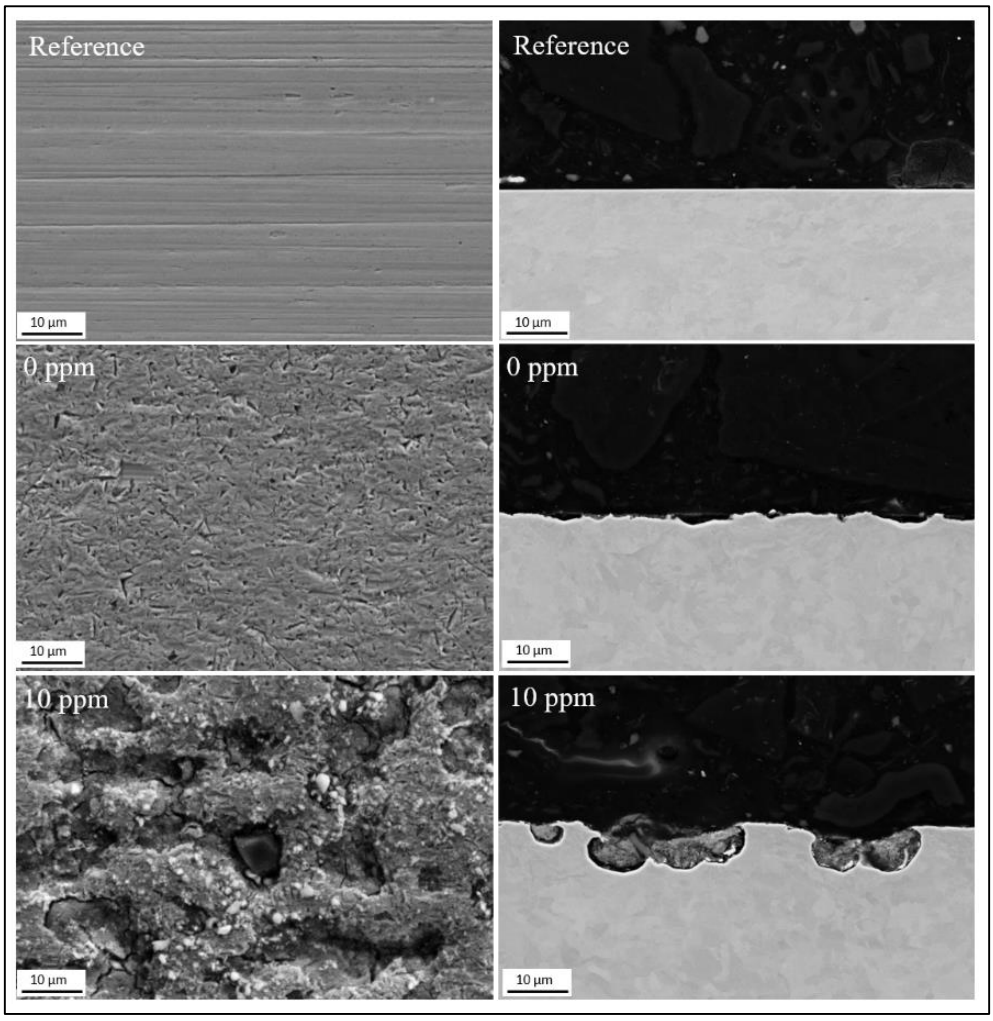

Figure 5.7 Representative SEM micrographs of the surface (left) and cross-section (right) of samples exposed at 0 ppm and 10 ppm od DO in the slurry keeping the other factors constant. Magnification 5,000×.

Figure 5.8 shows the EDX mapping on the surface and cross-section of these last samples to observe any change in the surface chemistry. There is an evident presence of oxygen, silicon and alumina on the surface, where it is possible to differentiate two well-marked areas: ones with a high concentration of oxygen and others of iron from the base metal. Areas with a high oxygen content are preferably located in the groove zones, as well as, the silica and aluminum contents, while, the iron zones are the shallower areas show in the electron images.

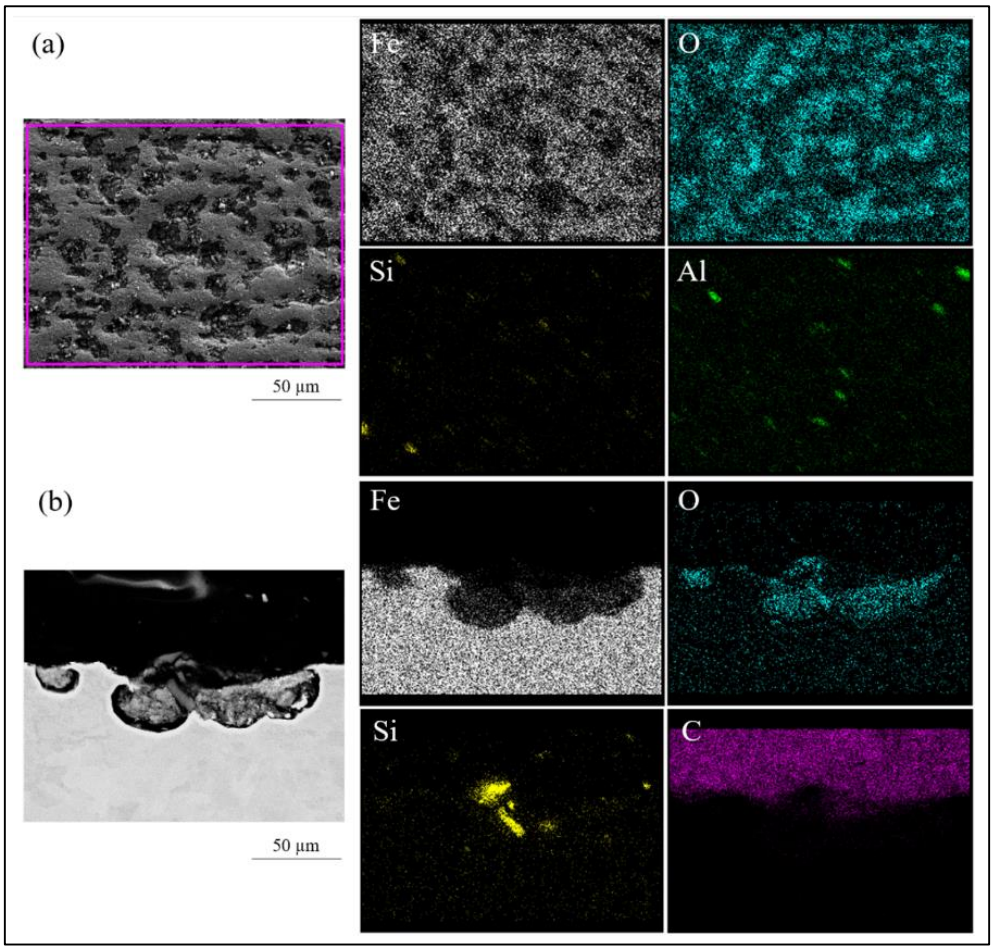

Figure 5.8 Representative EDX analysis on the: (a) top surface and (b) cross-section of samples exposed to the slurry with 10 ppm of DO. Magnification 5,000×. Carbon element in (b) (pink color) corresponds to the composition of the support resin (background).

5.2.1.3 Effect of temperature

Figure 5.9 compares the surface of samples worn at temperatures of 25 °C and 45 °C. It is observed a strong plastic deformation on the surfaces with multiple overlapping impacts, the formation of craters and extruding lips, with a high presence of indentation-type craters in both surfaces. Cross-section profile shows similar crater depths.

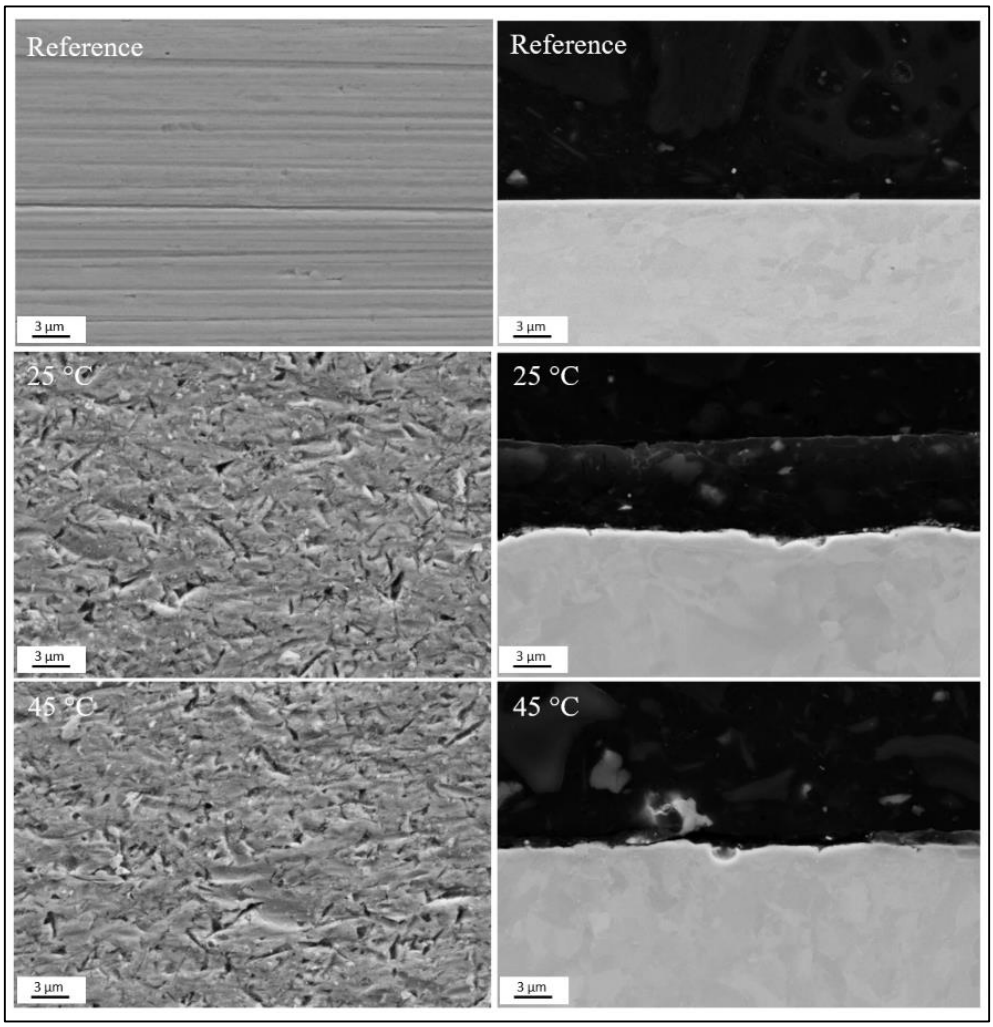

Figure 5.9 Representative SEM micrographs of the surface (left) and cross-section (right) of samples exposed at 25 °C and 45°C in the slurry keeping the other factors constant. Magnification 10,000×.

5.2.1.4 Effect of particles

SEM micrographs of the samples exposed at low (45 wt%) and high (65 wt%) concentration is presented in Figure 5.10. At both concentration different types of craters are observed on the surface, with a recurring presence of indentation–type craters on both surfaces. The specimen subject to the highest particles concentration shows stronger plastic deformation, with the highest density and depth of impact craters and lips formed on the surface in comparison with the samples subject to the lowest particles concentration.

The cross-section of the samples (Figure 5.10) shows a significant difference in the surface profile. The depth of craters is quantified to be on average 0.8 and 1.9 μm for 45 and 65 wt% in particles, respectively. SEM images of the sub-surface damaged at 45 wt% in particles present irregular craters of a shallow profile, compared with samples exposed at 65 wt% that reveal a contrasting profile with deeper sharp craters and a greater amount of extruded material.

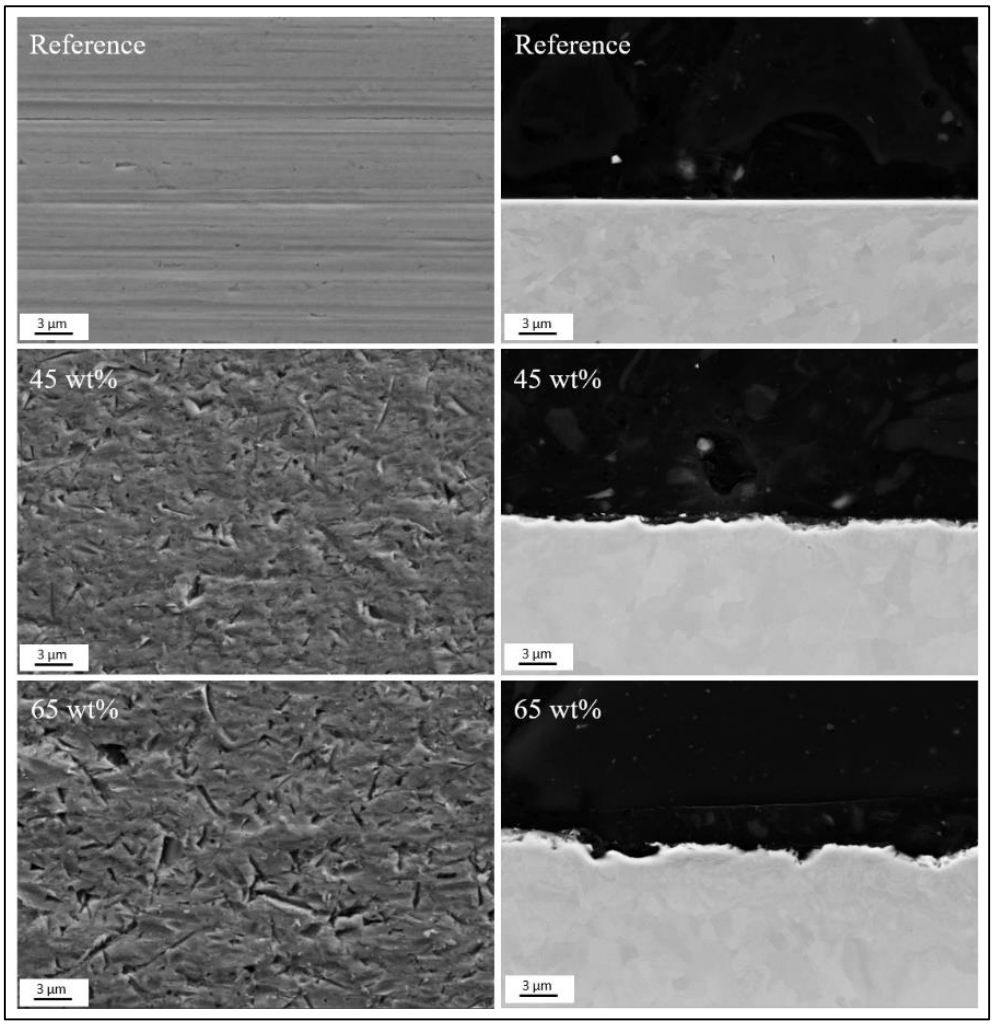

Figure 5.10 Representative SEM micrographs of the surface (left) and cross-section (right) of samples exposed at 45 wt% and 65 wt% particles in the slurry keeping the other factors constant. Magnification 10,000×.

5.2.1.5 Effect of copper ions content

The morphology of the analyzed samples (Figure 5.11) does not show significant differences to those already described for 10 ppm of DO (section 5.2.1.2) when the concentration of Cu^{2+} increase to 500 ppm in the slurry. However, the cross-section of the samples shows, in addition to the dimples filled with deposited products and particles, some white deposits near the top surface of the steel.

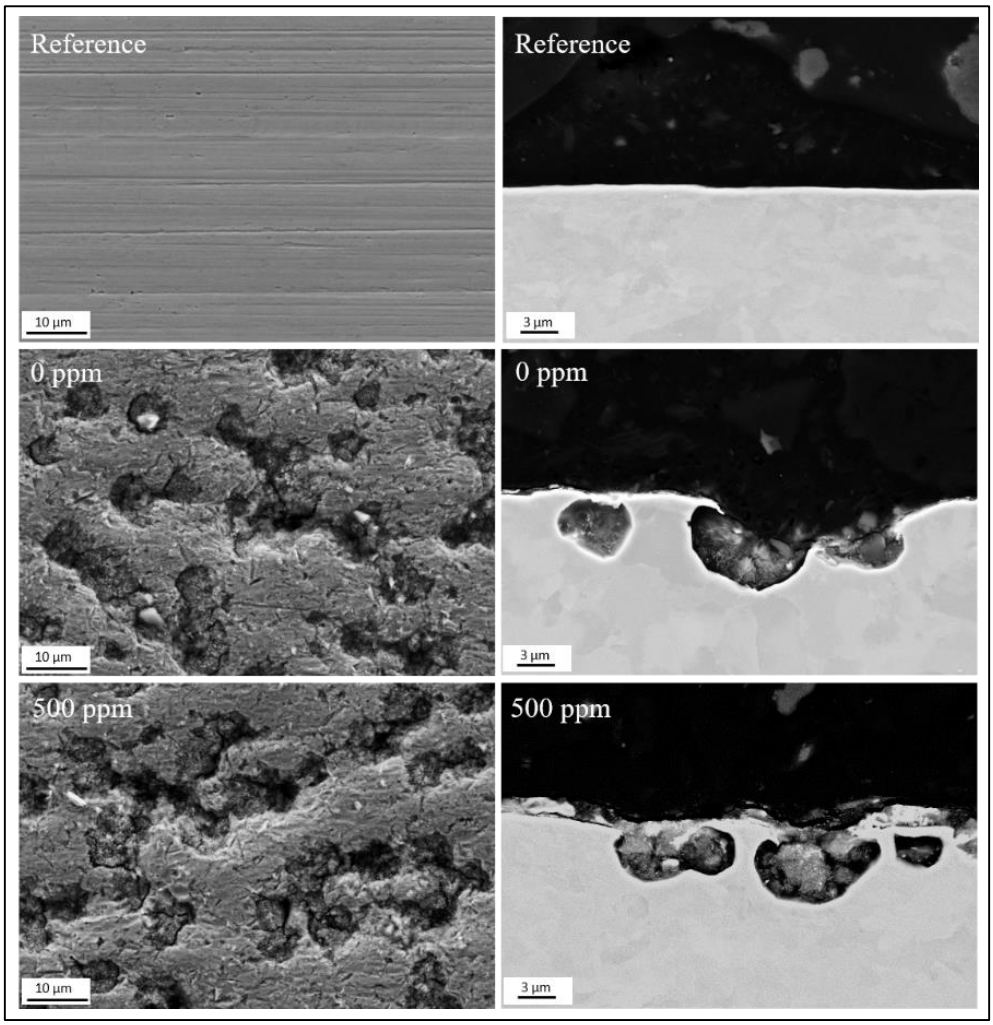

Figure 5.11 Representative SEM micrographs of the surface (left) and cross-section (right) of samples exposed at 0 and 500 ppm of Cu^{2+} ions in the slurry keeping the other factors constant. Magnification 5,000×(left) and 10,000×(right).

The EDX analysis of these last samples shows the presence of copper on the surface of the steel (Figure 5.12), near groove areas with high concentrations of oxygen and silicon. On the other hand, the cross-section shows a high content of oxygen inside the dimples, while the concentration of copper tends to be higher in the top surface of the sample.

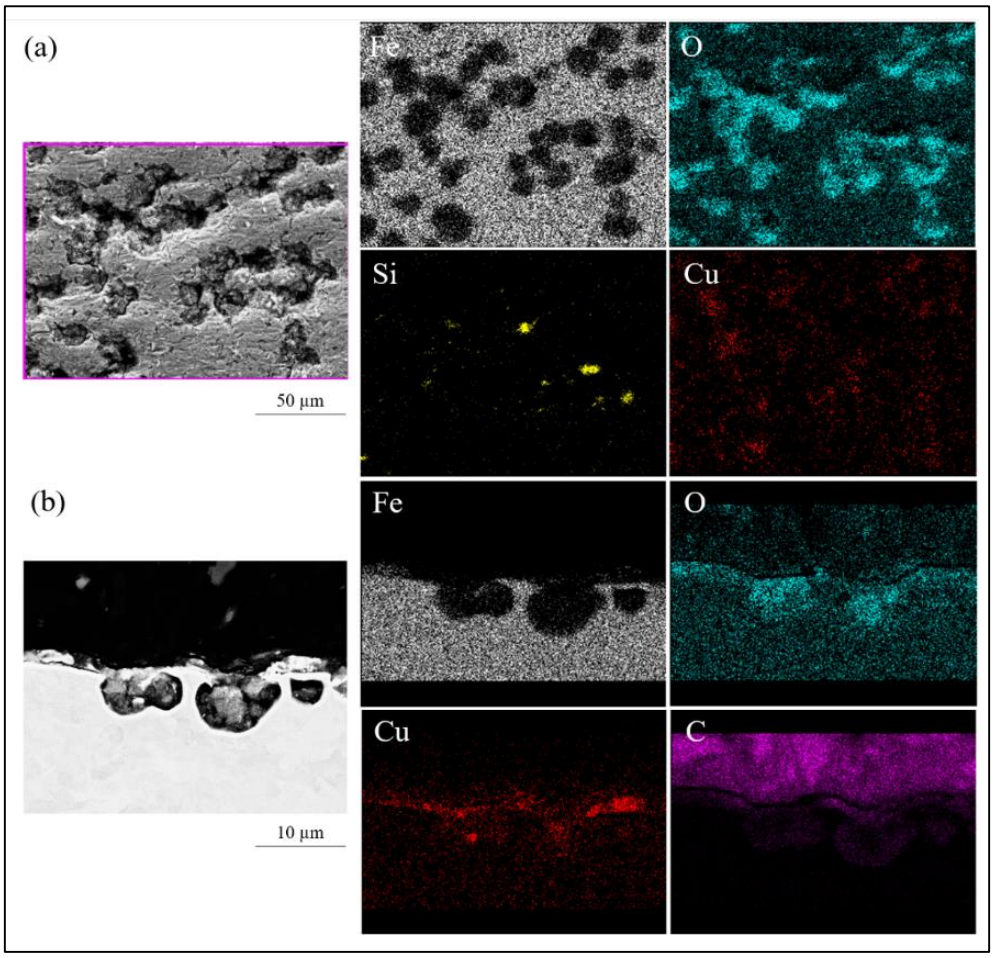

Figure 5.12 Representative EDX analysis on the: (a) top surface and (b) cross-section of samples exposed to the slurry with 10 ppm of DO and 500 ppm of Cu^{2+}. Magnification 5,000× (left) and 10,000× (right). Carbon element in (b) (pink color) corresponds to the composition of the support resin (background).

5.2.2 EBSD analysis

5.2.2.1 Effect of slurry velocity

Figure 5.13 shows the EBSD analysis of the sub-surface microstructure at different velocities of slurry flow. The reference sample, i.e., prior exposure to the slurry, has a similar sub-surface throughout the sample, except the smooth layer of smaller grain sizes at the surface that is typical for surface preparation employed in this study. After exposure to the slurry, the damage induced by impacting particles has a different appearance revealing that the grain size of the sub-surface decreases as the velocity increases. In the case of samples exposed to at 3 $m \cdot s^{-1}$, there is a top layer of deformed grains of about 1.7 μm in thickness, which is followed immediately by a typical grain structure of the bulk. Whereas, exposure to 7 $m \cdot s^{-1}$ reveals a thinner top layer, of about 2.1 μm thickness, followed by a layer of about 4.6 μm thickness consisting of micro-grains after which the nominal bulk microstructure is observed.

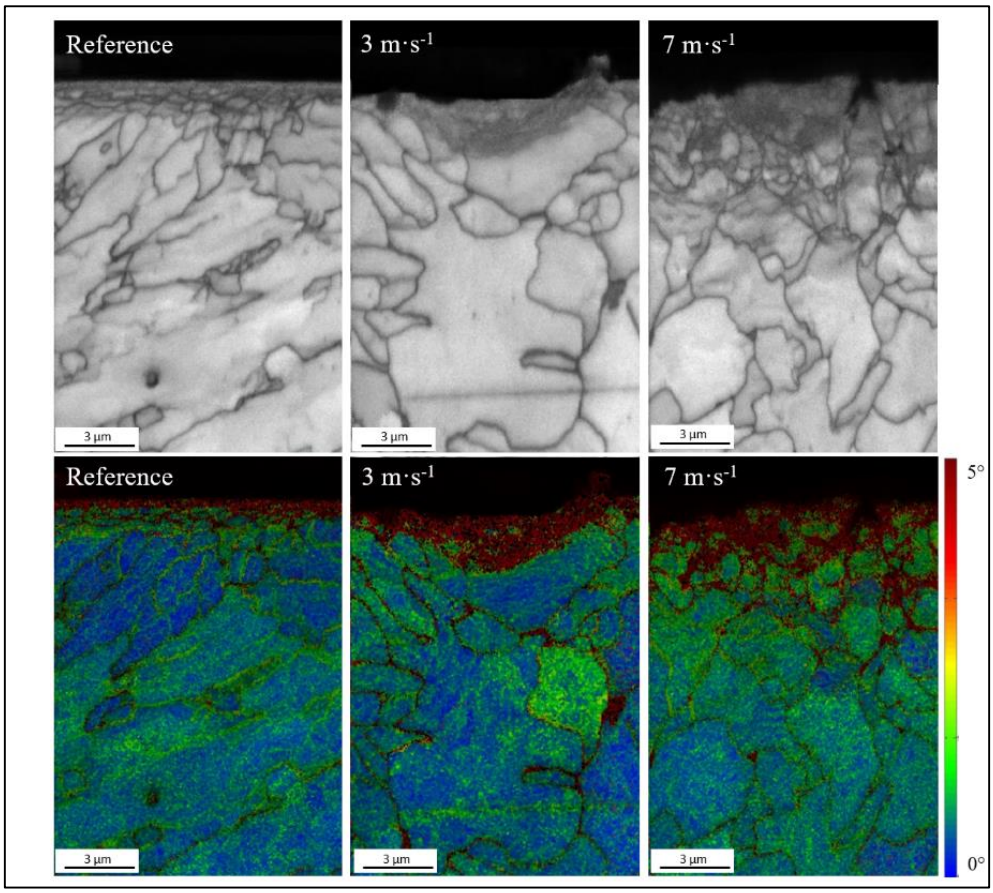

Figure 5.13 EBSD analysis of the sub-surface microstructure at different velocities of slurry flow: Image quality (top row); KAM analysis (bottom row).

Local misorientation analysis by the KAM method shown in Figure 5.13, allows assessing the qualitative magnitude of plastic deformation in the sub-surface of the samples. The blue and red areas in the KAM analysis indicate the extreme values of local misorientation, where 0° and 5° means non-deformed and highly deformed grain, respectively. The effect of flow velocity can be quantified by the depth of the deformed layer, which extends to 2.1 µm and 4.5 µm for the velocities of 3 and 7 $m \cdot s^{-1}$, respectively.

5.2.2.2 Effect of dissolved oxygen

The effect of the slurry DO content on the sub-surface damage is shown in Figure 5.14. The image quality reveals a significant difference in the appearance of microstructures after exposure to the slurry in the absence (0 ppm) and the presence of DO (10 ppm). In the absence of oxygen, the microstructure is analogous to that described in Figure 5.13, with layers of distinctive grain size in the sub-surface, extending down to 1.8 μm below the nominal surface of the smallest nanograins, followed by the transition layer consisting of grain in the micrometer length scale extending further 3.7 μm and finally the grains characteristic of the bulk material. On the other hand, the sub-surface of samples exposed to 10 ppm of DO does not show an apparent change in the grain size immediately under the worn surface. There is also no deformation observed in sections of the craters. However, incomplete grains are observed at the sides and bottom of the crater.

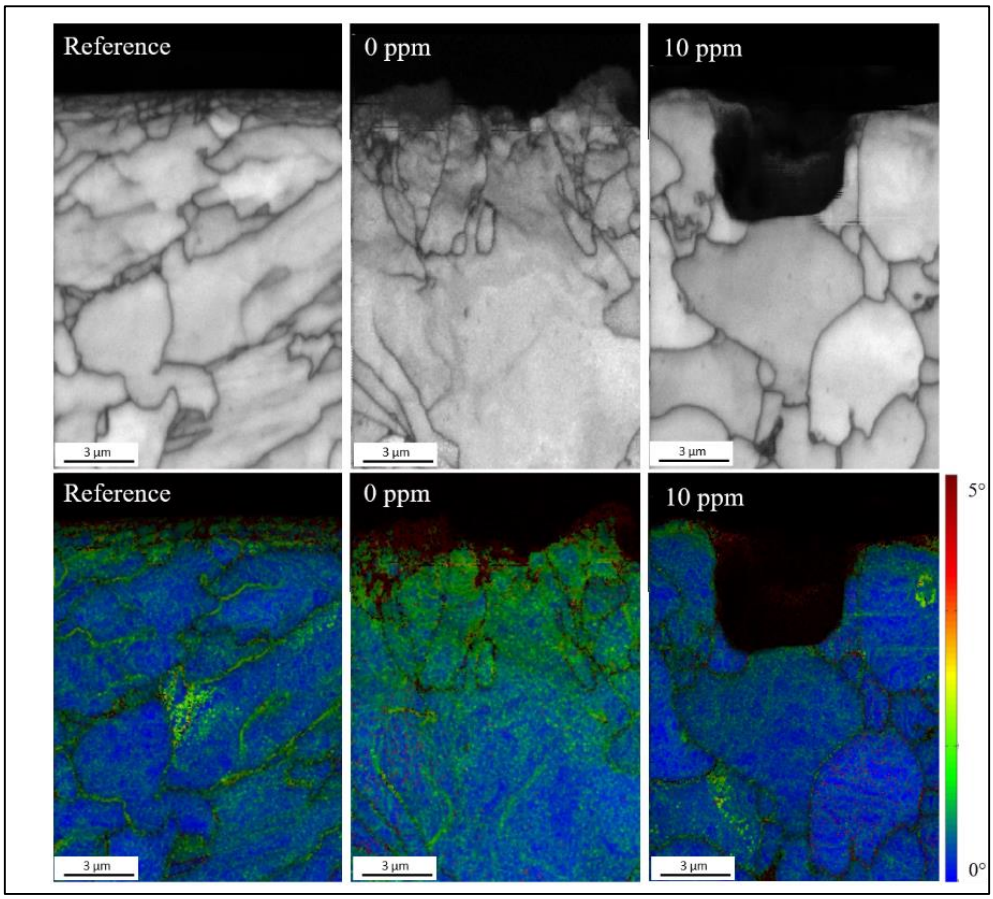

Figure 5.14 EBSD analysis of the sub-surface microstructure at different levels of oxygen. Image quality (top row); KAM analysis (bottom row).

KAM images reveal strong plastic deformation for samples exposed to 0 ppm DO, analogous to that observed in Figure 5.13. Whereas, exposure to oxygen-rich slurry results in slight plastic deformation of the top surface and no plastic deformation within the dimples. In particular, the grains comprising the pit show no plastic deformation around its perimeter, which is consistent with the incomplete grains described previously.

5.2.2.3 Effect of temperature

The microstructure of the sub-surface at different temperatures (Figure 5.15) shows a shallow layer of grains reduced in size near the surface for both 25 and 45 °C. While the KAM analysis shows a similar deformation layer of depth about 1 µm.

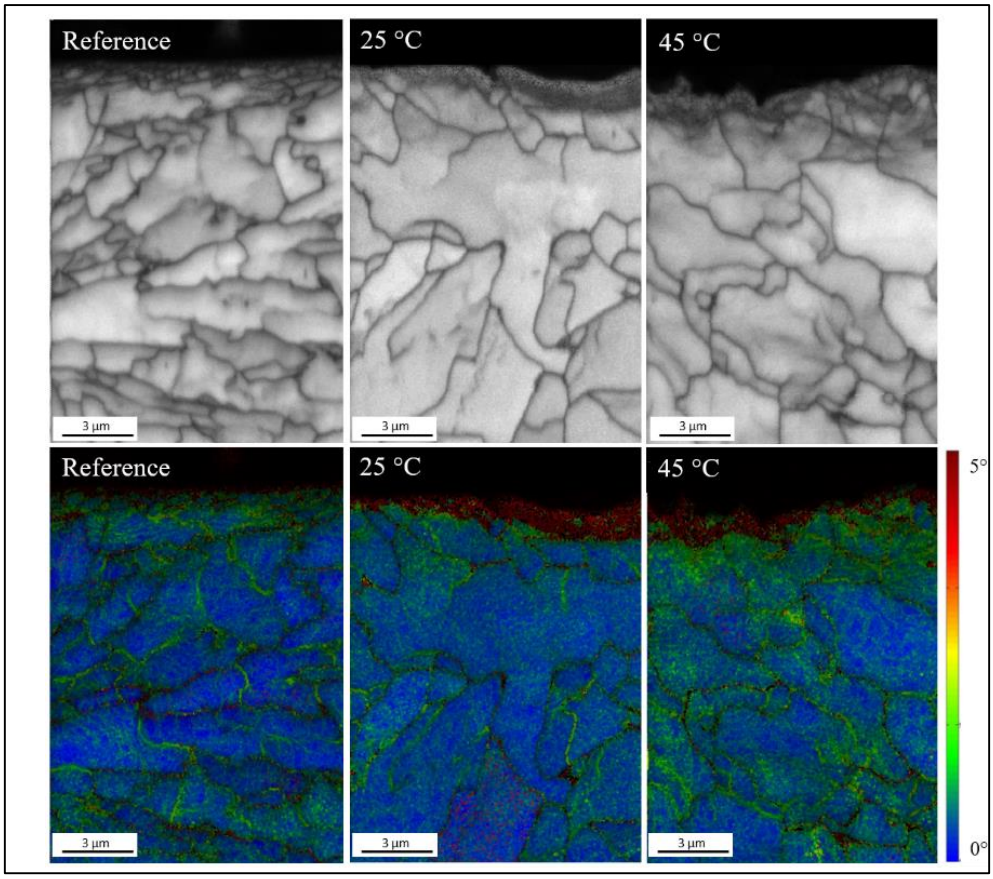

Figure 5.15 EBSD analysis of the sub-surface microstructure at different temperatures. Image quality (top row); KAM analysis (bottom row).

5.2.2.4 Effect of particles

The microstructure of the sub-surface (Figure 5.16) presents an evident change by varying the concentration of particles in the slurry. The images quality shows a reduction in the grain size of different expanse in depth similar to the one described in Section 5.2.2.1 for 7 $m \cdot s^{-1}$. In general, the sample exposed to 45 wt% of particles has a total layer of smaller grains (nano- and micro-grains) of 1.6 depth, while in samples exposed to 65 wt% the reduction in grain size reaches 3.8 um in depth. Local misorientation analysis by the KAM method shows the depth of the deformed layer, which extends to 1.9 µm and 4.4 µm for the concentration of 45 wt% and 65 wt%, respectively.

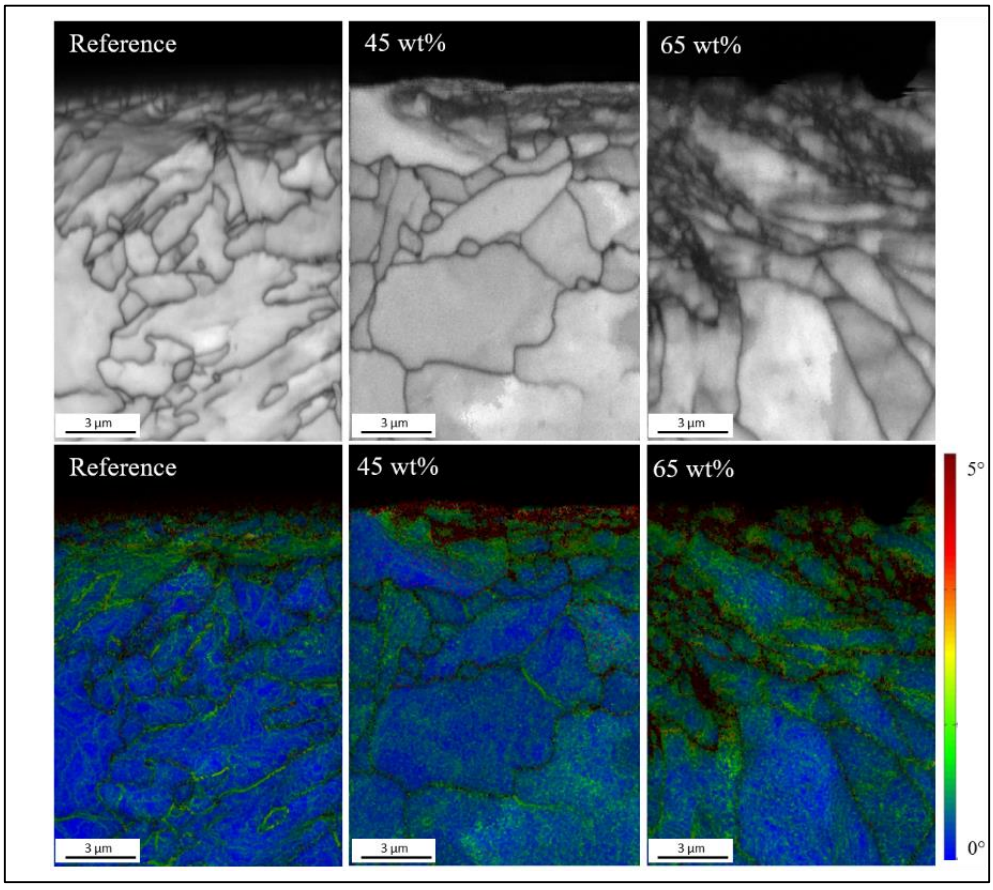

Figure 5.16 EBSD analysis of the sub-surface microstructure at different particles concentration. Image quality (top row); KAM analysis (bottom row).

5.2.2.5 Effect of copper ions

The microstructure of the sub-surface for samples at the different concentration of copper ions and 10 ppm of DO in the slurry is shown in the area of the dimples (Figure 5.17). The images do not show an evident reduction in the grain size at the top of the dimples, while inside these, incomplete grains are seen again similar to those observed in presence of DO (Figure 5.14). For both samples, the KAM analysis shows a small deformed layer on the surface above the dimples, while inside these there is no evident plastic deformation.

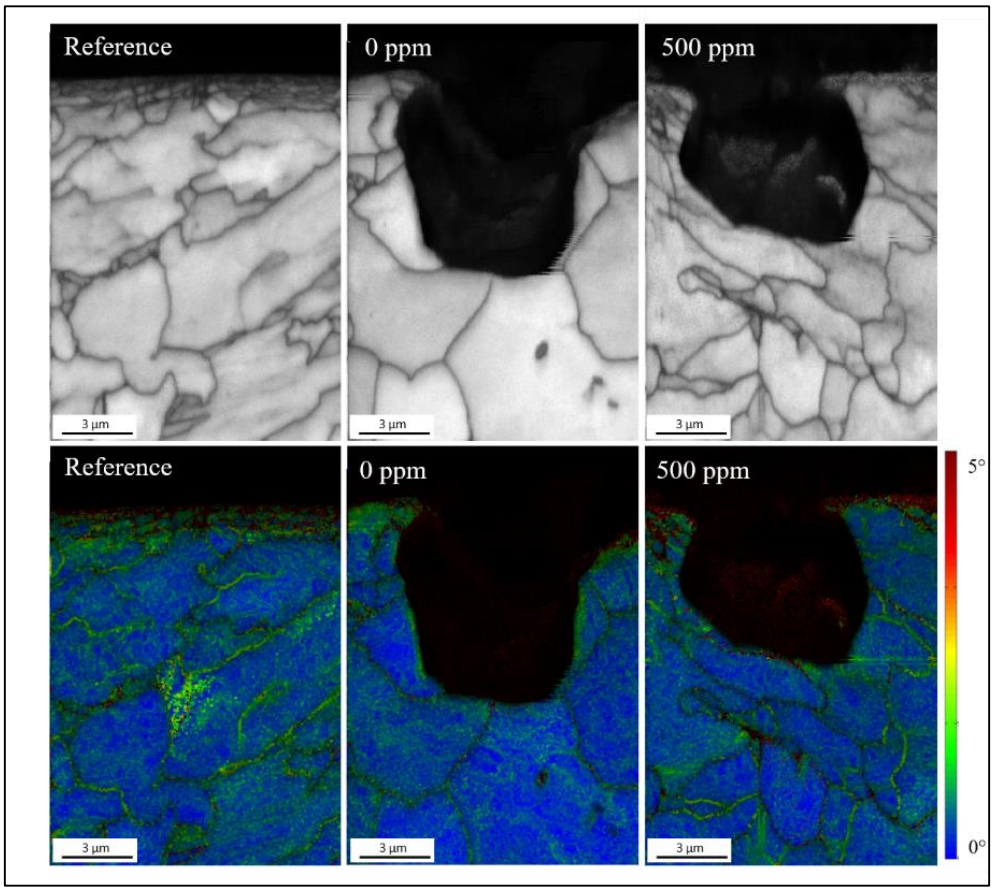

Figure 5.17 EBSD analysis of the sub-surface microstructure at different Cu^{2+} concentrations. Image quality (top row); KAM analysis (bottom row).

5.2.3 Potentiodynamic polarization

The potentiodynamic polarization curves collected for analyzing the electrochemical behavior of the factors are shown in Figure 5.18.

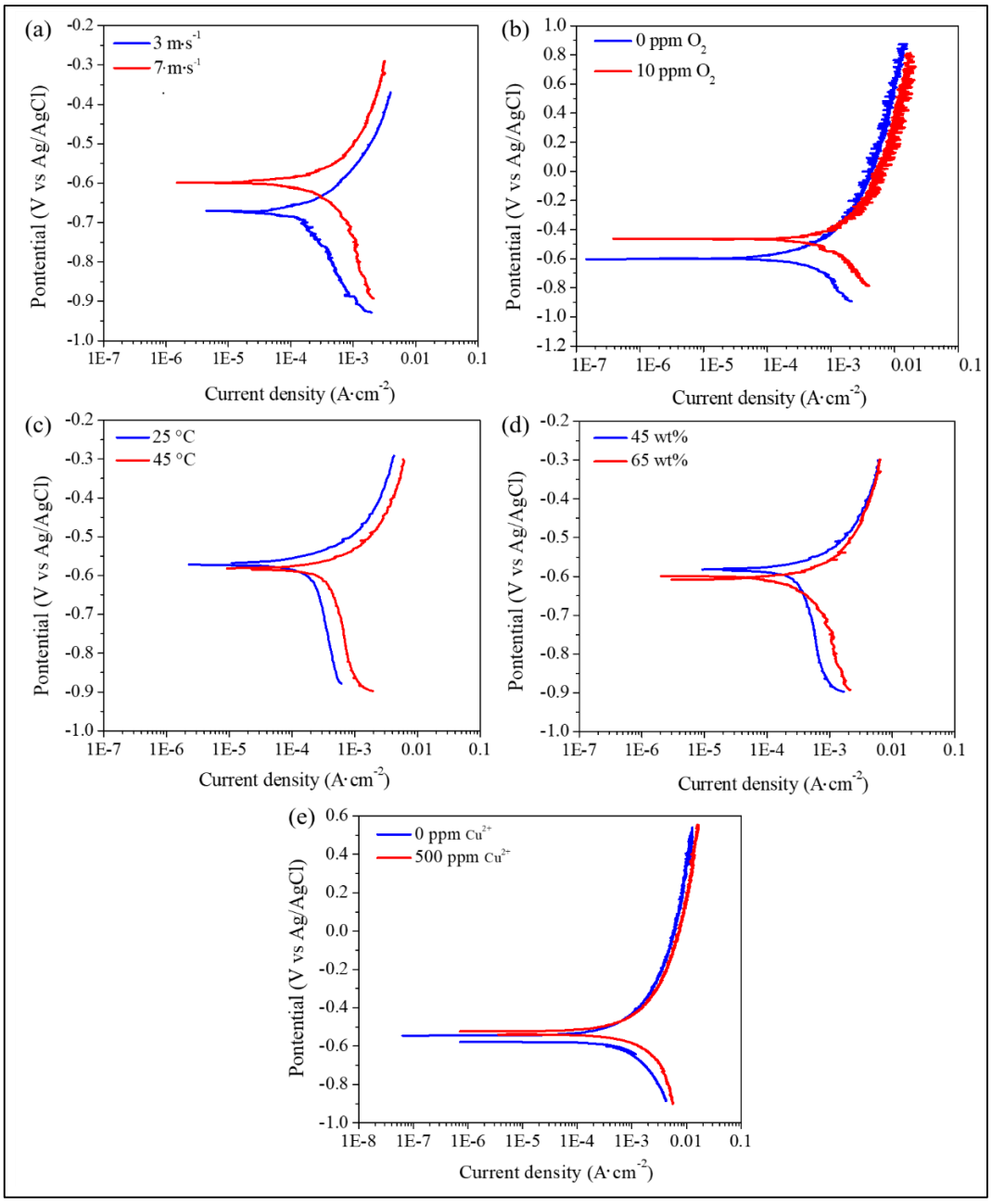

Figure 5.18. Potentiodynamic polarization during E-C exposure under varying (a) slurry flow velocity, (b) content of DO (c) temperature, (d) particles concentration and (e) copper ions content in the slurry.

The electrochemical parameters derived from the polarization curves are presented in Table 5.2.

Table 5.2 Electrochemical parameters from potentiodynamic polarization.

Factor	Sample	E_{corr} (V)	i_{corr} ($A \cdot cm^{-2}$)	Corrosion rate ($mm \cdot yr^{-1}$)
Velocity	3 m s^{-1}	- 0.675	8.27×10^{-5}	0.97
	7 m s^{-1}	- 0.599	1.76×10^{-4}	2.06
Dissolved Oxygen	0 ppm	- 0.603	1.69×10^{-4}	1.97
	10 ppm	- 0.466	3.21×10^{-4}	3.75
Temperature	25 °C	-0.569	6.95×10^{-5}	0.81
	45 °C	-0.582	1.32×10^{-4}	1.53
Particles concentration	45 wt%	-0.583	1.07×10^{-4}	1.25
	65 wt%	-0.605	1.68×10^{-4}	1.96
Copper ions content	0 ppm	-0.558	1.56×10^{-4}	1.82
	500 ppm	-0.531	2.54×10^{-4}	2.97

The flow condition of the electrolyte in the absence of oxygen (Figure 5.18a) affects both the anodic and cathodic polarization currents, observing a greater increase in the latter at a higher velocity, producing a corrosion current density (i_{corr}) at least twice greater.

The increase of DO in the slurry (Figure 5.18b) shows a shift in the corrosion potential (E_{corr}) of almost 0.2 V towards the anodic direction, associated with the increase in the current density of the cathodic branch; this also increases almost twice the i_{corr} of the system (Table 5.2). The anodic current density presents a slight increase at higher DO content, without significant changes in its behavior between the treatments.

The change in the temperature of the slurry (Figure 5.18c) shows an increment in the intensity of both anodic and cathodic curves of the system, which produces an increase in the corrosion current density by a factor of 1.8 times when the temperature of slurry rises from 25 °C to 45 °C.

The increase in particles content (Figure 5.18d) shows a slight increase in the intensity of both anodic and cathodic curves, increasing the corrosion current density by only 0.6 times when the concentration of particles changes from 45 wt% to 65wt% in the slurry.

The presence of 500 ppm of Cu^{2+} at 10 ppm of DO (Figure 5.18e) does not modify the behavior of the anodic and cathodic branch in the system. However, the intensity of the cathodic current density increases, which results in 1.5 times higher corrosion current density (Table 5.2).

6 DISCUSSION

The statistical analysis of the effects of slurry velocity, particle concentration, temperature, pH, dissolved oxygen concentration, and copper ion content of slurry, and their corresponding interactions, on the wear of a X65 steel by a slurry of copper tailing revealed that there are only five significant effects on the E-C rate, which explains 85.25% (R^2–adjusted) of the variation observed in the wear rates. These are, in decreasing order of magnitude (Figure 5.3), the effects of velocity, dissolved oxygen, the interaction between particle concentration and copper ion content, temperature, and finally the interaction between dissolved oxygen and slurry velocity. The effect of all other factors, because they are not statistically significant, can be considered to lie within the experimental variability of the employed method. Notably, the relevance of P×Cu^{2+} and V×DO interactions, have produced a greater contribution to the degradation process than some of the individual factors alone. In the case of P×Cu^{2+}, the interaction effect exceeds the contribution of its constituent factors, i.e., P and Cu^{2+} alone. A possible mechanistic explanation of these observations is discussed further in this section, addressing first the main effects, followed by discussing the interactions.

6.1 Effect of slurry velocity on E-C mechanisms

Out of the five significant effects identified in the present study, the increase in slurry velocity represents the greatest contribution to the E-C rate (Figure 5.1 and Figure 5.3). This effect, as discussed by the other authors, is mainly associated with the kinetic energy conveyed by the erodent since only particles with sufficient energy are capable of inducing surface deformation and producing removal of the material. Since the faster flow of slurry implies more kinetic energy of the solid phase, the results of the E-C rate observe here (Figure 5.1) would be qualitatively explained. However, since the process progresses in time, other side effects associated with the change in particle velocity should be taken into consideration, such as turbulence of the flow, the frequency of particles' impact,

change in effective impact angle, evolution of surface roughness in time and contribution of mass loss due to anodic dissolution.

The morphology of top- and sub-surfaces observed after exposure (Figure 5.6 through Figure 5.12) corresponds to the state of damage accumulated during the entire time of exposure consisting of successive impacts of particles hitting the steel and degradation by electrochemical corrosion process. The particle velocity vector of each particle, as introduced by Finnie and Bitter (Bitter, 1963a, 1963b; Finnie, 1960), can be described as a sum of two components, a horizontal one, associated with the plowing mechanism of surface removal, and a vertical one, associated with penetration/indentation and accumulation of fatigue damage. Even though in the RCE set-up it is not possible to control the angle of impact (θ) of each particle, i.e., the angle between velocity vector of a particle and the target surface, scar morphologies characteristic of low impact angles ($\theta < 45$ °) and high impact angles ($\theta > 45$ °) could be identified at both velocities (Figure 5.6). Thus, it is possible to distinguish a difference between the dominant erosion mechanisms at both slurry velocities.

The scars produced on the surface at 3 $m \cdot s^{-1}$ (Figure 5.6) appear less deep and more elongated as compared with the faster flow, indicating a greater magnitude of the horizontal component of velocity. As an abrasive particle slides on the surface after being projected at a low angle of impact, the preferential material's removal is expected to be plowing or cutting. As the particles slide on the surface, they squeeze the metal forward and sideways to form ridges. Subsequent impacts of particles flatten the ridges, generating metal debris by fracturing them off (Hutchings, 1992; Islam & Farhat, 2014).

In the case of the faster flow (Figure 5.6) the impact velocity and frequency of particle both increase, while the distribution of particles' impact angles is modified by the slurry turbulence (Molina, Aguirre, & Walczak, 2019). In particular, characteristic craters of high impact particles are observed, shifting the mechanism of material's removal towards indentation at normal incidence and micro-machining. However, the first mechanisms of metal removal seem to dominate under high particle velocity conditions

as indicated by the morphology of the crater. In this case, the indentation crater displaces the deformed material, forming an edge around the crater due to the impact of the particle. The material can be eliminated by deformation or fracture of these edges by the subsequent impact of particles as described for the normal impacts of angular particles (Islam & Farhat, 2014; Winter & Hutchings, 1974).

The preferential mechanism of material's removal is thus different at the two velocities providing a qualitative explanation for the difference in the E-C rate (Figure 5.1). In terms of flow parameters, this difference can be understood as the total of effects associated with the frequency of impacts, average kinetic energy conveyed per particle and impact angle. Considering that in case of ferritic steels, for a given nominal velocity of flow, the rate of target's removal for low impact angles ($\theta < 45°$) is higher than that of impact angles ($\theta > 45°$) (Islam & Farhat, 2014); it follows that the increase in particle energy and frequency of impacts are the main cause of E−C rate associated with nominal flow velocity.

The extension of plastic deformation in the sub-surface is observed in the EBSD analysis, visualizing differences produced at the two velocities of exposure. Samples worn at 3 $m \cdot s^{-1}$ (Figure 5.13) show marks of plastic deformation in a reduced section of the sub-surface, all of which have been produced by the impact of particles conveying sufficient kinetic energy and impacting at the proper orientation to deform the material. Whereas, samples worn at 7 $m \cdot s^{-1}$ (Figure 5.13) the damage induced by plastic deformation appear to accumulate in the sub-surface, which can be explained by the simultaneous increase of particle's kinetic energy, the frequency of impact and the impact angle of the particles. All the three aspects of particle's impact translate into a higher absorption of energy towards the material's bulk. As the top layer of the surface layer undergoes work-hardening, the load is progressively transmitted to the bulk grains. This load is initially transformed into work resulting in the formation of micro-grains, and after sufficient dislocations have accumulated, the deformation of the bulk grains would proceed. Formation of these layered structures of sub-surface by grain refinement was previously

described by. Umemoto (2003) and Rajahram et al. (Rajahram, Harvey, Walker, Wang, & Wood, 2012), associated with processes of severe plastic deformation. This explanation is consistent with observing sharp and irregular craters that at the high velocity (Figure 5.6), which can be attributed to strain hardening of the surface layer and thus reduced the ability of the target material to deform at impact, favoring fracture over deformation.

In addition to the erosive mechanisms of materials removal through mechanical damage described above, the contribution of the slurry velocity through electrochemical corrosion should be considered. This additional mechanism is evidenced by higher corrosion current density at the higher slurry velocity (Figure 5.18), which results in an increment in the corrosion rate of the material (Table 5.2). In this case, although the nominal DO is 0 ppm, its effective value varies between 0 and 0.3 ppm, allowing to expect the main electrochemical reactions at the measured overpotentials to be oxidation of steel ($Fe \leftrightarrow Fe^{2+} + 2\bar{e}$) and the reduction of oxygen in the slurry ($O_2 + 4\ H^+ + 4\bar{e} \leftrightarrow 2\ H_2O$). Thus, on the one hand, higher velocity implies faster transport of electroactive species towards and from the electrolyte (Tian & Cheng, 2008), shifting the reactions towards activation control. On the other hand, the increment in corrosion current can be explained by a greater surface roughness produced at the higher velocity providing a larger area of fresh material and the possible preferential activation of the strain-hardened zones (Ghosh et al., 2017; Kingkam, Zhao, Li, Zhang, & Li, 2018). Both explanations are plausible as indicated by the increase in cathodic and anodic currents by a similar amount at given over potential in Figure 5.18.

Finally, the effect of velocity can be summarized by the conceptual model shown in Figure 6.1.

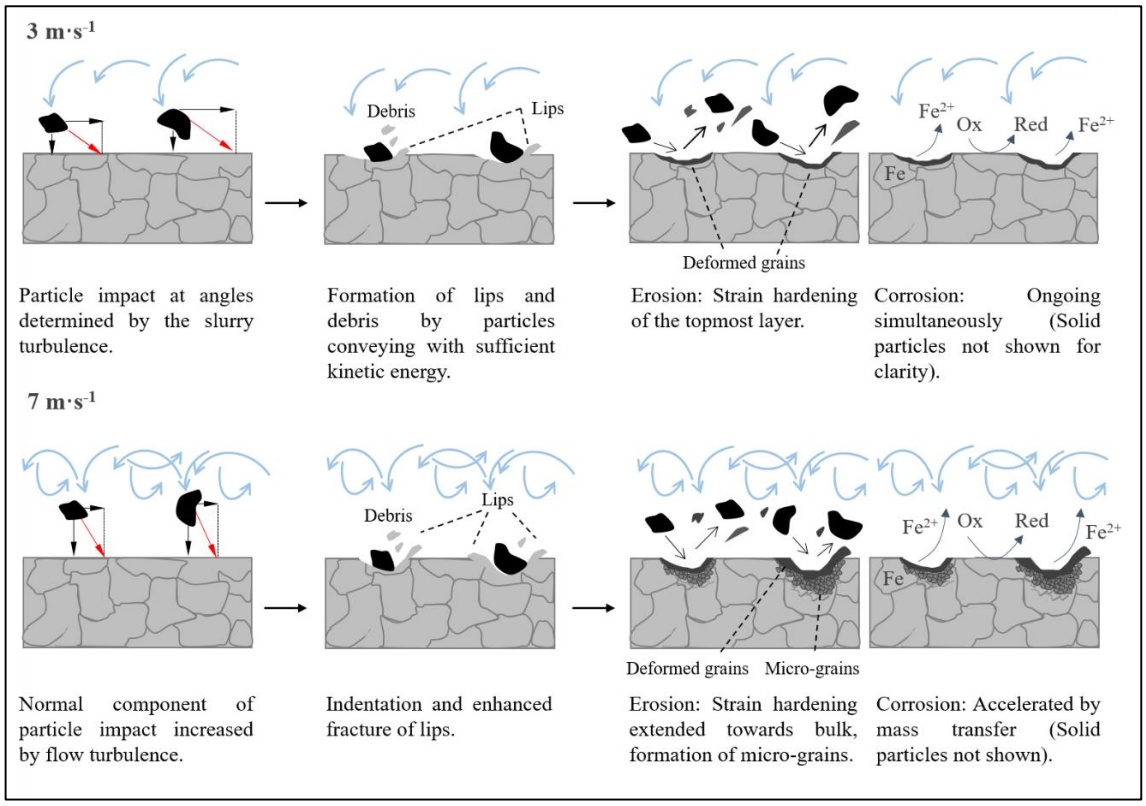

Figure 6.1 Schematic representation of the effect slurry velocity on the mechanism of E-C at very low concentration of oxygen (nominal DO 0 ppm).

6.2 Effect of dissolved oxygen on E-C mechanisms

The presence of oxygen in the slurry promotes electrochemical corrosion of the material, increasing the E-C rate (Figure 5.1), which might be explained by localized-corrosion as suggested by the visual appearance of the resulting surface (Figure 5.7). Localized corrosion in the presence of oxygen has been reported for active metals associated with the breakdown of stable corrosion product film of Fe_2CO_3 generated in slurries containing dissolved CO_2 (Hua, Barker, & Neville, 2015; Motte, Barker, Burkle, Vargas, & Neville, 2018), however, this is not the case here. In this study, both physical and chemical modification of surface are observed in association with the presence of oxygen. Figure 5.7 and Figure 5.8 show two clearly distinctive areas at the top surface: i)

dimples, several times larger than the indents observed after exposure without oxygen, characterized by predominantly high concentrations of oxides and embedded particles; and ii) remaining top surface of scar morphology equivalent to that described previously but with sparsely distributed fine erodent particles present in addition. Because the grains present inside the dimples consist of incomplete grains, they are interpreted as caused by electrochemical dissolution and are thus associated with anodic areas. The remaining surface is then interpreted to be cathodic, giving rise to a localized type of corrosion through the galvanic coupling of the macroscopic anodic and cathodic areas. In addition to these macroscopic features indicative of galvanic coupling, another couple can be identified at the microscopic level, i.e., between eroded and uneroded top surface which is clearly less affected by the corrosion process.

The increase of corrosion rate in the presence of oxygen (Table 5.2) is explained by the same electrochemical reactions of oxidation ($Fe \leftrightarrow Fe^{2+} + 2\bar{e}$) and reduction ($O_2 + 4\ H^+ + 4\bar{e} \leftrightarrow 2\ H_2O$), however, considering higher concentration of oxygen. The polarization curves recorded in exposure to the flowing slurry (Figure 5.18) show increased cathodic current density in the presence of oxygen, while anodic current density is not greatly affected. Thus, the reaction system can be considered under cathodic control through availability of oxygen at the electrode's surface. The relationship between the current density in terms of diffusional limiting current for a RCE system (J_{LRCE}) can be estimated by the Levich relation (Walsh et al., 2017), which adapted for the geometry used in this study is given by (Equation 6.1:

$$J_{LRCE} = 0.069\ z\ F\ c_b\ \nu^{-0.344}\ D^{0.644}\ U^{0.7} \qquad \text{(Equation 6.1)}$$

where c_b is the bulk concentration of electroactive species, D - diffusion coefficient of the species, z - charge number, F - Faraday constant, ν - kinematic viscosity of the electrolyte, and U - peripheral velocity of the RCE. Then, at a constant velocity, greater availability of DO in the slurry increases the diffusional limiting current resulting in a faster material degradation by the electrochemical action. On the other hand, the shape of the anodic branch is not modified significantly by a greater DO content in the slurry, which suggests

that the localized type of surface damage is related to the erosive effect rather than electrochemical degradation associated with the possible breakdown of a film of corrosion products on the surface. This idea is discussed in detail in Section 6.2.1.

Generation of the macroscopic anodic and cathodic areas seem to involve mechanisms different from the microscopic anodic and cathodic areas associated with particle impacts, which were deduced in the absence of oxygen. Although the impact of erosive particles generates a work-hardened layer, rendering the top surface more susceptible to brittle fracture by the subsequent impingement of particles, in the abundant presence of oxygen no plastic deformation is observed at the anodic sub-surface. The incomplete grains at the bottom of the dimple in Figure 5.14 (10 ppm DO) suggest that the electrochemical dissolution of grains is the case rather than extraction of entire grains as suggested by Neville et al. (1999). On the other hand, the sub-surface of the cathodic zones might be expected to be equivalent to that observed at 0 ppm DO for the same conditions of erosion in terms of particles' content, shape, size, and momentum, resulting in the formation of layers of plastic deformation of decreasing grain size towards the bulk. However, the extent of plastic deformation in these cathodic areas is greatly reduced, suggesting that corrosion accelerated by the presence of oxygen prevents the formation of a work-hardened layer on the surface. Such a mechanism could be attributed to electrochemically induced modification in steel's hardness, facilitating the removal of the material as reported by Lu and co-workers (Guo et al., 2005; Lu & Luo, 2015). In this case, the kinetic energy of the particles is conveyed directly into material's removal, rather than accumulating it as plastic deformation in the sub-surface.

6.2.1 Localized corrosion in the presence of oxygen

In order to elaborate on the nature of the localized corrosion it is interesting to note, that at the same conditions without the presence of erodent, i.e., only corrosion process, the main observable damage is by uniform corrosion on the surface as shown Figure 6.2. Thus, localized corrosion at higher DO content in the slurry only occurs in the

presence of particles, demonstrating the synergistic effect between erosion and corrosion. The synergy is deduced to be dominated by erosion−enhanced corrosion mechanism.

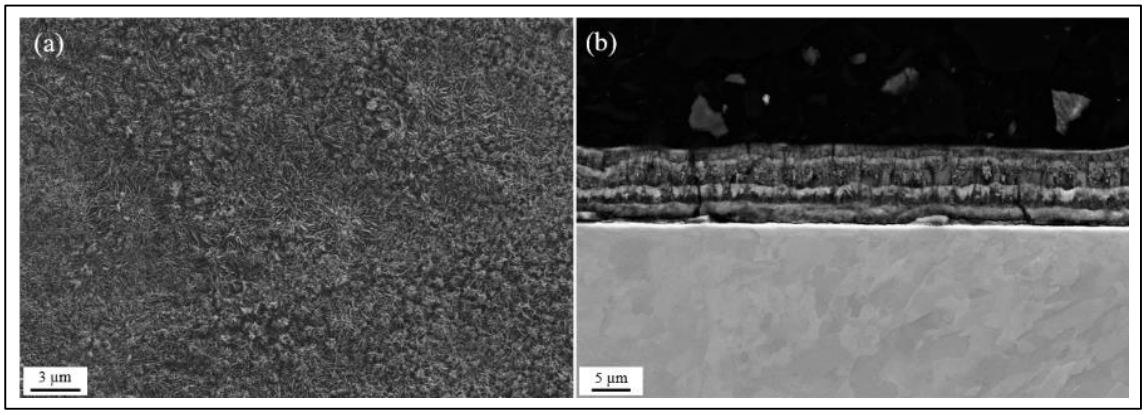

Figure 6.2 Sample exposed to pure erosion in absence of particles. (a) Surface and (b) Cross-section of the sample. Condition of the test: V = 7 m/s, T = 45 °C, pH 5, DO = 0 ppm, and Cu^{2+} = 0 ppm.

Previous studies (Xie et al., 2003a, 2003b) have shown that plastically deformed areas are more anodic and therefore are more susceptible to corrosion than non-deformed areas. Such an anodic activation could be expected considering the change of the surface energy of the exposed area associated with strain-hardening. In this work, considering a highly corrosive environment, it is suggested in the initial stages of damage by erosion-corrosion, areas plastically deformed at random by the impact of particles in the steel would create areas of localized charge on the surface, originating the dissolution of these zones preferably. Thus, areas initially deformed plastically would be used as incubation zones for the growth of the dimples during the process. A schematic representation is presented in Figure 6.3 It is not clear if this behavior remains active during the entire period of exposure of the material. Further investigation should be done to clarify this behavior.

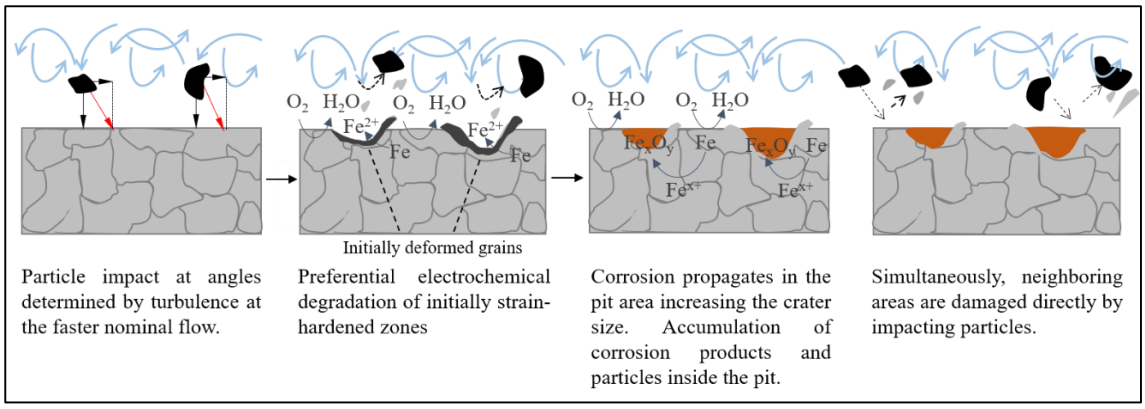

Figure 6.3 Schematic representation of the effect of dissolved oxygen on the mechanism of E-C.

6.3 Effect of temperature on E-C mechanisms

The last significant main effect, the temperature, has a low contribution to the overall material degradation (Figure 5.1 and Figure 5.3). It is normally expected that an increase in temperature increases the rates of both erosion and corrosion. The mechanisms involved in the case of erosion include temperature-related modification of physical properties of the slurry that are relevant to flow properties, notably its viscosity (Levy & Hickey, 1987; Stack et al., 2010), and to a lesser degree, modification of the mechanical properties of the metallic target. Whereas the first mechanism contributes to an increase in the erosion rate, the latter may go both ways, depending on the temperature range and the relative contribution of corrosion, which in turn, depends on temperature on its own. On the other hand, the current density is a function of Tafel coefficients determined by the kinetics of the involved reaction and which, in turn, depend on temperature through the Arrhenius relation. According to these relations, the rate of corrosion can be expected to double with every 10 °C increase in temperature approximately.

In the present work, no significant difference in surface morphology and sub-surface characteristics was observed when testing at different temperatures in the absence of oxygen (Figure 5.9 and Figure 5.15). However, it was observed from the potentiodynamic curves (Figure 5.18) an increase of 1.8 times in the corrosion rate of steel (Table 5.2) by varying the temperature of the slurry from 25 to 45 °C at the same exposure

conditions. This latter suggests that the contribution of corrosion and its cross-effects through synergy would tend to dominate the mechanism of wear with an increase in temperature, rather than the mechanical erosion process. This observation is consistent with data from the literature for similar test conditions (Hu & Neville, 2005).

6.4 Interaction between slurry velocity and dissolved oxygen

The interaction between velocity and dissolved oxygen (Figure 5.4) shows a greater E-C degradation than the interaction between particles concentration and copper ion content (Figure 5.5), reaching E-C rates higher than 6 $mg \cdot cm^{-2} \cdot h^{-1}$ when both factors are of the highest level. This interaction is interpreted as a synergistic effect between the two constituent factors, where slurry velocity has a dominant component on the E−C rate according to the contour map of Figure 5.4.

As was described previously in Sections 6.1 and 6.2, the increase in slurry velocity leads to surface plastic deformation and removal of the material target by the erosion of the particles, besides facilitating the mass transfer of the reactant and products from and to the material, increasing the electrochemical activity of the steel. Whereas the presence of oxygen accelerates the corrosion process generating, in the presence of particles, localized-type corrosion that produces a significant loss of material, at the same time the strong electrochemical action degrades surface properties that enhance the steel removal.

Thus, the simultaneous increment in the slurry velocity and DO enhance the intensity of these effects. Since, the effect of slurry velocity increases the plastic deformation of the material, which could promote, in the first stages of erosion, the potential difference in the surface between anodic and cathodic sites, favoring the anodic dissolution in the plastically deformed areas to intensify the localized-corrosion observed (Figure 5.7). At the same time, the higher DO and also slurry velocity accelerates mass-transfer of oxygen and corrosion products, increasing the rate of corrosion and consequently the removal of mass from the target.

6.5 Interaction between particles concentration and copper ion content

The interaction between particle concentration and content of copper ions has a negative coefficient in (Equation 5.3, corresponding to a cross-effect between the factors. However, in order to understand this interaction, it is worthwhile to describe the individual effects of both factors separately.

6.5.1 Effect of particle concentration on E-C mechanisms

On the one hand, the effect of particle concentration at the same exposure conditions is directly related to the frequency of impact on the steel since there are more particles available to hit the surface (Dasgupta et al., 1998; Kleis & Kulu, 2008; Turenne et al., 1989). Because particles convey kinetic energy, each effective impact leads to energy accumulation in the form of plastic deformation of the material (Figure 5.16). The subsequent impact of particles leads to the generation of a work-hardened layer into the sub-surface, favoring erosion by fracture or fatigue as described in the context of slurry velocity (Section 6.1). Consequently, a greater concentration of particles intensifies this process.

On the other hand, a greater concentration of particles slightly increases the corrosion density current (Table 5.2). This increase can be explained by a faster rate of exposing fresh material, i.e., active metal, for electrochemical corrosion since a greater amount of impacts activates the surface of the metal, exposing fresh material for electrochemical corrosion.

It also is observed that the change in particles concentration from 45 wt% to 65 wt% produces only a slight increase in the E−C rate (Figure 5.1), rendering this factor not significant on its own. This result is consistent with previous studies (Turenne et al., 1989) that indicate a decrease in the effective erosion rate at a high concentration of solid volume (more than 15 wt%), which can be explained by particle-particle interaction due to rebounding or screening effect, that reduces the effective particle energy transferred into the material.

6.5.2 Effect of copper ions on E-C mechanisms

No significant difference in surface morphology and sub-surface characteristics was observed when testing at higher copper ion concentration in the presence of oxygen (Figures 5.11 and 5.17). This observation suggests that the increment in E-C rate by free copper ions in the slurry (Figure 5.1) is mainly related to the process of electrochemical corrosion of the steel.

The limiting current observed in the cathodic branch in copper-free electrolyte (Figure 5.18e) is characteristic for oxygen diffusion and reduction on X65 steel surface as shown by several authors (Sherif, Almajid, Khalil, Junaedi, & Latief, 2013; Tian & Cheng, 2008; Vera, Vinciguerra, & Bagnara, 2015; Zhang & Cheng, 2009). As copper ions are added, the increase in cathodic current can be explained by additional reaction of Cu^{2+} reduction ($Cu^{2+} + 2\bar{e} \rightarrow Cu^{0}$) consuming additional electrons and thus increasing the corrosion density current as observed in Table 5.2. This behavior has been reported for similar concentrations of copper ions (Aguirre & Walczak, 2017). Figure 6.4 shows the effect of different concentration of copper ions on the intensity of the cathodic branch (marked by arrow).

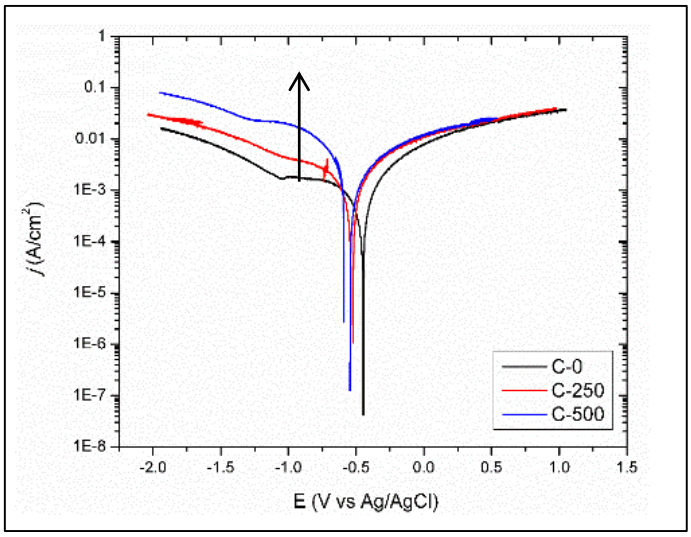

Figure 6.4 Polarization curve recorded during exposure to erodent-free electrolyte of varying Cu^{2+} concentration. Adapted from Aguirre & Walczak (2017).

The reaction of Cu^{2+} reduction produces deposition of metallic copper at the steel's surface as evidenced by the presence of copper in the EDX data of the cross-section (Figure 5.12b). The latter supports the description of anodic (dimples) and cathodic (base metal) sites described in Section 6.2 since copper deposits are preferably observed on the top surface of the metal where the reduction would occur, rather than in the area of dimples. This situation is shown schematically in Figure 6.5.

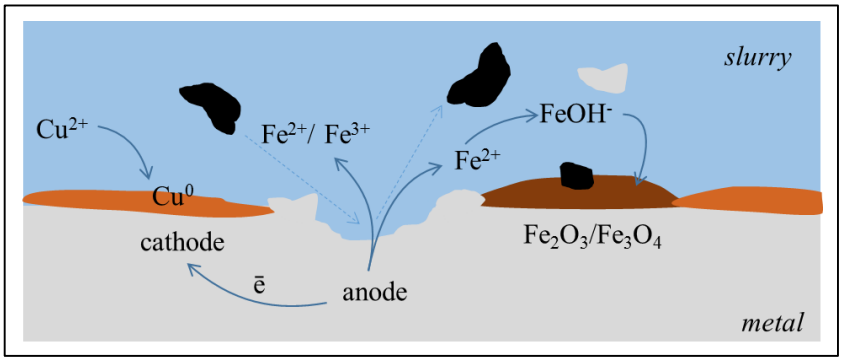

Figure 6.5 Schematic representation of the effect of copper ions in the system (Aguirre & Walczak, 2017).

6.5.3 Interaction

The individual effect of the two factors is shown in the contour map (Figure 5.5), on the respective coordinate axis. In the absence of Cu^{2+} (0 ppm) a higher concentration of particles leads to an increase in the E-C rate. Analogously, this occurs for the increment of Cu^{2+} at 45 wt% of particles. However, their interaction presents an antagonistic effect decreasing the erosion-corrosion rate when both factors are at their highest level. The observed cross-effect is attributed mainly to the effect of copper ions in the slurry, which increases the E-C rate by the mechanism described in the previous section (Section 6.5.2). The latter can be explained by the different amount of copper ions available in the slurry by volume, as the concentration of particles is modified. Thus, a lower particle concentration would be associated with a higher effective amount of Cu^{2+}, despite its nominal concentration being constant. The inverse is observed for higher particle concentrations. The stabilization of the E-C rate at the central levels of P and Cu^{2+}

observed in Figure 5.5 supports this explanation. Therefore, the intensity of the effect on E-C rate, i.e., the cross-effect, depends on the amount of Cu^{2+} in the liquid phase relative to particle concentration.

7 CONCLUSIONS

The erosion-corrosion wear of API 5L X65 carbon steel by simulated copper tailing slurry has been examined by a statistical analysis of the parameters identified as relevant in the operational practice of a mining slurry pipeline. The statistical analysis used for identifying the significant parameters and interactions allowed the formulation of a phenomenological description of the E-C in the studied system to be stated. Although the description is valid only for the studied range of factors, it has provided key information on the parameters that contribute most to the steel damage.

The significant main effects and interactions were determined, which are in order of decreasing the effect on the E-C rate were: slurry velocity, dissolved oxygen, the interaction between particle concentration and concentration of copper ions, temperature, and the interaction between velocity and dissolved oxygen. All the main factors as well as the interaction between velocity and dissolved oxygen, increase the erosion-corrosion rate of the steel when it increases their intensity. However, the interaction between particle concentration and copper ions presents an opposite behavior, decreasing the corrosion-erosion rate when both factors increase. As a result of their contributions, these three main effects and two interactions explain 85.25% of the variation in wear rate observed.

These statistical results allowed focusing the analysis of the wear mechanisms on the effect of main factors and interactions. The surface and sub-surface inspection, as well as the electrochemical measurement of X65 steel exposure to copper tailing at different E-C conditions, allow formulating the following insights into the mechanisms of erosion-corrosion:

1. The erosive effect of slurry velocity is associated with grain refinement and localized accumulation of plastic deformation in the sub-surface. The increment of flow velocity increases the frequency of impacts and the energy conveyed per particle through the normal component of the effective impact velocity, both of which are the main contributors to removing the material. In addition, a synergetic contribution of velocity through corrosion is produced by faster transport of electroactive species, the increased

surface area for the electrochemical reaction to take place and possible activation of the strain-hardened zones.

2. The effect of dissolved oxygen in the slurry, which significantly increases the effective wear rate of steel, is produced mainly by generating corrosion of localized-type. Also, the formation of a work-hardened layer in the sub-surface is either suppressed or the layer is removed preferentially during the process. Finally, the mechanism of E-C wear in presence of oxygen is dominated by erosion-enhanced corrosion, in which plastic deformation induced by particles hitting onto the material favors the formation of anodic and cathodic sites on the surface larger than the area of the initial particle-target contact.

3. The mechanism by which temperature affects wear in this study is not clear. It is suggested that the contribution of corrosion and its cross-effects through synergy tends to dominate over the mechanical erosion. Further research is necessary to clarify this mechanism.

4. The interaction between slurry velocity and dissolved oxygen produces a positive synergism, i.e., the E−C rate of the material increases as both factors increase, where the effect of slurry velocity tends to dominate the interaction. The behavior of this interaction is explained by the mechanisms that dominate each factor. On the one hand, a higher slurry velocity increases the plastic deformation of the material, favoring the anodic dissolution in the plastically deformed areas, which in turn, intensifies the localized corrosion. On the other hand, both higher DO, and slurry velocity accelerate mass-transfer of oxygen and corrosion products, increasing the rate of corrosion and consequently the removal of mass from the target.

5. The individual effects of particle concentration and copper ions content in the slurry increase the E−C rate of the steel due to a greater frequency of impacts and the rise of corrosion kinetics by deposition of copper on the steel surface, respectively. However, their interaction results in an antagonistic behavior dominated by the effect of copper

ions. This behavior is determined by the effective amount of copper ions present in the liquid phase of the slurry rather than a significant change in the wear mechanism.

REFERENCES

Aguirre, J., & Walczak, M. (2017). Effect of dissolved copper ions on erosion-corrosion synergy of X65 steel in simulated copper tailing slurry. *Tribology International*, *114*(April), 329–336. http://doi.org/10.1016/j.triboint.2017.04.036

Ahmed, W. H. (2010). Annals of Nuclear Energy Evaluation of the proximity effect on flow-accelerated corrosion. *Annals of Nuclear Energy*, *37*(4), 598–605. http://doi.org/10.1016/j.anucene.2009.12.020

Akbarzadeh, E., Elsaadawy, E., Sherik, A. M., Spelt, J. K., & Papini, M. (2012). The solid particle erosion of 12 metals using magnetite erodent. *Wear*, *282–283*, 40–51. http://doi.org/10.1016/j.wear.2012.01.021

Al-Bukhaiti, M. A., Abouel-Kasem, A., Emara, K. M., & Ahmed, S. M. (2016). Particle Shape and Size Effects on Slurry Erosion of AISI 5117 Steels. *Journal of Tribology*, *138*(2), 024503 1-8. http://doi.org/10.1115/1.4031987

Alam, T., Aminul Islam, M., & Farhat, Z. N. (2015). Slurry Erosion of Pipeline Steel: Effect of Velocity and Microstructure. *Journal of Tribology*, *138*(2), 021604. http://doi.org/10.1115/1.4031599

Aminul Islam, M., & Farhat, Z. N. (2015). Mechanical and Electrochemical Synergism of API X42 Pipeline Steel During Erosion-corrosion. *Journal of Bio- and Tribo-Corrosion*, *1*(4), 1–18. http://doi.org/10.1007/s40735-015-0027-7

Aminul Islam, M., Farhat, Z. N., Ahmed, E. M., & Alfantazi, A. M. (2013). Erosion enhanced corrosion and corrosion enhanced erosion of API X-70 pipeline steel. *Wear*, *302*(1–2), 1592–1601. http://doi.org/10.1016/j.wear.2013.01.041

Andrews, N., Giourntas, L., Galloway, A. M., & Pearson, A. (2014). Effect of impact angle on the slurry erosion-corrosion of Stellite 6 and SS316. *Wear*, *320*(1), 143–151. http://doi.org/10.1016/j.wear.2014.08.006

Arabnejad, H., Shirazi, S. A., McLaury, B. S., Subramani, H. ., & Rhyne, L. D. (2015).

The effect of erodent particle hardness on the erosion of stainless steel. *Wear*, *332–333*, 1098–1103. http://doi.org/10.1016/0043-1648(91)90263-T

ASTM International. (1994). *ASTM G119-09 Standard guide for determining amount of synergism between wear and corrosion*. *Wear and Erosion, Metal Corrosion*. Retrieved from https://compass.astm.org/EDIT/html_annot.cgi?G119+09(2016)

ASTM International. (1999). Standard Practice for Preparing , Cleaning , and Evaluating Corrosion Test. *Significance*, *90* (Reapproved 2011), 1–9. http://doi.org/10.1520/G0001-03R11.2

Barik, R. C., Wharton, J. a., Wood, R. J. K., & Stokes, K. R. (2009). Electro-mechanical interactions during erosion-corrosion. *Wear*, *267*, 1900–1908. http://doi.org/10.1016/j.wear.2009.03.011

Ben-Ami, Y., Uzi, A., & Levy, A. (2016). Modelling the particles impingement angle to produce maximum erosion. *Powder Technology*, *301*, 1032–1043. http://doi.org/10.1016/j.powtec.2016.07.041

Benchaita, M. T., Griffith, P., & Rabinowicz, E. (1983). Erosion of Metallic Plate by Solid Particles Entrained in a Liquid Jet. *Journal of Engineering for Industry*, *105*(3), 215–222. http://doi.org/10.1049/iet-gtd.2009.0695

Bitter, J. G. A. (1963a). A study of erosion phenomena. Part I. *Wear*, *6*, 5–21. https://doi.org/10.1016/0043-1648(63)90003-6

Bitter, J. G. A. (1963b). A study of erosion phenomena. Part II. *Wear*, *6*(3), 169–190. http://doi.org/10.1016/0043-1648(63)90073-5

Burstein, G. T., & Sasaki, K. (2000). Effect of impact angle on the slurry erosion-corrosion of 304L stainless steel. *Wear*, *240*(1–2), 80–94. http://doi.org/10.1016/S0043-1648(00)00344-6

Chadwick, J. (2011). Hydrotransport. *International Mining*, (4), 57–65. Retrieved from http://www.infomine.com/library/publications/docs/internationalmining/chadwick2011k.pdf

Clark, H. M. (1991). On the impact rate and impact energy of particles in a slurry pot erosion tester. *Wear*, *147*(1), 165–183. http://doi.org/10.1016/0043-1648(91)90127-G

Clark, H. M. (2002). Particle velocity and size effects in laboratory slurry erosion measurements OR... do you know what your particles are doing? *Tribology International*, *35*(10), 617–624. http://doi.org/10.1016/S0301-679X(02)00052-X

Clark, H. M., & Burmeister, L. C. (1992). The influence of the squeeze film on particle impact velocities in erosion. *International Journal of Impact Engineering*, *12*(3), 415–426. http://doi.org/10.1016/0734-743X(92)90156-N

Clark, H. M., & Hartwich, R. B. (2001). A re-examination of the "particle size effect" in slurry erosion. *Wear*, *248*(1–2), 147–161. http://doi.org/10.1016/S0043-1648(00)00556-1

Clark, H. M. (1992). The influence of the flow field in slurry erosion. *Wear*, *152*(2), 223–240. http://doi.org/10.1016/0043-1648(92)90122-O

COCHILCO. (2015). *Identificar elementos de valor en residuos mineros (relaves) y su recuperación como productos comerciales*. Santiago. Retrieved from http://www.cochilco.cl/Archivos/destacados/20151021114631_Proyectorelaves.pdf

Dasgupta, R., Prasad, B., & Jha, A. (1998). Effect of sand concentration on slurry erosion of steels. *Materials Transactions*, *39*, 1185–1190.

Desale, G. R., Gandhi, B. K., & Jain, S. C. (2006). Effect of erodent properties on erosion wear of ductile type materials. *Wear*, *261*(7–8), 914–921. http://doi.org/10.1016/j.wear.2006.01.035

Desale, G. R., Gandhi, B. K., & Jain, S. C. (2008). Slurry erosion of ductile materials under normal impact condition. *Wear*, *264*(3–4), 322–330. http://doi.org/10.1016/j.wear.2007.03.022

Desale, G. R., Gandhi, B. K., & Jain, S. C. (2009). Particle size effects on the slurry erosion of aluminium alloy (AA 6063). *Wear*, *266*(11–12), 1066–1071. http://doi.org/10.1016/j.wear.2009.01.002

Desale, G. R., Gandhi, B. K., & Jain, S. C. (2011). Development of Correlations for Predicting the Slurry Erosion of Ductile Materials. *Journal of Tribology*, *133*(3), 031603. http://doi.org/10.1115/1.4004342

El-gammal, M., Mazhar, H., Cotton, J. S., Shefski, C., Pietralik, J., & Ching, C. Y. (2010). The hydrodynamic effects of single-phase flow on flow accelerated corrosion in a 90-degree elbow. *Nuclear Engineering and Design*, *240*(6), 1589–1598. http://doi.org/10.1016/j.nucengdes.2009.12.005

Finnie, I. (1960). Erosion of surfaces by solid particles. *Wear*, *3*(2), 87–103. http://doi.org/10.1016/0043-1648(60)90055-7

Finnie, I. (1995). Some reflections on the past and future of erosion. *Wear*, *186–187*, 1–10. http://doi.org/10.1016/0043-1648(95)07188-1

Frankel, G. S., & Rohwerder, M. (2007). Electrochemical Techniques for Corrosion. In A. Bard & M. Stratmann (Eds.), *Encyclopedia of Electrochemistry* (pp. 687–723). Wiley. http://doi.org/10.1002/9783527610426

Gandhi, B. K., Singh, S. N., & Seshadri, V. (1999). Study of the parametric dependence of erosion wear for the parallel flow of solid-liquid mixtures. *Tribology International*, *32*(5), 275–282. http://doi.org/10.1016/S0301-679X(99)00047-X

Giourntas, L., Hodgkiess, T., & Galloway, a. M. (2015). Comparative study of erosion-corrosion performance on a range of stainless steels. *Wear*, *332–333*, 1051–1058. http://doi.org/10.1016/j.wear.2014.12.052

Ghosh, S., Singh, A. K., Mula, S., Chanda, P., Mahashabde, V. V., & Roy, T. K. (2017) Mechanical properties, formability and corrosion resistance of thermomechanically controlled processed Ti-Nb stabilized IF steel. Materials Science and Engineering A, 684(December 2016), 22–36. https://doi.org/10.1016/j.msea.2016.12.034

Guo, H. X., Lu, B. T., & Luo, J. L. (2005). Interaction of mechanical and electrochemical factors in erosion-corrosion of carbon steel. *Electrochimica Acta*, *51*(2), 315–323. http://doi.org/10.1016/j.electacta.2005.04.032

Guo, H. X., Lu, B. T., & Luo, J. L. (2006). Response of surface mechanical properties to electrochemical dissolution determined by in situ nanoindentation technique. *Electrochemistry Communications*, *8*(7), 1092–1098. http://doi.org/10.1016/j.elecom.2006.04.020

Gupta, R., Singh, S. N., & Seshadri, V. (1995). Study on the uneven wear rate in a slurry pipeline. *Bulk Solids Handling*, *15*(4), 603–607. http://doi.org/10.1016/0043-1648(94)06566-7

Gutman, E. M. (2002). Chemomechanical Effects Accompanying Mechanochemical Reactions and Creep. *Materials Science Forum*, *386–388*, 235–244. http://doi.org/10.4028/www.scientific.net/MSF.386-388.235

Hadavi, V., Arani, N. H., & Papini, M. (2019). Numerical and experimental investigations of particle embedment during the incubation period in the solid particle erosion of ductile materials. *Tribology International*, *129*(April 2018), 38–45. http://doi.org/10.1016/j.triboint.2018.08.013

Heitz, E. (1990). Chemo-Mechanical Effects of Flow on Corrosion, *CORROSION*. 1991;47(2):135-145. https://doi.org/10.5006/1.3585229

Heitz, E. (1996). Mechanistically based prevention strategies of flow-induced corrosion. *Electrochimica Acta*, *41*(4), 503–509. http://doi.org/10.1016/0013-4686(95)00336-3

Heusler, K. E., Landolt, D., & Trasatti, S. (1989). Electrochemical corrosion nomenclature. *Pure and Applied Chemistry*, *61*(1), 19–22.

Hu, X., & Neville, a. (2005). The electrochemical response of stainless steels in liquid-solid impingement. *Wear*, *258*(1–4), 641–648. http://doi.org/10.1016/j.wear.2004.09.043

Hua, Y., Barker, R., & Neville, A. (2015). The effect of O2 content on the corrosion behaviour of X65 and 5Cr in water-containing supercritical CO2 environments. *Applied Surface Science*, *356*, 499–511. http://doi.org/10.1016/j.apsusc.2015.08.116

Hutchings, I. M. (1992). *Tribology: Friction and Wear of Engineering Materials*. Oxford,UK: Butterworth-Heinemann.

Hutchings, I. M. (1981). A model for the erosion of metals by sperical particles at normal incidence. *Wear*, *70*, 269–281.

Huth, S. (2011). Tribocorrosion of Passive Metals and Coatings. In Landolt D. & M. S. (Eds.), *Tribocorrosion of Passive Metals and Coatings* (pp. 265–295). http://doi.org/10.1533/9780857093738.2.265

Islam, M. A., & Farhat, Z. (2017). Erosion-corrosion mechanism and comparison of erosion-corrosion performance of API steels. *Wear*, *376–377*, 533–541. http://doi.org/10.1016/j.wear.2016.12.058

Islam, M. A., & Farhat, Z. N. (2013). The synergistic effect between erosion and corrosion of API pipeline in CO_2 and saline medium. *Tribology International*, *68*, 26–34. http://doi.org/10.1016/j.triboint.2012.10.026

Islam, M. A., & Farhat, Z. N. (2014). Effect of impact angle and velocity on erosion of API X42 pipeline steel under high abrasive feed rate. *Wear*, *311*(1–2), 180–190. http://doi.org/10.1016/j.wear.2014.01.005

Iwai, Y., & Nambu, K. (1997). Slurry wear properties of pump lining materials. *Wear*, *210*(1–2), 211–219. http://doi.org/10.1016/S0043-1648(97)00055-0

Jana, B. D., & Stack, M. M. (2005). Modelling impact angle effects on erosion-corrosion of pure metals: Construction of materials performance maps. *Wear*, *259*, 243–255. http://doi.org/10.1016/j.wear.2005.02.012

Javaheri, V., Porter, D., & Kuokkala, V. T. (2018). Slurry erosion of steel – Review of tests, mechanisms and materials. *Wear*, *408–409*(July 2017), 248–273. http://doi.org/10.1016/j.wear.2018.05.010

Jiang, S., Chai, F., Su, H., & Yang, C. (2017). Influence of chromium on the flow-accelerated corrosion behavior of low alloy steels in 3.5 % NaCl solution, *123*(May), 217–227. http://doi.org/10.1016/j.corsci.2017.04.024

JRI, & INNOVA CORFO. (2010). *Aplicación Industrial de la Tecnología de Espesamiento Extremo En Proyectos Mineros*.

Juan Rayo Capacitación. (2013). *Fuidodinámica aplicada a la minería*. (Juan Rayo Capacitación S.A., Ed.). Santiago: JRI.

Kain, V., Roychowdhury, S., Ahmedabadi, P., & Barua, D. K. (2011). Flow accelerated corrosion : Experience from examination of components from nuclear power plants. *Engineering Failure Analysis*, *18*(8), 2028–2041. http://doi.org/10.1016/j.engfailanal.2011.06.007

Kingkam, W., Zhao, C.-Z., Li, H., Zhang, H.-X., & Li, Z.-M. (2018). Hot Deformation and Corrosion Resistance of High-Strength Low-Alloy Steel. Acta Metallurgica Sinica (English Letters), 32(4), 495–505. https://doi.org/10.1007/s40195-018-0797-2

Kleis, I., & Kulu, P. (2008). *Solid particle erosion* (First). Springer London.

Kosa, E., & Göksenli, A. (2015). Effect of Impact Angle on Erosive Abrasive Wear of Ductile and Brittle Materials. *International Journal of Mechanical, Aerospace, Industrial, Mechatronic and Manufacturing Engineering*, *9*(9), 1582–1586.

Kosel, T. H. (1992). Solid Particle Erosion. In *ASM Handbook Vol. 18*. ASM International, Materials Park, OH.

Landolt, D. (2007). *Corrosion and Surface Chemistry of Metals*. (EPFL Press, Ed.) (First) Florida, US: CRC Press.

Levy, A. V., & Chik, P. (1983). The effects of erodent composition and shape on the erosion of steel. *Wear*, *89*(2), 151–162. http://doi.org/10.1016/0043-1648(83)90240-5

Levy, A. V, & Hickey, G. (1987). Liquid-solid particle slurry erosion of steels. *Wear*, *117*, 129–146. https://doi.org/10.1016/0043-1648(87)90251-1

Li, W., Pots, B. F. M., Brown, B., Kee, K. E., & Nesic, S. (2016). A direct measurement of wall shear stress in multiphase flow — Is it an important parameter in CO_2 corrosion of carbon steel pipelines ? *Corrosion Science*, *110*, 35–45. http://doi.org/10.1016/j.corsci.2016.04.008

Li, Y., Burstein, G. T., & Hutchings, I. M. (1995). The influence of corrosion on the

erosion of aluminium by aqueous silica slurries, *187*, 515–522.

Lindgren, M., & Perolainen, J. (2014). Slurry pot investigation of the influence of erodent characteristics on the erosion resistance of austenitic and duplex stainless steel grades. *Wear*, *319*(1–2), 38–48. http://doi.org/10.1016/j.wear.2014.07.006

Lu, B. T., Lu, J. F., & Luo, J. L. (2011). Erosion-corrosion of carbon steel in simulated tailing slurries. *Corrosion Science*, *53*(3), 1000–1008. http://doi.org/10.1016/j.corsci.2010.11.034

Lu, B. T., & Luo, J. L. (2006). Synergism of electrochemical and mechanical factors in erosion - Corrosion. *Journal of Physical Chemistry B*, *110*(9), 4217–4231. http://doi.org/10.1021/jp051985f

Lu, B. T., & Luo, J. L. (2015). Correlation between surface-hardness degradation and erosion resistance of carbon steel—Effects of slurry chemistry. *Tribology International*, *83*, 146–155. http://doi.org/10.1016/j.triboint.2014.11.008

Lynn, R. S., Wong, K. K., & Clark, H. M. (1991). On the particle size effect in slurry erosion. *Wear*, *149*(1–2), 55–71. http://doi.org/10.1016/0043-1648(91)90364-Z

Madasamy, P., Mohan, T. V. K., Sylvanus, A., Natarajan, E., & Rani, H. P. (2018). Hydrodynamic e ff ects on fl ow accelerated corrosion at 120 ° C and neutral pH conditions, *94*(May), 458–468. http://doi.org/10.1016/j.engfailanal.2018.08.021

Malka, R., Ne, S., & Gulino, D. A. (2007). Erosion – corrosion and synergistic effects in disturbed liquid-particle flow, *262*, 791–799. http://doi.org/10.1016/j.wear.2006.08.029

Marcus, P. (2017). *Corrosion Mechanisms in Theory and Practice*. (P. Marcus, Ed.) (Third Edit). Florida,USA:CRC Press.

Matsumura, M. (1994). Erosion-Corrosion of Metallic Materials in Slurries. *Corrosion Reviews*, *12*(3–4), 321–340. http://doi.org/10.1515/CORRREV.1994.12.3-4.321

Mbabazi, J. G., Sheer, T. J., & Shandu, R. (2004). A model to predict erosion on mild steel surfaces impacted by boiler fly ash particles. *Wear*, *257*(5–6), 612–624.

http://doi.org/10.1016/j.wear.2004.03.007

Mccafferty, E. (2010). *Introduction to Corrosion Science*. http://doi.org/10.1007/978-1-4419-04553

Mcgrady, J., Scenini, F., Duff, J., Stevens, N., Cassineri, S., Curioni, M., & Banks, A. (2017). Investigation into the effect of water chemistry on corrosion product formation in areas of accelerated fl ow, *493*. http://doi.org/10.1016/j.jnucmat.2017.06.030

Meng, H. C., & Ludema, K. C. (1995). Wear models and predictive equations: their form and content. *Wear*, *181–183*(PART 2), 443–457. http://doi.org/10.1016/0043-1648(95)90158-2

Meng, H., Hu, X., & Neville, a. (2007). A systematic erosion-corrosion study of two stainless steels in marine conditions via experimental design. *Wear*, *263*, 355–362. http://doi.org/10.1016/j.wear.2006.12.007

Minería Chilena. (2014). Transporte de fluidos: La confiabilidad es clave.. Retrieved from http://www.mch.cl/informes-tecnicos/transporte-de-fluidos-la-confiabilidad-es-clave/#

Misra, A., & Finnie, I. (1981). On the size effect in abrasive and erosive wear. *Wear*, *65*(3), 359–373. http://doi.org/10.1016/0043-1648(81)90062-4

Molina, N., Aguirre, J., & Walczak, M. (2019). Application of FFT analysis for the study of directionality of wear scars in exposure to slurry flow of varying velocity. Wear, 426–427(November 2018), 589–595. https://doi.org/10.1016/j.wear.2019.01.013

Molinari, J. F., & Ortiz, M. (2002). A study of solid-particle erosion of metallic targets. *International Journal of Impact Engineering*, *27*(4), 347–358. http://doi.org/10.1016/S0734-743X(01)00055-0

Montgomery, D. C. (2017). *Design and Analysis of Experiments* (9th ed.). Wiley.

Motte, R. A. De, Barker, R., Burkle, D., Vargas, S. M., & Neville, A. (2018). The early stages of FeCO 3 scale formation kinetics in CO 2 corrosion. *Materials Chemistry and Physics*, *216*, 102–111. http://doi.org/10.1016/j.matchemphys.2018.04.077

Nandre, B. D., & Desale, G. R. (2018). Study the Effect of Impact Angle on Slurry Erosion Wear of Four Different Ductile Materials. *Materials Today: Proceedings*, *5*(2), 7561–7570. http://doi.org/10.1016/j.matpr.2017.11.428

National Institutes of Health. (n.d.). ImageJ. Retrieved from https://imagej.nih.gov/ij/

Neville, a., Reyes, M., & Xu, H. (2002). Examining corrosion effects and corrosion/erosion interactions on metallic materials in aqueous slurries. *Tribology International*, *35*(10), 643–650. http://doi.org/10.1016/S0301-679X(02)00055-5

Neville, A., Hodgkiess, T., & Xu, H. (1999). An electrochemical and microstructural assessment of erosion-corrosion of cast iron. *Wear*, *233–235*, 523–534. http://doi.org/10.1002/1521-4176(200201)53:1<5::AID-MACO5>3.0.CO;2-R

Nguyen, Q. B., Nguyen, V. B., Lim, C. Y. H., Trinh, Q. T., Sankaranarayanan, S., Zhang, Y. W., & Gupta, M. (2014). Effect of impact angle and testing time on erosion of stainless steel at higher velocities. *Wear*, *321*, 87–93. http://doi.org/10.1016/j.wear.2014.10.010

Nguyen, V. B., Nguyen, Q. B., Zhang, Y. W., Lim, C. Y. H., & Khoo, B. C. (2016). Effect of particle size on erosion characteristics. *Wear*, *348–349*, 126–137. http://doi.org/10.1016/j.wear.2015.12.003

Postlethwaite, J. (1981). Effect of Chromate Inhibitor on the Mechanical and Electrochemical Components of Erosion-Corrosion in Aqueous Slurries of Sand. *Corrosion*, *37*(1), 1–5. http://doi.org/10.5006/1.3593833

Pourbaix, M. (1974). *Atlas of electrochemical equilibria in aqueous solutions* (Second). Houston Texas;USA: NACE.

Prasad, M., Gopika, V., Sridharan, A., Parida, S., & Gaikwad, A. J. (2018). Annals of Nuclear Energy Hougaard process stochastic model to predict wall thickness in Flow Accelerated Corrosion. *Annals of Nuclear Energy*, *117*, 247–258. http://doi.org/10.1016/j.anucene.2018.03.035

Rajahram, S. S., Harvey, T. J., Walker, J. C., Wang, S. C., & Wood, R. J. K. (2012). Investigation of erosion-corrosion mechanisms of UNS S31603 using FIB and TEM.

Tribology International, *46*(1), 161–173. http://doi.org/10.1016/j.triboint.2011.05.012

Rajahram, S. S., Harvey, T. J., & Wood, R. J. K. (2009). Erosion-corrosion resistance of engineering materials in various test conditions. *Wear*, *267*(1–4), 244–254. http://doi.org/10.1016/j.wear.2009.01.052

Rajahram, S. S., Harvey, T. J., & Wood, R. J. K. (2010). Full factorial investigation on the erosion-corrosion resistance of UNS S31603. *Tribology International*, *43*(11), 2072–2083. http://doi.org/10.1016/j.triboint.2010.05.012

Sherif, E. M., Almajid, A. A., Khalil, K. A., Junaedi, H., & Latief, F. H. (2013). Electrochemical Studies on the Corrosion Behavior of API X65 Pipeline Steel in Chloride Solutions. *International Journal of Electrochemical Science*, *8*, 9360–9370.

Shipway, P. H., & Hutchings, I. M. (1996). The rôle of particle properties in the erosion of brittle materials. *Wear*, *193*, 105–113.

Silverman, D. C. (1999). Technical Note: On Estimating Conditions for Simulating Velocity-Sensitive Corrosion in the Rotating Cylinder Electrode. *Corrosion*, *55*(12), 1115–1118. http://doi.org/10.5006/1.3283948

Silverman, D. C. (2004). The Rotating Cylinder Electrode for Examining Velocity-Sensitive Corrosion—A Review. *Corrosion*, *60*(11), 1003–1023. http://doi.org/10.5006/1.3299215

Silverman, D. C. (2005). Technical Note: Conditions for Similarity of Mass-Transfer Coefficients and Fluid Shear Stresses Between the Rotating Cylinder Electrode and Pipe. *Corrosion*, *61*(6), 515–518. http://doi.org/10.5006/1.3278187

Sinha, S. L., Dewangan, S. K., & Sharma, A. (2017). A review on particulate slurry erosive wear of industrial materials: In context with pipeline transportation of mineral−slurry. *Particulate Science and Technology*, *35*(1), 103–118. http://doi.org/10.1080/02726351.2015.1131792

Söderberg, S., Hogmark, S., Engman, U., & Swahn, H. (1981). Erosion classification of materials using a centrifugal erosion tester. *Tribology International*, *14*(6), 333–343.

http://doi.org/10.1016/0301-679X(81)90101-8

Söderberg, S., Hogmark, S., & Swahn, H. (1983). Mechanisms of Material Removal During Erosion of a Stainless Steel. *A S L E Transactions*, *26*(2), 161–172. http://doi.org/10.1080/05698198308981490

Stachowiak, G. B., Salasi, M., Rickard, W. D. A., & Stachowiak, G. W. (2016). The effects of particle angularity on low-stress three-body abrasion-corrosion of 316L stainless steel. *Corrosion Science*, *111*, 690–702. http://doi.org/10.1016/j.corsci.2016.06.008

Stack, M. M., Corlett, N., & Turgoose, S. (2003). Some thoughts on modelling the effects of oxygen and particle concentration on the erosion-corrosion of steels in aqueous slurries. *Wear*, *255*(1–6), 225–236. http://doi.org/10.1016/S0043-1648(03)00205-9

Stack, M. M., & Abdulrahman, G. H. (2010). Tribology International Mapping erosion-corrosion of carbon steel in oil exploration conditions : Some new approaches to characterizing mechanisms and synergies. *Tribiology International*, *43*(7), 1268–1277. http://doi.org/10.1016/j.triboint.2010.01.005

Stack, M. M., Abdelrahman, S. M., & Jana, B. D. (2010). Some perspectives on modelling the effect of temperature on the erosioncorrosion of Fe in aqueous conditions. *Tribology International*, *43*(12), 2279–2297. http://doi.org/10.1016/j.triboint.2010.07.015

Stack, M. M., & Abdulrahman, G. H. (2012). Mapping erosion-corrosion of carbon steel in oil–water solutions: Effects of velocity and applied potential. *Wear*, *274–275*, 401–413. http://doi.org/10.1016/j.wear.2011.10.008

Stack, M. M., & Pungwiwat, N. (1999). Slurry erosion of metallics, polymers, and ceramics: particle size effects. *Materials Science and Technology*, *15*(3), 337–344. http://doi.org/10.1179/026708399101505770

Stack, M. M., Zhou, S., & Newman, R. C. (1996). Effects of particle velocity and applied potential on erosion of mild steel in carbonate/bicarbonate slurry. *Materials Science and Technology*, *12*(3), 261–268. http://doi.org/10.1179/mst.1996.12.3.261

Stevenson, A. N. J., & Hutchings, I. M. (1995). Scaling laws for particle velocity in the

gas-blast erosion test. *Wear*, *181–183*(PART 1), 56–62. http://doi.org/10.1016/0043-1648(95)90008-X

Telfer, C. G., Stack, M. M., & Jana, B. D. (2012). Particle concentration and size effects on the erosion-corrosion of pure metals in aqueous slurries. *Tribology International*, *53*, 35–44. http://doi.org/10.1016/j.triboint.2012.04.010

Tian, B. R., & Cheng, Y. F. (2008). Electrochemical corrosion behavior of X-65 steel in the simulated oil sand slurry. I: Effects of hydrodynamic condition. *Corrosion Science*, *50*(3), 773–779. http://doi.org/10.1016/j.corsci.2007.11.008

Turenne, S., Fiset, M., & Masounave, J. (1989). The effect of sand concentration on the erosion of materials by a slurry jet. *Wear*, *133*(1), 95–106. http://doi.org/10.1016/0043-1648(89)90116-6

Umemoto, M. (2003). Nanocrystallization of Steels by Severe Plastic Deformation. *Materials Transactions*, *44*(10), 1900–1911. http://doi.org/10.2320/matertrans.44.1900

Vera, R., Vinciguerra, F., & Bagnara, M. (2015). Comparative Study of the Behavior of API 5L-X65 Grade Steel and ASTM A53-B Grade Steel against Corrosion in Seawater. *International Journal of Electrochemical Sciences*. 10, 6187–6198.

Walsh, F. C., Kear, G., Nahlé, A. H., Wharton, J. A., & Arenas, L. F. (2017). The rotating cylinder electrode for studies of corrosion engineering and protection of metals—An illustrated review. *Corrosion Science*, *123*, 1–20. http://doi.org/10.1016/j.corsci.2017.03.024

Wang, Y. F., & Yang, Z. G. (2008). Finite element model of erosive wear on ductile and brittle materials. *Wear*, *265*(5–6), 871–878. http://doi.org/10.1016/j.wear.2008.01.014

Winter, R. E., & Hutchings, I. M. (1974). Solid particle erosion studies using single angular particles. *Wear*, *29*, 181–194.

Wood, R. J. K. (2006). Erosion-corrosion interactions and their effect on marine and offshore materials. *Wear*, *261*(9), 1012–1023. http://doi.org/10.1016/j.wear.2006.03.033

Wood, R. J. K. (2010). Tribocorrosion. In T. Richardson (Ed.), *Shreir's Corrosion* (pp. 1005–1050). Elsevier Sc. http://doi.org/https://doi.org/10.1016/B978-044452787-5.00041-X

Wood, R. J. K., & Hutton, S. P. (1990). The synergistic effect of erosion and corrosion: trends in published results. *Wear*, *140*(2), 387–394. http://doi.org/10.1016/0043-1648(90)90098-U

Wood, R. J. K., Walker, J. C., Harvey, T. J., Wang, S., & Rajahram, S. S. (2013). Influence of microstructure on the erosion and erosion-corrosion characteristics of 316 stainless steel. *Wear*, *306*(1–2), 254–262. http://doi.org/10.1016/j.wear.2013.08.007

Xie, J., Alpas, a. T., & Northwood, D. O. (2003a). Mechano-electrochemical effect between erosion and corrosion. *Journal of Materials Science*, *38*(24), 4849–4856. http://doi.org/10.1023/B:JMSC.0000004404.53054.b4

Xie, J., Alpas, A. T., & Northwood, D. O. (2003b). The Effect of Erosion on the Electrochemical Properties of AISI 1020 Steel. *Journal of Materials Engineering and Performance*, *12*(1), 77–86. http://doi.org/10.1361/105994903770343510

Yang, Y., & Cheng, Y. F. (2012). Parametric effects on the erosion-corrosion rate and mechanism of carbon steel pipes in oil sands slurry. *Wear*, *276–277*, 141–148. http://doi.org/10.1016/j.wear.2011.12.010

Yin, S., & Li, D. Y. (2008). A New Phenomenon Observed in Determining the Wear-Corrosion Synergy during a Corrosive Sliding Wear Test. *Tribology Letters*, *29*(1), 45–52. http://doi.org/10.1007/s11249-007-9280-3

Young, J. P., & Ruff, A. W. (1977). Particle Erosion Measurements on Metals. *Journal of Engineering Materials and Technology*, *99*(2), 121–125.

Zhang, G. a., & Cheng, Y. F. (2009). Electrochemical corrosion of X65 pipe steel in oil/water emulsion. *Corrosion Science*, *51*(4), 901–907. http://doi.org/10.1016/j.corsci.2009.01.020

Zhou, S., Stack, M. M., & Newman, R. C. (1996). Characterization of Synergistic Effects

Between Erosion and Corrosion in an Aqueous Environment Using Electrochemical Techniques. *Corrosion, 52*(12), 934–946.

APPENDIX A: Results of erosion-corrosion rate used for factorial analysis.

Table A 1. Results of weight loss and E-C rate for each experimental run performed.

Order of run	V ($m \cdot s^{-1}$)	P (wt.%)	T (°C)	pH	DO (ppm)	Cu^{2+} (ppm)	Weight loss (mg)	E-C rate ($mg \cdot cm^{-2} \cdot h^{-1}$)
1	5	55	35	8	5	250	18.2	3.1
2	7	65	25	11	0	500	11.7	2.0
3	3	45	25	5	10	500	8.0	1.4
4	7	45	45	11	10	0	27.7	4.7
5	3	45	45	11	10	500	16.5	2.8
6	3	65	25	11	0	0	1.7	0.3
7	7	45	25	11	0	0	8.8	1.5
8	5	55	35	8	5	250	18.2	3.1
9	3	65	45	5	0	0	8.3	1.4
10	7	45	45	11	0	500	35.7	6.1
11	3	45	45	11	0	0	2.9	0.5
12	7	65	25	5	0	0	26.8	4.6
13	7	45	25	11	10	500	39.9	6.8
14	7	65	45	11	10	500	29.0	4.9
15	7	45	45	5	0	0	19.7	3.3
16	7	65	45	5	10	0	50.9	8.6
17	5	55	35	8	5	250	18.2	3.1
18	7	65	25	11	10	0	39.2	6.7
19	3	65	45	5	10	500	15.0	2.5
20	3	45	25	11	0	500	0.9	0.2
21	3	45	25	11	10	0	8.5	1.4
22	3	65	45	11	0	500	1.0	0.2
23	7	65	45	5	0	500	25.6	4.3
24	3	45	25	5	0	0	1.3	0.2
25	7	65	25	5	10	500	39.4	6.7
26	7	45	45	5	10	500	55.5	9.4
27	3	45	45	5	0	500	1.9	0.3
28	3	65	25	5	10	0	8.7	1.5
29	7	45	25	5	0	500	12.6	2.1

Order of run	V ($m \cdot s^{-1}$)	P (wt.%)	T (°C)	pH	DO (ppm)	Cu^{2+} (ppm)	Weight loss (mg)	E-C rate ($mg \cdot cm^{-2} \cdot h^{-1}$)
30	3	65	25	11	10	500	6.7	1.1
31	7	45	25	5	10	0	28.6	4.9
32	3	45	45	5	10	0	13.5	2.3
33	7	65	45	11	0	0	32.3	5.5
34	3	65	45	11	10	0	10.7	1.8
35	3	65	25	5	0	500	2.1	0.4

Document revision: 2019/05/06